GL-TR-90-0038

# PHYSICS STUDIES IN
# ARTIFICIAL IONOSPHERIC MIRROR (AIM)
# RELATED PHENOMENA

| | | |
|---|---|---|
| R. Short | A. Ali | A. Drobot |
| P. Lallement | P. Koert | K. Tsang |
| D. Papadopoulos | R. Shanny | P. Vitello |
| T. Wallace | C. Stewart | |

ARCO Power Technologies, Inc.
1250 24th Street, NW
Suite 850
Washington, DC 20037

23 February 1990

Final Report
(26 August 87 - 31 August 89)

**Approved for Public Release, Distribution Unlimited**

Geophysics Laboratory
Air Force Systems Command
United States Air Force
Hanscom Air Force Base, MA 01731-5000

AD-A227 112

91 1 10 020

"This technical report has been reviewed and is approved for publication"

JOHN L. HECKSCHER
Contract Manager

JOHN E. RASMUSSEN
Branch Chief

FOR THE COMMANDER

ROBERT A. SKRIVANEK
Division Director

| REPORT DOCUMENTATION PAGE | | Form Approved OMB No. 0704-0188 |
|---|---|---|

| 1a. REPORT SECURITY CLASSIFICATION Unclassified | | 1b. RESTRICTIVE MARKINGS N/A | | |
|---|---|---|---|---|
| 2a. SECURITY CLASSIFICATION AUTHORITY | | 3. DISTRIBUTION/AVAILABILITY OF REPORT Approved for public release, distribution is unlimited. | | |
| 2b. DECLASSIFICATION/DOWNGRADING SCHEDULE | | | | |
| 4. PERFORMING ORGANIZATION REPORT NUMBER(S) APTI - 5004 | | 5 MONITORING ORGANIZATION REPORT NUMBER(S) GL-TR-90-0038 ADA-227112 | | |
| 6a. NAME OF PERFORMING ORGANIZATION ARCO Power Technologies, Inc. | 6b. OFFICE SYMBOL (If applicable) | 7a. NAME OF MONITORING ORGANIZATION Geophysics Laboratory | | |
| 6c. ADDRESS (City, State, and ZIP Code) 1250 24th Street, NW Suite 850 Washington, DC 20037 | | 7b. ADDRESS (City, State, and ZIP Code) Hanscom AFB, MA 01731-5000 | | |
| 8a. NAME OF FUNDING/SPONSORING ORGANIZATION ESD | 8b. OFFICE SYMBOL (If applicable) TCO | 9 PROCUREMENT INSTRUMENT IDENTIFICATION NUMBER F19628-87-C-0127 | | |
| 8c. ADDRESS (City, State, and ZIP Code) Hanscom AFB, MA 01731-5000 | | 10. SOURCE OF FUNDING NUMBERS | | |

| | | PROGRAM ELEMENT NO. 62101F | PROJECT NO. 4140 | TASK NO ES | WORK UNIT ACCESSION NO. AA |
|---|---|---|---|---|---|

11. TITLE (Include Security Classification)
Physics Studies in Artificial Ionospheric Mirror (AIM) Related Phenomena

12. PERSONAL AUTHOR(S) R. Short, P. Lallement, D. Papadopoulos, T. Wallace, A. Ali, P. Koert, R. Shanny, C. Stewart, A. Drobot,* K. Tsang,* P. Vitello*

| 13a. TYPE OF REPORT Final Report | 13b. TIME COVERED FROM 87/8/26 TO 89/8/31 | 14. DATE OF REPORT (Year, Month, Day) 90/2/23 | 15. PAGE COUNT 148 |
|---|---|---|---|

16 SUPPLEMENTARY NOTATION        * Science Applications International, Corp.
1710 Goodridge Dr., McLean, VA 22102

| 17. COSATI CODES | | | 18. SUBJECT TERMS (Continue on reverse if necessary and identify by block number) |
|---|---|---|---|
| FIELD | GROUP | SUB-GROUP | |
| 0401 | | | Artificial Ionospheric Mirror |
| 1702 | | | Wave-Plasma Interactions |

19. ABSTRACT (Continue on reverse if necessary and identify by block number)
This document reports on the progress made and final results of a Geophysics Laboratory sponsored study into the fundamental physics of electromagnetic induced ionization in the lower ionosphere (60 - 80 km), using a ground based radiation source. The technique of remotely controlled ionization can be used to create a layered region of ionization and to then use the Artificial Ionospheric Mirror (AIM) to reflect HF/VHF signals for over-the-horizon communication and radar applications. The objective of the study was to identify the basic physics issues controlling RF breakdown phenomena and to develop an understanding of those issues sufficient for performing quantitative prediction of AIM characteristics and the impact of those characteristics on the reflecting wave. Results of the study indicate that AIM is a viable concept and has the potential of providing important benefits over more traditional communication/radar technology.

| 20 DISTRIBUTION/AVAILABILITY OF ABSTRACT ☒ UNCLASSIFIED/UNLIMITED ☐ SAME AS RPT ☐ DTIC USERS | 21. ABSTRACT SECURITY CLASSIFICATION Unclassified | |
|---|---|---|
| 22a NAME OF RESPONSIBLE INDIVIDUAL John L. Heckscher | 22b. TELEPHONE (Include Area Code) (617) 377-4052 | 22c OFFICE SYMBOL GL/LID |

DD Form 1473, JUN 86        Previous editions are obsolete         SECURITY CLASSIFICATION OF THIS PAGE

# TABLE OF CONTENTS

## 1.0 INTRODUCTION

The concept of using artificial ionospheric plasmas for over-the-horizon (OTH) transmission of electromagnetic waves was presented by ARCO Power Technologies, Inc. (APTI) to the Air Force during the Project Forecast II technology review and subsequently funded by the Geophysics Laboratory (GL) in its lead role for the S&T initiative PT-47 Plasma Defense Technology. The concept relies on a ground-based radio frequency (RF) heater to create an artificial region of enhanced plasma density and to use this region as a reflector of electromagnetic waves. The objective of the research described in this technical report is to achieve a high confidence level in the physics and scaling related to Artificial Ionospheric Mirror (AIM) applications.

Since the formulation of the initial concept by APTI, the work performed under the current GL contract has led to a refinement of the idea, innovative approaches to the creation and control of the ionized region, and identification of the key parameters required for a highly effective and practical operational AIM system using current technologies. The research effort is founded on an examination of physics issues, on the development of a conceptual RF heater model, and on simulation of candidate systems. The physics reported here is based on zero- and one-dimensional models validated by previous experimental results extrapolated to the relevant parameter range. The matching of the phenomenological requirements, the RF-heater technology and the desired system performance characteristics have produced a very promising outlook for the application. Furthermore, the performance requirements of potential system components have been narrowed on the basis of our increased understanding of the underlying physical processes. Rigorous computer simulations have been developed of many aspects of the system and the physical processes. A modular heater antenna concept based on conventional, solid-state sources has been developed; however, a parallel effort has been underway to consider the realization of the heater using tubes and dishes.

### 1.1   Physics Issues

The critical physics issues associated with the AIM concept have been identified and investigated

- atmospheric breakdown physics and related scaling laws;
- AIM useful lifetime;
- AIM altitude, profile, and attitude control; and

1

- AIM reflection, refraction and absorption characteristics for 20-100 MHz frequencies.

The present analysis and the conclusions presented in this report are based on zero- and one-dimensional modeling as well as the experimental data (i.e. power and energy considerations with time dependence and at most one spatial dimension). The status of experimental verification of key uncertainties related to the above issues can be seen in Figure 1.1. These are listed in order of critical importance in reducing current uncertainties in the physical phenomenology as they relate to the performance of an AIM system. The issues have been listed in descending order of importance (i.e. Plasma Control is the most important). The issues listed have also been graded with respect to the amenability (cost, complexity, etc.) of their resolution to laboratory experimentation, with "A" representing very, "B" moderately, and "F" not amenable.

| Experimental Questions | Status of Lab Exps | Physics Issues | Amenable to Lab Exp. |
|---|---|---|---|
| Plasma Control | Little besides one USSR crossed beam experiment | Level of control in chirping and focusing; Mapping of field structure to density structure ℓ underdense; Smoothness in painting of layer | B |
| Plasma Cooling And Decay | Some Experimental basis | Conditions for plasma decay time longer than 3-body attachments; Role of wind transport | B |
| Propagation | No labs exps in proper range; Some field experiments in ionosphere | Spatial and temporal inhomogeneities | F |
| Physics of Breakdown | Numerous Experiments; Large Data Base | Inelastic cross-sections; Threshold for runaway ionization; Role of atmospheric irregularity structure | A |

Figure 1.1. Currently Identified Critical Physics Issues

## 1.1.1 Accomplishments to Date

Efforts to date on the AIM phenomenology investigations and system trade-off studies have resulted in a first-order understanding of the ionization process and how this process can be used to create a controlled plasma mirror. Specifically, results to date include:

2

1) A preliminary AIM system concept, incorporating

   - a zero-dimensional analytic ionization model and a one-dimensional numeric simulation,

   - a "painting" strategy for creating an inclined mirror,

   - a RF heater design,

   - a baseline system concept, and

   - a system operational timeline.

2) A set of zero-order system performance trade studies, including

   - a range of achievable mirror characteristics,

   - RF heater design parameters,

   - system design parameters,

   - quantitative impact of AIM on RF transmission waveform, and

   - prediction of AIM system performance.

3) Identification of the remaining technical uncertainties and an approach for addressing them, including

   - impact of RF self absorption considerations on ionization,

   - exact scaling of physics to AIM regime,

   - control of breakdown and subsequent AIM behavior in open atmosphere, and

   - demonstration of AIM orientation, uniformity, and smoothness.

## 1.1.2 Remaining Uncertainties

Although a large body of RF breakdown data is available, and theoretical models exist for all aspects of the ionization process, validation of the the AIM concept will require experimental confirmation of theory in several areas, which are outlined in Figure 1.2 below. Virtually all chamber data on low-pressure RF breakdown have been taken in chambers of small dimensions. The main loss mechanism in a chamber is diffusion to the sides of the chamber, as opposed to attachment and recombination. This leads to higher requirements for breakdown power in a chamber than in open air. Because patch decay

3

times are expected to be of the order of .1 - 1 second, a very large chamber would be required to provide accurate predictions of patch decay rates.

| Phenomenon | Relevant Physical Parameters | | Implication on Validity of Past Experiments |
|---|---|---|---|
| | Previous Experiments | AIM Scenario | |
| Breakdown | $l_f \ll l_a$<br>Spot size $\ll l_d$<br>$w_p = w_{rf}$ | $l_f \gg l_a$<br>Spot size $\gg l_d$<br>$w_p \ll w_{rf}$ | Does not properly account for self absorption<br>Diffusion effects dominate<br>Does not measure evolution of breakdown |
| Lifetime | Spot size $< l_d$<br>Molecular time $\sim t_d$<br>$w_p = w_{rf}$ | Patch Size $\gg l_d$<br>Molecular time $\ll t_d$<br>$w_p \ll w_{rf}$ | Diffusion effects bias chamber data<br>Chamber wall affects lifetime<br>High energy absorption per molecule alters atomic/molecular energy states |
| Peak Density | $l_f \ll l_a$<br>$w_p = w_{rf}$ | $l_f \gg l_a$<br>$w_p \ll w_{rf}$ | Peak density limited by RF frequency, not self absorption |
| Density Profile | $l_f \ll l_a$<br>Spot size $\ll l_d$ | $l_f \gg l_a$<br>Spot size $\gg l_d$ | Does not resolve for 1-dimensional absorption and is dominated by diffusion effects |
| Shape Control | $l_{rf} \sim$ Chamber size | Painting/scanning focus | Chamber size prevents focusing/painting |
| Ambient Winds | Enclosed chamber | Winds at 70 Km | No wind effects |

$l_f$ = RF focal length  $l_a$ = plasma absorption length  $l_d$ = diffusion length
$w_p$ = plasma frequency  $w_{rf}$ = RF frequency  $t_d$ = diffusion time

Figure 1.2. Significant Uncertainties Relative to AIM, Not Addressed by Available Experimental Data

## 1.2 Baseline Concepts

Using an AIM to achieve beyond-LOS RF transmission entails production of a plasma patch in the upper atmosphere at an orientation such that an HF or VHF signal emanating from below the patch will refract back toward the AIM's horizon (Figure 1.3). For a nominal AIM altitude of 70 km, the resulting transmission horizon is extended out beyond 1,000 km. The patch is created by a focused, high-power RF beam generated in the near field of the ground-based heater.

Results from theoretical analysis and numerical modelling indicate that a useful AIM consists of an ionized layer, with an electron density gradient increasing with altitude from the ambient state to a density with plasma frequency corresponding to the transmission frequency. The AIM layer is oriented with an inclination ($\sim 40°$-$45°$) and has a slight curvature to allow the wave to refract over a 15° elevation beamwidth, providing range coverage from 200 to 1,000 km. In addition, the AIM azimuth orientation is incrementally stepped over the desired range.

The size and orientation of the AIM relative to the spot size of the focused RF heater beam requires that the AIM creation be performed with a raster scanning procedure. As Figure 1.3 indicates, a complete AIM is formed by moving the heater focus along a stepped sequence of horizontal sweeps (each sweep produces a bar of ionization the width of the patch). The focal position is controlled so as to follow a surface contour with the desired azimuth and elevation orientation and a slight curvature to allow for beam divergence over the azimuth elevation required for surveillance. This procedure is referred to as "painting" and is notionally illustrated in Figure 1.3. Based on our current understanding of ionization physics, a typical AIM will require on the order of a 10 to 50 milliseconds to paint.
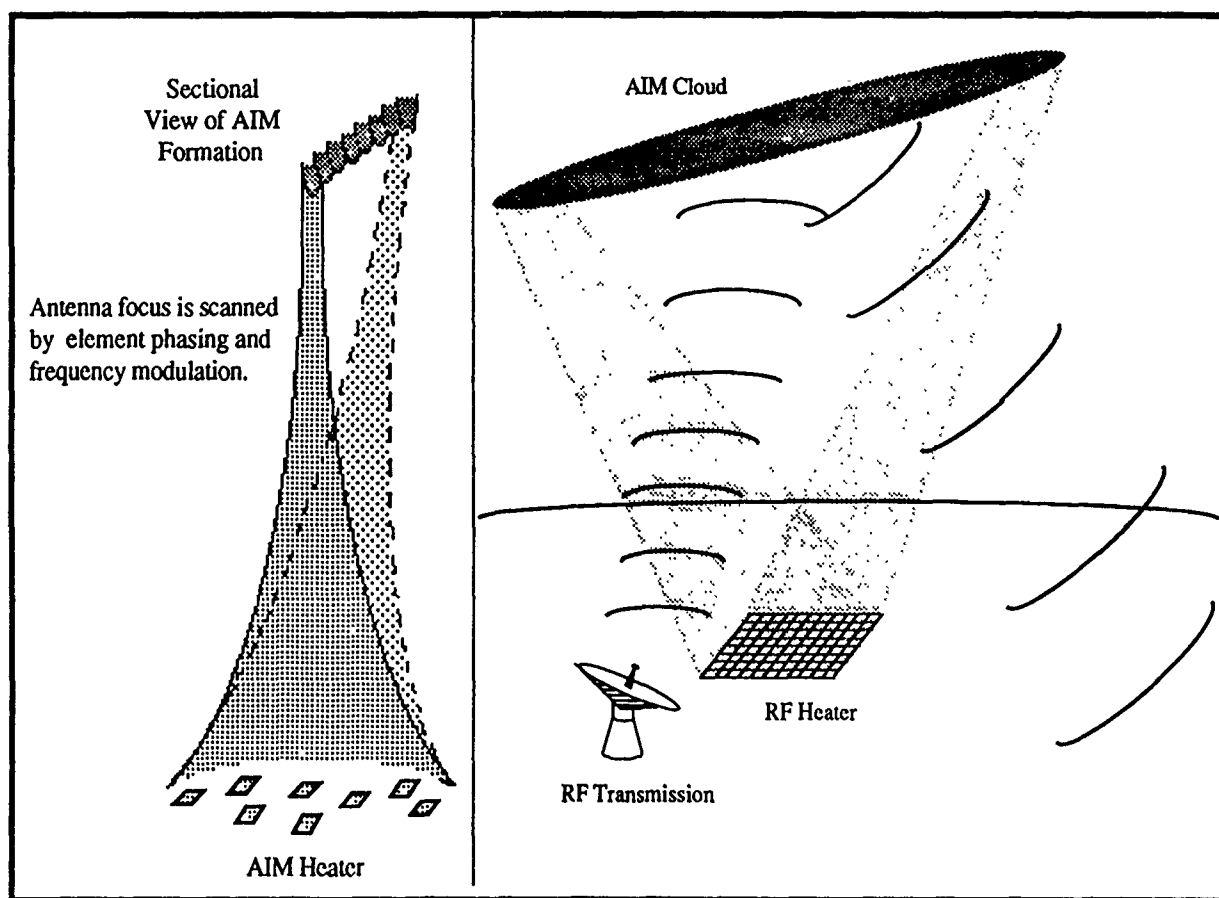


Figure 1.3. The Large, Sparse Heater Can Paint a Smooth, Homogeneous AIM Patch

A central issue concerned with evaluating the feasibility of the AIM concept is how reliably one can create the AIM within tolerances necessary for useful reflection of the RF signal. Issues that directly impact usefulness include: size, shape, orientation, uniformity, smoothness, peak electron density, steepness of the density gradient, and density lifetime.

In order to adequately address these issues, one needs a comprehensive understanding of the physics phenomenology (validated experimentally) and a careful analysis of the heater system design parameters as they impact plasma formation control. These topics have been the major focus of investigations up to this point. Specific results of these studies are presented in the following discussions.

By applying the results of the research performed by APTI the feasibility and utility of the AIM concept as a key element in an operational system can be examined. Considerable improvement in the understanding of the basic phenomenology of creation and dynamics of the ionized mirror led to innovative and practical approaches for the creation of stable, long-lived ionospheric mirrors.

## 1.3 Report Organization

This interim report is organized in parallel with the contract statement of work. After the current section (1.0 Introduction) is 2.0 Review of Relevant Theoretical and Experimental Efforts which discusses briefly the history and state of the art in atmospheric breakdown physics. Section 3.0, Theoretical Models of Ionization addresses the details of the study of the physics of the atmospheric ionization process. The concept for producing the AIM is treated in the next section, 4.0 Formation, Maintenance, and Control of an AIM. The alteration of the electromagnetic wave by the patch is treated in the next section, 5.0 AIM Propagation Effects. Section 6.0 describes the Overall Simulation Model that is currently partially functional but still under development.

## 2.0 REVIEW OF THEORETICAL & EXPERIMENTAL EFFORTS

A large body of theoretical and experimental work exists on the subject of RF breakdown. Most of this work was motivated by the need to avoid breakdown in RF transmission systems, for example, in waveguides and near antennas. For this purpose, easily observable criteria such as the presence of visible light emission are sufficient to determine that breakdown has occurred. In contrast to this, an AIM system must cause a controlled breakdown, generating a certain desired electron concentration over a specified three dimensional region. Development of the knowledge required to design an AIM system requires a thorough theoretical analysis of the breakdown process, and confirmation of the theoretical predictions requires more detailed data than most conventional breakdown experiments provide. The following section reviews the existing theoretical and experimental efforts which are relevant to RF breakdown, and discusses the limitations of these approaches with respect to AIM.

The first microwave breakdown experiment, in air and other gases, was carried out in 1948 by Herlin and Brown. This pioneering work was followed by numerous continuous wave (CW) and pulsed microwave breakdown experiments. However, the majority of these experiments concentrated on measuring the microwave breakdown field, or the microwave breakdown power, as a function of the gas pressure. Breakdown was generally considered to be a threshold, rather than a continuous increase in the electron production rate. Furthermore, there have been very few experiments where the microwave electron production rates have been directly measured as a function of the microwave field either in air or any other gases.

As for the concept of microwave breakdown, and the breakdown electric field, there seems to be no unique definition of breakdown. However, several qualitative and quantitative definitions have been used so far. Confining the discussion to the pulsed microwave breakdown experiments, several criteria have been advanced in regards to breakdown in air. Qualitatively, breakdown is said to occur when the microwave field reaches a level which induces a glow or visible light emission in air. Quantitatively, two definitions have been most often utilized:

7

- When the ratio of the final electron density to the initial density is

$$\frac{N_e(t_f)}{N_e(t_o)} = 10^8. \tag{2.1a}$$

- when the electron density reaches the critical density (ie. the plasma frequency equals the wave frequency) or

$$N_e(t_f) = 1.2 \times 10^{-8} f^2, \tag{2.1b}$$

where $f$ is the frequency of the microwave radiation.

This section reviews previous experimental ionization rate measurements, as well as the existing theoretical approaches for ionization rate calculations, provides a critical comparison of the available data, summarizes the current status of the data and makes recommendations for further measurements in this area.

## 2.1 Review of Ionization Rate Measurements

In microwave air breakdown experiments, the electron density grows exponentially during the microwave pulse, starting from seed electrons of unknown density. The seed electrons are generated by cosmic rays or by a radioactive source in the laboratory as is the practice in controlled experiments. The equation which describes the rate of growth of the electron density $N_e$ is

$$\frac{dN_e}{dt} = (v_i - v_a - v_d) N_e \tag{2.2}$$

where $v_i$, $v_a$ and $v_d$ are ionization, attachment and diffusion rates, respectively, which control the rate of electron density change. These rates, in general, depend on the electron energy and have to be obtained from an appropriate electron energy distribution which, in turn, must be known or calculated by solving a Boltzmann Equation. However, it is usually assumed that these rates are constant during breakdown, which facilitates the integration of equation (2.2), resulting in

$$N_e(t_f) = N_e(t_o) e^{v\tau}, \tag{2.3}$$

where $v = v_i - v_a - v_d$, $N_e(t_o)$ is the electron density at the beginning of the pulse ($t = t_o$), and $\tau = t_f - t_o$ is the duration of the microwave pulse. Equation (2.3) can be rewritten as

$$v_{net} = v_i - v_a = \frac{1}{\tau} \ln\left\{\frac{N_e(t_f)}{N_e(t_o)}\right\} + v_d \qquad (2.4a)$$

or

$$\frac{v_{net}}{P} = \frac{1}{P\tau} \ln\left\{\frac{N_e(t_f)}{N_e(t_o)}\right\} + \frac{v_d}{P}, \qquad (2.4b)$$

where $P$ is the pressure of the gas. When diffusion is negligible, breakdown experiments can be used to calculate $v_{net}/P$ by varying the electric field and the pulse length until breakdown occurs and then either substituting (2.1a) or (2.1b) into (2.4b). In the case of (2.1b), the initial electron density is either assumed to be 1 or is determined a priori. This approach has been used to calibrate $v_{net}/P$ as a function of $E_e/P$, where $E_e$ is the effective electric field which is defined by

$$E_e = E_{rms}\left(\frac{v_m^2}{v_m^2 + \omega^2}\right)^{1/2} \qquad (2.5)$$

In equation (2.5) $v_m$ is the collision frequency for momentum transfer by electrons to the air molecules. This approach, along with other assumptions in regards to some relevant parameters, has been utilized in the previous experiments where ionization rates have been determined.

The first microwave air breakdown experiments, pioneered by Herlin and Brown [Herlin and Brown, 1948] determined the ionization coefficient as a function of $E/P$ under CW conditions. However, the first pulsed microwave air breakdown and ionization rate measurements were made by Gould and Roberts [Gould and Roberts, 1957]. They defined the breakdown field as the field necessary to generate light in the discharge, and assumed that a certain electron density was achieved for the duration of the microwave pulse. They further assumed that the ratio of this electron density to the initial seed electrons was $10^8$, a number which gave good agreement between theory and experiment. Their single pulse breakdown results were given in the usual $P\tau$ vs. $E_e/P$ diagram where the effective field was calculated assuming a simple relationship between momentum transfer collision frequency and pressure, $v_m = 5.3 \times 10^9 P$. Furthermore, their measurements were based on single microwave pulses with durations of 0.4 - 2.0 μsec, a

microwave frequency of 2.8 GHz and an air pressure range of 25-300 Torr. All calculations were made assuming that diffusion is negligible. Some of these values are shown in Figure 2.1.
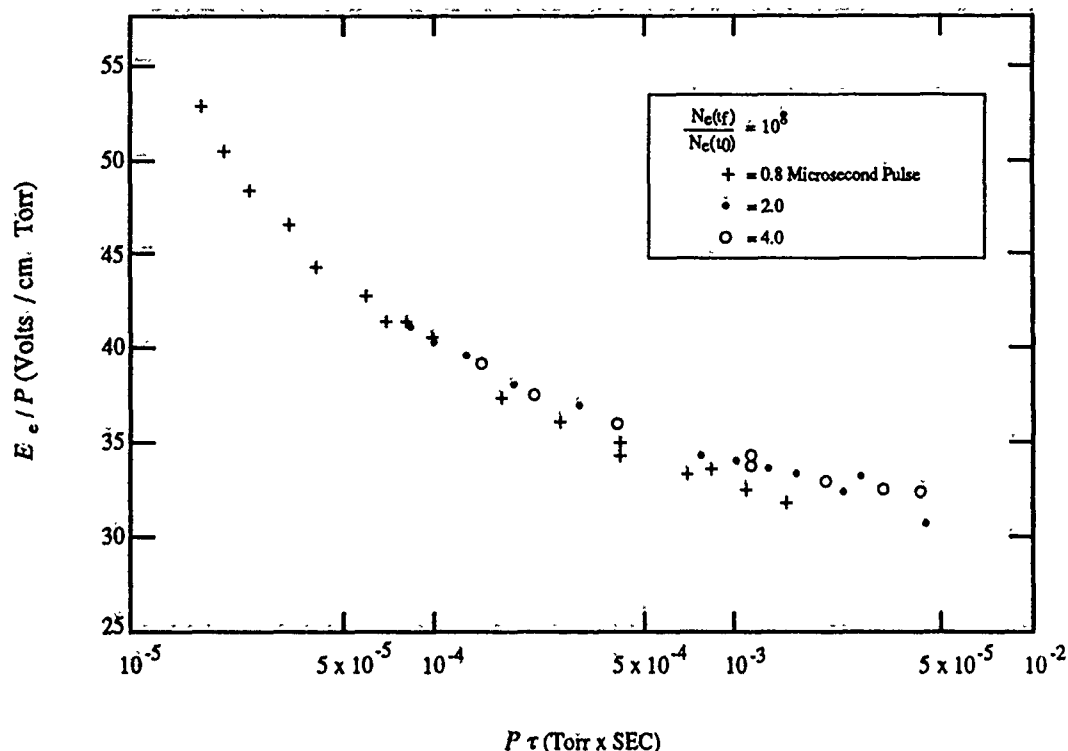


Figure 2.1. Typical Data from Gould and Roberts (1957)

Similar experiments by MacDonald [MacDonald et al, 1963] covered a range of frequencies in the L, X and K band in a number of resonant cavities. The pressures varied from .01 to 100 Torr. Pulsed measurements were made at .992 GHz, 9.3-9.4 GHz and 24 GHz, while CW were made at X and L bands. Pulse lengths in the range of .2-20µs were used. The seed ionization was produced by a radioactive source and the breakdown criterion was defined as the field at which the transmitted power is blocked during the last 5% of the pulse, which corresponds to reaching critical density. Typical experimental results are shown in Figure 2.2.
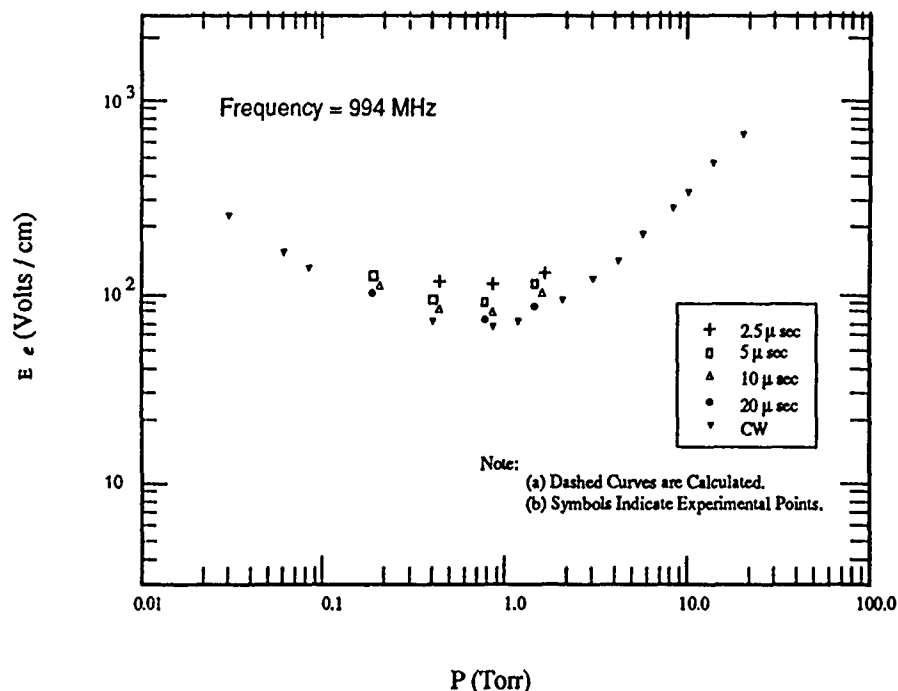
Figure 2.2. Typical Data from MacDonald (1963)

The next pulsed microwave ionization rate measurements in air were made by Scharfman and Morita [Scharfman and Morita,1964]. Here microwave radiation, with a frequency of 10 GHz, was focused in air (1-10 Torr) inside a large 4 ft diameter spherical Plexiglas chamber, to simulate open-air breakdown away from walls. The experimental conditions were chosen in such a manner to make diffusion effects negligible. In their analysis, Scharfman and Morita used a value of $10^8$ for the ratio of the electron density at breakdown to the initial seed electron density, and a value of $5.3 \times 10^9 P$ for the electron momentum transfer collision frequency. Their measurements of $V_{net}/P$ vs $E_e/P$ were in the range of $E_e/P$ from 32 to 75. However, in a later paper by Scharfman, Taylor, and Morita [Scharfman et al, 1964], ionization rates were presented for $E_e/P$ up to 170. In the second paper a somewhat different definition of the electron density at breakdown was utilized; it was equated with the electron density at the critical frequency (see equation (2.1)). Furthermore, the breakdown concept was defined either visually as the first sign of a glow in the chamber, or when there occurred a sharp drop in the microwave transmitted through the breakdown region. The ionization rates measured by Scharfman and Morita are shown in Figure 2.3, along with data from several other sources.
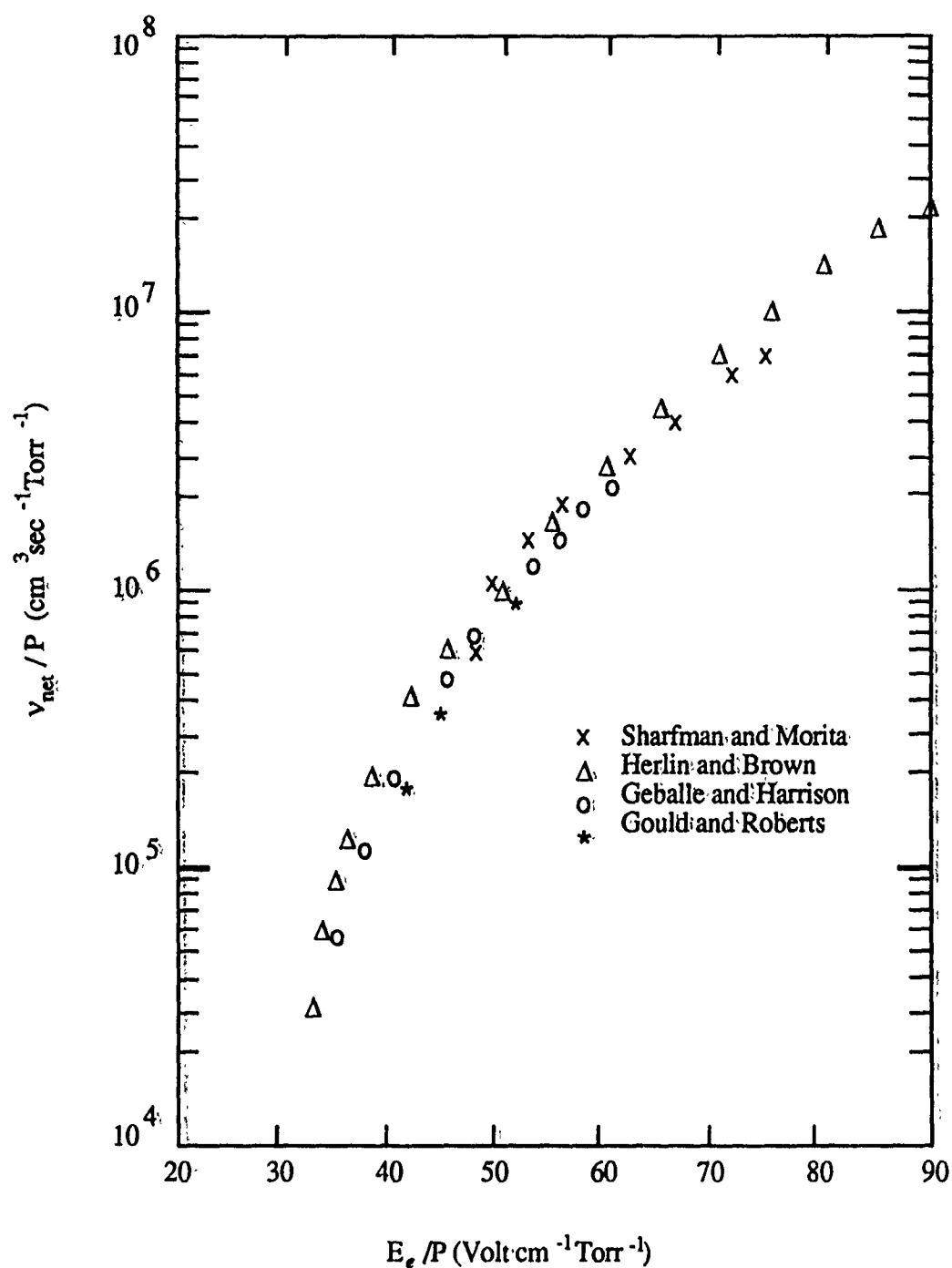
Figure 2.3. Composite of Pulsed Breakdown Measurements

Experiments by Tetenbaum [Tetenbaum et al, 1971] utilized two S-band cavities resonant at 3.062 GHz with $\Lambda = .391$ cm and .718 cm. The pulse-width in these experiments was extremely short (.1-.6 $\mu$secs) and the pressure range 1-1000 Torr. The preionization source

was UV light from a synchronized pulse discharge and the breakdown criterion was similar to the MacDonald experiments mentioned above.

In 1976 Lupan [Lupan, 1976] presented a theoretical approach for the calculations of $v_{net}/P$ vs $E_e/P$, assuming a Maxwellian electron velocity distribution. Lupan also reported on the ionization rate measurement of $v_{net}/P$ vs $E_e/P$ in the $E_e/P$ range from 30 to 100 under pulsed microwave breakdown conditions in air. The breakdown experiments were performed using microwave pulse lengths of 0.55 µsec to 10 µsec and air pressures of 0.5 to 18 Torr. The experimental set up was similar to that of Scharfman and Morita where open-air like breakdown occurs away from the walls. In the analysis of the experimental data Lupan used assumptions similar to those used by others, i.e., $v_m = 5.3 \times 10^9 P$ and ratio of initial to final electron concentration of $10^8$. The results of these measurements for $v_{net}/P$ vs. $E_e/P$ are shown in Figure 2.4 along with the previous measurements of Scharfman and Morita. Also shown in Figure 2.4 are the results based on Ali's [Ali,1986] theoretical approach in calculating $v_{net}/P$ vs. $E_e/P$ .
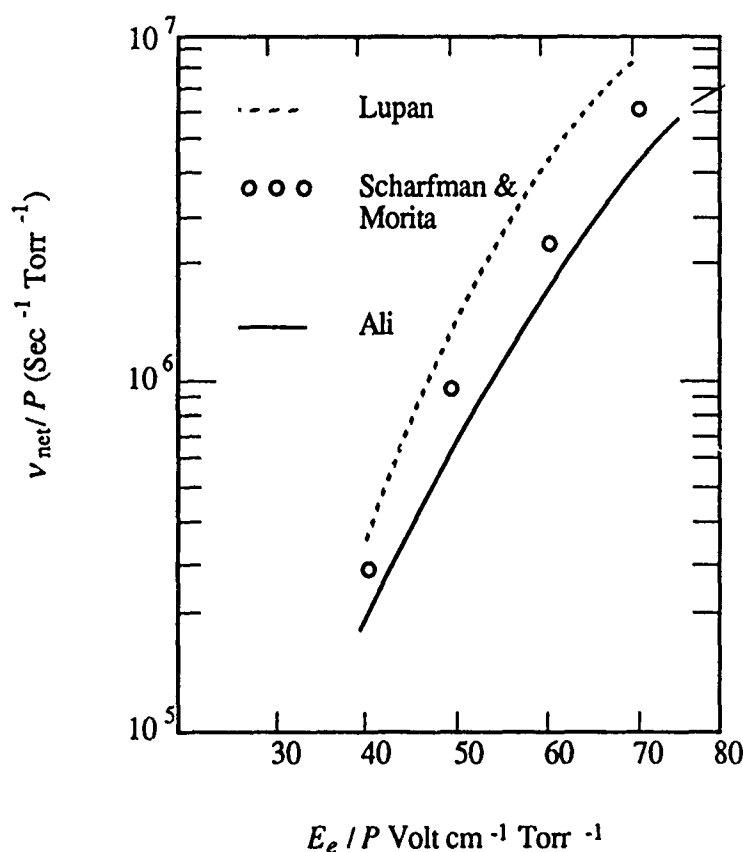


Figure 2.4. Typical Data from Scharfman and Morita and Lupan

13

A more recent Soviet experiment on open-air breakdown was performed by Karfidov et al [1981]. Microwaves with a frequency of 6 GHz were focused with the aid of a lens. The power was controlled by an attenuator to vary between $10^2$ and $7 \times 10^7$ W. The pulse duration was constant at 10 $\mu$s. Breakdown was recorded visually and defined on the basis of reaching critical density ($N_c = 4.5 \times 10^{11}$ cm$^{-3}$). Two preionization modes were used. The first was a radioactive source which was estimated to create an electron density of 1-10 cm$^{-3}$. The second was a glow discharge which produced about $10^9$ cm$^{-3}$. The results of the experiment are shown in Figure 2.5. Notice that the value of the electric field used is a theoretical estimate since the field at focus was not measured.
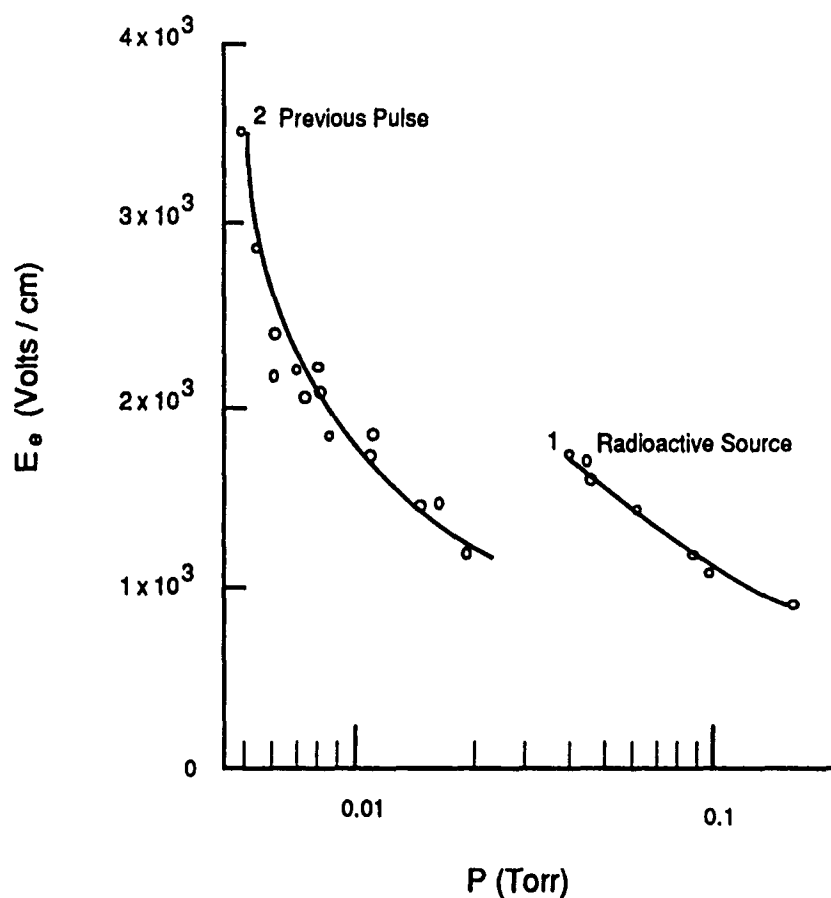


Figure 2.5. Typical Results from Karfidov (1981)

With the advent of high power microwave sources and short pulses, air breakdown experiments have been performed recently ([Byrne et al, 1983], [Didenko et al, 1985], [Hays et al, 1987], [Sullivan et al, 1988], and [Yee et al, 1986]) at $E_e/P$ values higher than 100 and with microwave pulse durations less than 100 nsec. These recent experiments have been motivated by the need to model short pulse high power microwave propagation through the atmosphere. One of the striking results in these recent experiments is that the ionization rate $v_{net}/P$ vs. $E_e/P$ levels off faster at higher values of $E_e/P$ ($E_e/P > 100$) than is predicted by the often used formula given by Felsenthal and Proud [Felsenthal and Proud, 1965], [Felsenthal, 1966]. An explanation of this discrepancy and a formula which predicts the ionization rates at higher $E_e/P$ values, in good accord with experimental data, has been provided by Ali [Ali, 1986]. This and other theoretical aspects will be discussed in section 2.2.1.

A recent experiment designed to measure ionization rate in nitrogen ($N_2$) at high values of $E_e/P$ ($E_e/P$ = 144-3840) is described in [Hays et al, 1987]. In this experiment the growth of the electron density was monitored as a function of time which gives direct measurement of the ionization rate. This experiment employed electron cyclotron resonance heating in an attempt to predict ionization rates for DC breakdown, and directly measured the electron concentration during breakdown. This method should be compared with the previous methods where the results were based on an assumed value of initial electron density. These recent results for $N_2$, which should be equal to that for air at high values of $E_e/P$, are shown in Figure 2.6, along with other data which are discussed in the next section.
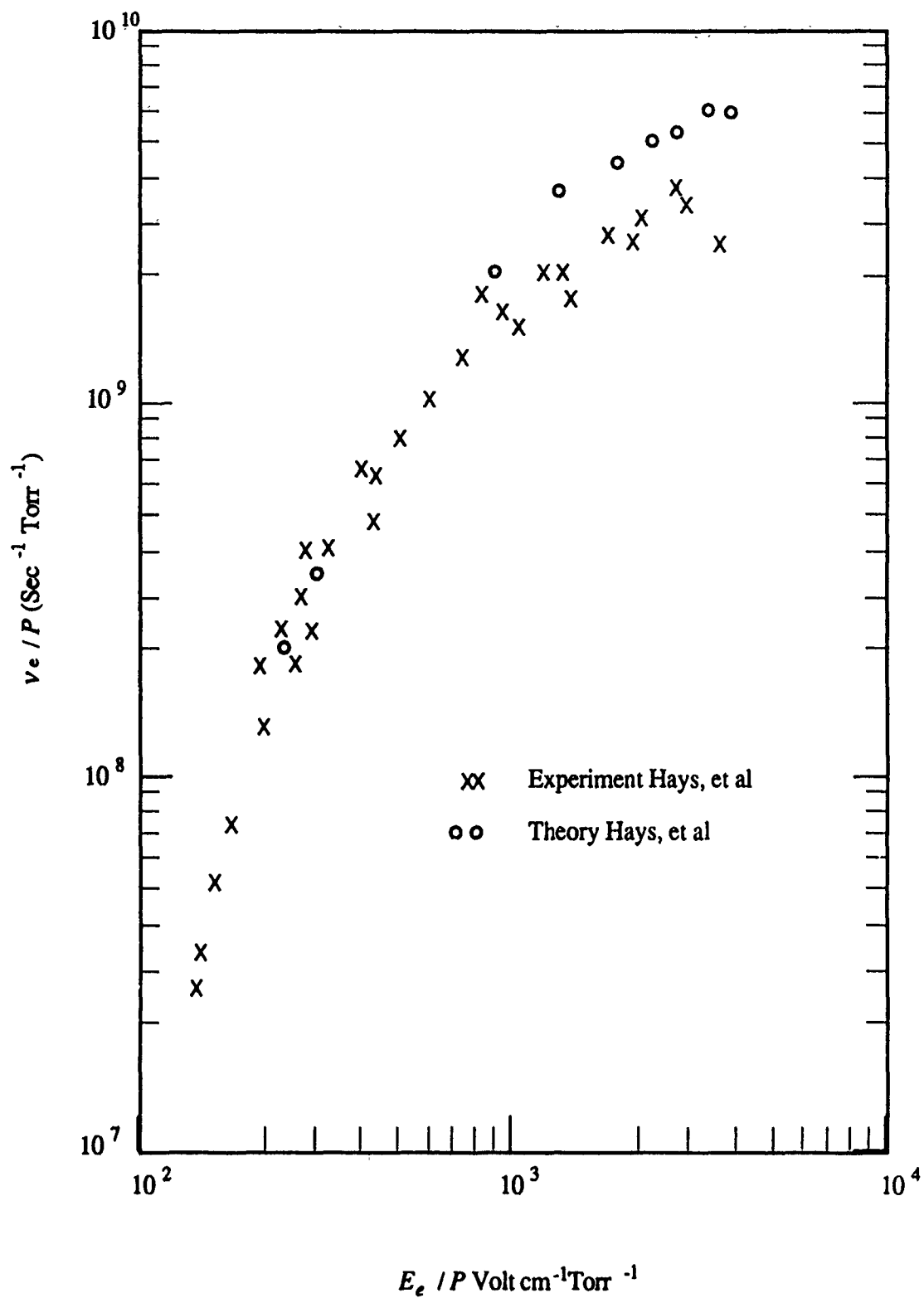
Figure 2.6. Experimental Data and Theory from Hays (1987)

16

## 2.2 Theoretical Methods for Calculating the Electron Production Rate

The net electron production rate in the absence of diffusion is given by

$$v_{net} = v_i - v_a \tag{2.6}$$

For a plasma in air, the ionization and attachment rates are given by

$$v_i = 4\pi \int_0^\infty v^3 f(v) \left(N_{N_2}\sigma_{iN_2}(v) + N_{O_2}\sigma_{iO_2}(v)\right) dv \tag{2.7}$$

and

$$v_a = 4\pi N_{O_2} \int_0^\infty v^3 f(v) \, \sigma_{aO_2}(v) \, dv, \tag{2.8}$$

where $N_{N_2}$ and $N_{O_2}$ are the number densities of nitrogen and oxygen, $\sigma_{iN_2}$ and $\sigma_{iO_2}$ are their ionization cross sections, $\sigma_{aO_2}$ is the oxygen attachment cross section, and $f(v)$ is the electron velocity distribution function, which has been normalized according to

$$N_e = 4\pi \int_0^\infty v^2 f(v) \, dv. \tag{2.9}$$

There are three basic theoretical approaches to calculating the rate of electron production. The first is to equate the microwave field to an equivalent DC field, and use measured DC data to calculate the ionization rates. The second approach is to assume an analytic form for $f(v)$, develop analytic approximations for the cross-sections, and directly solve the rate integrals. We will refer to these two approaches as approximate methods. The third technique is to calculate $f(v)$ using the Boltzmann equation

$$\frac{\partial f(v)}{\partial t} = -\frac{e}{3mv^2}\frac{\partial}{\partial v}\left(D(v,\omega,E)\frac{\partial f(v)}{\partial v}\right) - L(f(v)), \tag{2.10}$$

where $D(v,\omega,E)$ is a velocity diffusion term describing the accelerating effects of the electric field $E$, and $L(f(v))$ is an operator describing the effects of collisions on $f(v)$. This is a kinetic calculation. All of these methods are discussed in detail in the sections below.

17

### 2.2.1 Approximate Methods

The first approach utilizes the concept of the effective field as defined by equation (2.5), which replaces the actual field $E_{rms}$ by an effective DC field $E_e$. For a DC field, the net ionization rate is given by

$$\nu_{net} = \alpha \, \nu_d \tag{2.11}$$

where $\alpha$ is the Townsend ionization coefficient ($cm^{-1}$) and $\nu_d$ the electron drift velocity. Measured values of $\alpha$ and $\nu_d$ are available as a function of $E_{DC}/P$, and these can be used to obtain the net ionization rates as a function of $E_{DC}/P$. In order to apply the corresponding results to the microwave ionization, one replaces the RF field by the effective DC field $E_e$ [Felsenthal and Proud, 1965].

The use of the effective field may be justified in terms of the Boltzmann equation. Rewriting (2.10) in terms of energy gives

$$\frac{\partial f(\varepsilon)}{\partial t} = \frac{1}{\sqrt{\varepsilon}} \frac{\partial}{\partial \varepsilon} \left[ \varepsilon^{3/2} \, D(\varepsilon,\omega,E) \frac{\partial f(\varepsilon)}{\partial \varepsilon} \right] - L(f(\varepsilon)). \tag{2.12}$$

For the DC case the value of $D(\varepsilon,\omega,E)$ is given by

$$D_{DC}(\varepsilon,E) = \frac{2}{3} \frac{e^2 E_{DC}^2}{m \, \nu_m(\varepsilon)}, \tag{2.13}$$

while for the microwave case

$$D_{AC}(\varepsilon,\omega,E) = \frac{1}{3} \frac{e^2 E_{rms}^2}{m} \left\{ \frac{1}{(\omega-\omega_c)^2 + \nu_m^2(\varepsilon)} + \frac{1}{(\omega+\omega_c)^2 + \nu_m^2(\varepsilon)} \right\} \nu_m(\varepsilon), \tag{2.14}$$

where $E_{rms}$ is the RMS field and $\omega_c$ is the electron cyclotron frequency. At the electron cyclotron resonance, $\omega = \omega_c$, and assuming $\omega > \nu_m$, we find

$$D_{ECR}(\varepsilon,\omega,E) = \frac{1}{3} \frac{e^2 E_{rms}^2}{m \, \nu_m(\varepsilon)}. \tag{2.15}$$

18

Here, as discussed by Hays [Hays et al, 1987], the ECR case is equivalent to the DC case with an effective field $E_e = E_{rms}/\sqrt{2}$. For the microwave case where $\omega \gg \omega_c$, we find

$$D_{Ac}(\varepsilon,\omega,E) = \frac{2}{3} \frac{e^2 E_{rms}^2}{m \, v_m(\varepsilon)} \frac{v_m^2(\varepsilon)}{v_m^2(\varepsilon) + \omega^2} . \qquad (2.16)$$

Defining the effective electric field as

$$E_e \approx E_{rms} \left( \frac{v_m(\varepsilon)^2}{v_m(\varepsilon)^2 + \omega^2} \right)^{1/2}, \qquad (2.17a)$$

we can replace $E_{DC}$ by $E_e$ in (2.13) and reproduce (2.16). In comparing equation (2.5) with (2.17a), we see that a strictly correct use of the effective field concept requires knowledge of $v_m(\varepsilon)$ for all electron energies. However, in practice, it has been found that approximating $v_m(\varepsilon)$ by a nominal value, such as its average, $\overline{v}_m$, over the electron energy distribution gives good agreement with experimental measurements. Using this approximation for $v_m(\varepsilon)$, $E_e$ is given by

$$E_e \approx E_{rms} \left( \frac{\overline{v}_m^{\,2}}{\overline{v}_m^{\,2} + \omega^2} \right)^{1/2} . \qquad (2.17b)$$

Typically, $\overline{v}_m$ is either calculated from the assumed $f(\varepsilon)$, or it is assumed to be independent of energy. It is important to note that the use of the effective field concept is strictly valid only when $v_m$ is independent of energy, and that this is never exact for air.

The effective field approach has been used by Felsenthal [Felsenthal, 1966] and Ali [Ali, 1986]. This procedure results in the following expressions, as given by Ali,

$$\frac{v_{net}}{P} = \left[ 5.0 + 0.19 \left( \frac{E_e}{P} \right) \right] \times 10^7 \, exp \left( -273.8 \frac{P}{E_e} \right) \qquad (2.18)$$

for $120 \geq E_e/P > 54$, and

$$\frac{v_{net}}{P} = 54.08 \times 10^6 \left( \frac{E_e}{P} \right)^{1/2} exp \left( -359 \frac{P}{E_e} \right) \qquad (2.19)$$

for $3000 \geq E_e/P \geq 120$.

To obtain the effective field one requires the value of $E_e/P$ (see equation (2.5)); values of $V_m$ at breakdown are assumed to be constant and are obtained either phenomenologically [MacDonald, 1966], [Felsenthal, 1966] as $V_m = 5.3 \times 10^9 P$, or by assuming a Maxwellian velocity distribution [Ali, 1986] and calculating the electron temperature as a function of $E/P$. The results from equations (2.18) and (2.19) are shown in Figure 2.7 and are compared with the predictions of Felsenthal and Proud, where a discrepancy is obvious at values of $E/P \geq 100$. This discrepancy is due to the fact that Felsenthal and Proud obtained an expression for the electron drift velocity based on experimental data in the range of $E/P$ from 0.5 to 20 volt cm$^{-1}$ Torr$^{-1}$, which is linear in $E/P$. The extrapolation of this expression to higher values of $E/P$ is not valid because the drift velocity varies [Schlumbohm, 1965] as $(E/P)^{1/2}$ for $E/P > 100$, a fact reflected in equation (2.19).
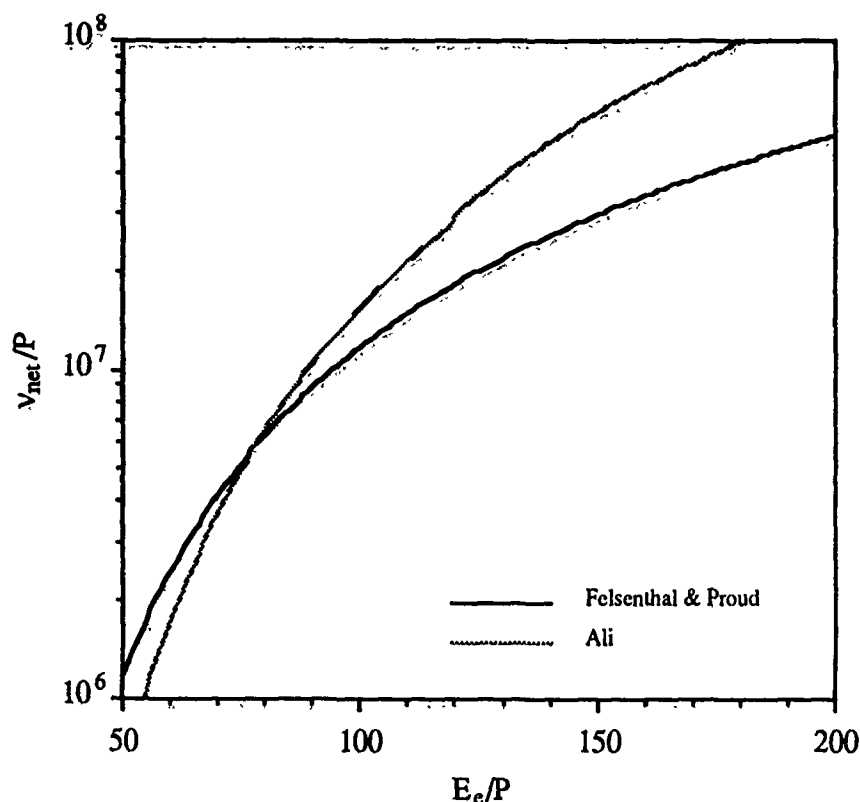


Figure 2.7. Comparison of Analytic Formulas from Felsenthal and Proud and Ali

The second group of approximate methods rest upon an assumed form of the electron velocity distribution function $f(v)$, or, equivalently, the energy distribution function $f(\varepsilon)$. The most common assumed distribution is the Maxwellian, with a temperature determined

by the effective field. Often, the form of the distribution and its relation to the field intensity is selected to provide the best match to experimental data.

This theoretical approach is typified by Lupan [Lupan, 1976], who assumed a Maxwellian distribution for the electrons and utilized the measured cross sections of $N_2$ and $O_2$ to obtain the ionization rate as a function of the electron energy. An estimate of the equivalent electron temperature $T_e$ was made so that calculated rates based on a Maxwellian distribution matched the measured rates. The resulting relation is

$$T_e = 0.0675 \frac{E_e}{P}. \tag{2.20}$$

The ionization rate as a function of $E_e/P$ obtained by Lupan is limited to $T_e \leq 20$ eV and valid for $E_e/P \leq 100$ with the assumption that $v_m = 5.3 \times 10^9 P$ can be expressed as

$$\frac{v_{net}}{P} = 2.5 \times 10^7 \left[ 1.45 \left( \frac{E_e}{P} \right)^{1/2} + 0.01 \left( \frac{E_e}{P} \right)^{3/2} \right] exp \left( -\frac{278 \, P}{E_e} \right). \tag{2.21}$$

This expression for the ionization rate is shown in Figure 2.4 along with Ali's expression and experimental data.

## 2.2.2 Validity of Approximate Techniques

The validity of the approximate techniques discussed above rests, in the first case, on the similarity of $f(\varepsilon)$ for the microwave case and for a DC case with the same effective field, and in the second case, on the similarity of the actual distribution to the assumed (usually Maxwellian) distribution.

The effective field approach relies on the assumption that the electron energy distribution function $f(\varepsilon)$ is similar in the microwave case and the equivalent DC case. The form of the distribution function in equation (2.12) is determined by the energy diffusion term $D(\varepsilon,\omega,E)$ and the loss operator $L(f(\varepsilon))$. Because $L(f(\varepsilon))$ does not depend on the intensity or frequency of the field, we would expect the effective field approximation to be useful when $D_{DC}(\varepsilon,E)$ and $D_{AC}(\varepsilon,\omega,E)$ have the same functional form. When $v_m(\varepsilon) \gg \omega$, equations (2.13),

21

$$D_{DC}(\varepsilon,E) = \frac{2}{3} \frac{e^2 E_{DC}^2}{m \, \nu_m(\varepsilon)}, \tag{2.13}$$

and (2.16),

$$D_{AC}(\varepsilon,\omega,E) = \frac{2}{3} \frac{e^2 E_{rms}^2}{m \, \nu_m(\varepsilon)} \frac{\nu_m^2(\varepsilon)}{\nu_m^2(\varepsilon) + \omega^2}, \tag{2.16}$$

show that the AC field behaves similar to a DC field with a field strength of $E_{rms}$. Assuming for the moment that $\nu_m$ is independent of energy and that $\nu_m = 5.3 \times 10^9 \, P$, this condition will be met when

$$f < P \tag{2.22}$$

with $f$ in GHz and $P$ in Torr. In this region, the energy dependence of the energization term for the DC and AC cases are similar, and we expect that the effective electric field concept will give reasonable results.

The maximum collision frequency is given by $\nu_{max} \approx 10^{10} \, P$. If $\omega > \nu_{max}$, the $\omega$ term in the denominator of (2.16) must dominate, and the energy dependence of the diffusion coefficient for this case will be

$$D_{AC}(\varepsilon) \propto \nu_m(\varepsilon) \tag{2.23}$$

which is completely different from the DC case, where

$$D_{DC}(\varepsilon) \propto \frac{1}{\nu_m(\varepsilon)} \tag{2.24}$$

This will result in different distribution functions for the AC and DC cases. As a result the effective field concept, and the rate predictions derived from it, are invalid when $\omega > \nu_{max}$, or equivalently, when

$$f > 2P \tag{2.25}$$

again with $f$ in GHz and $P$ in Torr.

In the case of methods which calculate the electron production rate from an assumed electron energy distribution $f(\varepsilon)$, difficulty arises from the need to simultaneously model the

22

actual distribution in the 6 eV region, in order to accurately calculate $v_a$, and the region above 12 eV, to calculate $v_i$. Measured $f(\varepsilon)$ for microwave breakdown are found to depart from Maxwellian in the high energy region, as described in the summary of experimental results below. This leads to errors in calculating the net electron production rate which may be as large as an order of magnitude.

Most of the relevant experimental investigations of the validity of these approximate techniques were conducted in the USSR ([Kal'vina et al, 1968], [Brassem et al, 1976], [Maksinov, 1967], [Babaly'ants, 1976], [Ivanov et al , 1977]). With the exception of Ivanov, the investigations examined whether the equivalent DC and microwave discharges produced the same value of average energy $\bar{\varepsilon}$. They found that under a variety of conditions the values of $\bar{\varepsilon}$ for microwave plasmas were much larger than the equivalent positive column glow discharge [Maksimov, 1967], [Babaly'ants, 1976]. Furthermore, while microwave discharge in inert gases, where $v_m$ is essentially independent of energy, were found to have a Maxwellian $f(\varepsilon)$ [Franklin et al, 1968], $f(\varepsilon)$ was highly non-Maxwellian for $N_2$ discharges [Babaly'ants et al, 1976]. A careful experiment was conducted by Ivanov [Ivanov et al, 1977] to investigate $f(\varepsilon)$ for equivalent microwave and DC glow discharges. They used 2.4 GHz microwaves with 50-300 W power and a pressure range 1-5 Torr in $N_2$ gas. They found that for microwave power of 1-2.5 W/cm$^3$ the values of $\bar{\varepsilon}$ were 2.4, 2.0 and 1.7 eV at pressures of 1, 2 and 5 Torr. These values were approximately the same for equivalent DC glow discharges. However, the electron energy distributions were radically different. For the microwave plasma $f(\varepsilon)$ was approximately Maxwellian at energies up to 8 eV, while the DC glow discharge had a Druyvesteyn distribution and approached Maxwellian only for high discharge currents. Furthermore at energies above 8 eV the microwave distribution had strong non-Maxwellian tails, the departure from Maxwellian reaching an order of magnitude at $\varepsilon > 15$ eV. The study concluded that although the two types of discharges result in the same average energy per electron $\bar{\varepsilon}$, the ionization rates can differ by more than an order of magnitude under "equivalent" conditions.

Many of the cases of interest for this study fall outside the range of validity of conventional effective field formulations. For example, the ionization rate of a 0.5 GHz (500 MHz) heater at an altitude of 70 km, where $P = 0.05$ Torr, cannot be reliably predicted using standard effective field formulations. Analytic approaches which assume a particular $f(\varepsilon)$ have also been found to be unreliable in the prediction of microwave ionization rates,

particularly in the region near the breakdown threshold. For this reason, the kinetic approach to calculation of the electron production rate was selected.

## 2.2.3 Kinetic Calculations

The kinetic approach requires solution of the Boltzmann equation for $f(v)$ as a function of time,

$$\frac{\partial f(v)}{\partial t} = -\frac{e}{3mv^2}\frac{\partial}{\partial v}\left(D(v,\omega,E)\frac{\partial f(v)}{\partial v}\right) - L(f(v)). \tag{2.10}$$

For air breakdown, the operator $L$, which describes the losses due to inelastic and elastic collisions, is determined by complex cross-sections for various processes. Analytic solution of this equation is not possible; numerical techniques must be used.

The use of the Boltzmann equation to determine the energy distribution of a nonuniform gas was described by Chapman and Cowling [Chapman and Cowling, 1939], and the application of these methods to ionization processes was described in detail by W. P. Allis [Allis, 1956]. The treatment described by Allis, which includes the expansion of the electron velocity distribution function in spherical harmonics and the use of the Fokker-Planck treatment of Coulomb collisions, has been widely used, and is developed to a high degree of detail by, for example, Shkarofsky, Johnston, and Bachynski [Shkarofsky et al, 1966], or Gurevich [Gurevich,1978].

A complete kinetic simulation of the ionization process in air has been developed, which includes the effects of elastic collisions, 2 and 3 body attachment, dissociation, ionization, and the excitation of rotational, vibrational and electronic (optical) resonances. The most accurate empirical cross-section data have been employed throughout. This simulation is described in detail in Section 3.

## 2.3 Fits to Experimentally Obtained Ionization Rates

In addition to theoretical attempts to predict electron production rates, many attempts have been made to develop empirical formulas by fitting experimental data. These approaches generally use the effective field concept, and it is important to note that the limitations of the

24

theoretical approach, where $E_e$ is equated with a DC field, also apply to these empirical efforts. An approach which uses the effective field concept cannot be used to predict electron production rates outside of the $v_m(\varepsilon) > \omega$ regime, unless it is based on measurements made outside that regime. This is because the shape of the energy distribution function changes, and identical values of $E_e/P$ will give different electron production rates in the two regimes. The relationships between $v_{net}/P$ and $E_e/P$ developed in the studies discussed below are based on data taken when $v_m(\varepsilon) > \omega$, and should not be used outside that regime.

Suitable fits to the experimental data have been found by Bisbing [Bisbing et al, 1968], and by Mayhan and Fante [Mayhan and Fante, 1969]. The corresponding fits are given by equations (2.26) and (2.27), respectively

$$\frac{v_{net}}{P} = 4 \times 10^7 \frac{(E_e/P)}{100} - 6.4 \times 10^4 \qquad (2.26)$$

and

$$\frac{v_{net}}{P} = 8.35 \times 10^{-4} \left(\frac{E_e}{P}\right)^{5.34}. \qquad (2.27)$$

These fits are found to be useful ([August, 1988], [Woo and DeGroot, 1984]) for estimating breakdown power and other calculations. However, it should be noted that these fits are based on experimental data of Figure 2.1 which are basically in a limited range of $E_e/P$. Therefore, the extrapolation of these fits beyond their limits (10 - 90 volt cm$^{-1}$ Torr$^{-1}$) will result in erroneous answers.

## 2.4  Summary and Conclusions

Based on the review of the experimental and theoretical data for the pulsed microwave ionization rates in air, it is clear that there are a limited number of measurements whose results are useful, and these are limited to the region where $v_m/\omega > 1$, and to values of $E_e/P$ below 100 volt cm$^{-1}$ Torr$^{-1}$. A recent measurement in nitrogen (N$_2$) spans a wide range in $E_e/P$ (150 - 4,000 volt cm$^{-1}$ Torr$^{-1}$), however, it is a gyroresonance heating experiment. All the relevant experimental data are shown in Figures 2.1-2.6. These figures show the current status of the ionization rate measurements. They show the degree of scatter in the data, which is roughly 50% in the calculated electron production rate. Table 2.1 below

compares the differences between the parameter regime in which most measurements have been taken and the regime important for AIM.

Table 2.1. Comparison Between Experimental Regime and AIM

|  | Experiment Regime | AIM Regime |
|---|---|---|
| $E_e/P$ | < 100 | > 100 |
| $v_m/\omega$ | >1 | < 1 |
| Effective field concept valid | Usually | Usually Not |
| Diffusion important | Usually | No |

It is evident that microwave ionization rate measurements need further study if they are to provide data for AIM design, especially for $v_m/\omega > 1$ and $E_e/P \geq 100$. Future studies, however, must rely on new methods where the results are not dependent on a priori assumptions about initial electron density. The interferometric method used by Hays is one such method which should be exploited.

# 3.0 THEORETICAL MODELS OF IONIZATION

In this section, a brief qualitative description of the ionization process is given, followed by the derivation of a kinetic equation for calculating the electron velocity distribution function $f(r,v,t)$. A simpler analytic approximation, based on a test particle approach, is presented. The computational solution of the kinetic equation is then described, and the results of the computations are compared with the analytic approximation and with experimental data.

## 3.1 The Ionization Process

An electron under the influence of an oscillating electric field with peak amplitude $E_0$ and frequency $\omega$ has a peak velocity of $eE_0/m\omega$, or equivalently, a peak quiver energy of

$$\tilde{\varepsilon} = \frac{1}{2} m \frac{e^2 E_0^2}{m^2 \omega^2} , \tag{3.1}$$

where $m$ is the mass of the electron, and $e$ is its charge. In practical units, the quiver energy in eV is given by

$$\tilde{\varepsilon} = 1.68 \times 10^{12} \frac{P}{f^2} , \tag{3.2}$$

where $P$ is the power density of the electric field in Watts per square meter, and $f$ is the frequency in Hertz. If the quiver energy is higher than the energy required to ionize (12.0 eV for $O_2$ and 15.6 eV for $N_2$), then an electron may acquire sufficient energy to ionize directly from the field. This requires very high power levels; for example, to reach a quiver energy of 12 eV with a 300 MHz electric field requires a power density of 640 kilowatts per square meter.

At lower power levels, the electron must be accelerated by either a gyrofrequency resonance or a series of momentum transfer collisions. Gyrofrequencies for the earth's magnetic field are in the 0.7 - 1.9 MHz range, thereby severely limiting electron density production and consequent plasma frequencies, due to strong self absorption of the wave at lower altitudes [Bailey, 1937, 1938; Clavier, 1961; Gurevich, 1965]. Since achievable electron densities have been determined to be much less than that required for a useful artificial mirror, further consideration of gyrofrequency ionization has not been pursued in this effort. The second mechanism for producing high energy electrons, momentum

transfer collisions, was first recognized by Lombardini [Lombardini, 1965] as a mechanism that would allow significantly higher RF heating frequencies, thus reducing the severity of the self absorption problem and obtaining useful levels of ionization.

As an electron, moving under the influence of the field, collides with a neutral molecule, its direction is altered (momentum transfered), and a portion of the quiver energy is converted to random (thermal) energy. This process of converting field induced quiver energy to randomly directed drift energy, if unimpeded by energy absorbing inelastic collisions, will cause the electron to accelerate to velocity levels required for ionization. A detailed kinetic approach to modeling this phenomenon requires calculating the electron distribution function $f(r,v,t)$. The function $f$ gives the expected number of electrons at position $r$, with velocity $v$, at time $t$. (Note that $v$ is in general a vector, because either overall motion of the entire population of electrons or the effects of an electric field may produce anisotropic velocity distributions.) The kinetic calculation must account for the effects of the electric field, motion of the electrons (e.g. winds or diffusion), and collisions between the electrons and all other species.

The time evolution of the electron velocity distribution function $f(r,v,t)$ within a given volume under the influence of an electric field and elastic and inelastic collisions is described by the Boltzmann equation

$$\frac{\partial f}{\partial t} = \frac{e}{m} E \cdot \frac{\partial f}{\partial v} - v \cdot \frac{\partial f}{\partial r} - S_{coll}. \qquad (3.3)$$

Here the left hand term represents the time rate of change of the distribution function, and the right hand terms represent the effects of all processes which change the distribution. The first term represents the addition of energy to the electron population by the electric field, the second term the change due to motion of electrons into and out of the test volume (note that this is zero if the plasma is uniform), and the final term represents the effects of collisions.

The following analysis of electron heating and consequent ionization is facilitated by a number of simplifying approximations to equation (3.3). The validity of these approximations is directly related to the assumed regime of physical parameters for an AIM system. The AIM concept relies on the formation of regions of plasma, of sufficient density to reflect HF/VHF signals between 30 MHz and 100 MHz, in the atmosphere

between 60 and 80 kilometers altitude. The electron density required to reflect signals at the frequencies of interest ranges from roughly $10^7$ to $10^8$ electrons per cubic centimeter, while the neutral density decreases from $7 \times 10^{15}$ at 60 kilometers to $3 \times 10^{14}$ at 80 kilometers. The desired fractional ionization is thus always below $10^{-6}$, and very often below $10^{-8}$ (it is $3 \times 10^{-9}$ for the baseline AIM system, which reflects a 50 MHz wave at a patch altitude of 70 kilometers.) We are therefore always dealing with a weakly ionized plasma, for which the effects of collisions between electrons, and between electrons and ions, may be neglected. In order to minimize the impact of self absorption, self focusing, and other plasma effects during ionization, the heater frequency should be approximately an order of magnitude higher than the desired electron density (eg. for a 30 MHz signal, the heater RF should be at least 300 MHz).

### 3.1.1 Expansion of the Electron Energy Distribution Function

It is apparent that the electron distribution function $f(r,v,t)$ will never be exactly isotropic in the presence of an electric field, since the motion of electrons parallel to the field is anisotropic. However, where the average thermal energy of an electron $\varepsilon_{th}$ is large compared to the energy of field-induced motion $\tilde{\varepsilon}$, the electron distribution function may be thought of as an isotropic distribution with a small anisotropic perturbation added.

A more rigorous approach which follows these lines is the expression of the distribution function as a sum of spherical harmonics in velocity space [Allis, 1956]. This yields an expression for $f$ as an infinite sum of terms, only the first of which is isotropic. If the thermal energy is indeed large compared to the quiver energy, then the series may be truncated after the first anisotropic term, yielding the set of equations [Gurevich, 1978]

$$\frac{\partial f_0}{\partial t} = -\frac{v}{3} \nabla f_1 + \frac{e}{3mv^2} \frac{\partial}{\partial v}\left(v^2 \, E f_1\right) - S_0 \tag{3.4}$$

and

$$\frac{\partial f_1}{\partial t} = -v \, \nabla f_0 + \frac{eE}{m} \frac{\partial f_0}{\partial v} - S_1, \tag{3.5}$$

where $f_0$ and $f_1$ are the first two terms of the expansion of $f$, and $S_0$ and $S_1$ are the corresponding expansions of the collision integral $S_{coll}$. It is important to note that the isotropic velocity distribution $f_0$ has been normalized so that

29

$$N_e = 4\pi \int_0^\infty v^2 f_0(v) \, dv \qquad (3.6a)$$

or

$$N_e \doteq K \int_0^\infty \sqrt{\varepsilon} f_0(\varepsilon) \, d\varepsilon, \qquad (3.6b)$$

where $K$ is a constant which accounts for the change in units from velocity to energy, and the notation $f_0(\varepsilon)$ means the value of $f_0$ at the velocity corresponding to energy $\varepsilon$. Other works have sometimes employed other normalizations, and care must be taken when comparing expressions. The references upon which this discussion is based, [Allis, 1956] and [Gurevich,1978], employ the normalization above.

In a weakly ionized plasma, the first anisotropic term $f_1$ of the expansion of the distribution function is given by [Gurevich, 1978]

$$f_1 = -u \frac{\partial f_0}{\partial v}, \qquad (3.7)$$

where $u$ is the directional velocity of the electrons due to the field. Substituting into the expression for $f_0$, we obtain

$$\frac{\partial f_0}{\partial t} = \frac{v}{3} \nabla \cdot \left( u \frac{\partial f_0}{\partial v} \right) - \frac{e}{3mv^2} \frac{\partial}{\partial v} \left( v^2 \, \mathbf{E} \cdot \mathbf{u} \, \frac{\partial f_0}{\partial v} \right) - S_0. \qquad (3.8)$$

In the first approximation, we will assume that the plasma is uniform. This removes the divergence term, leaving

$$\frac{\partial f_0}{\partial t} = - \frac{e}{3mv^2} \frac{\partial}{\partial v} \left( v^2 \, \mathbf{E} \cdot \mathbf{u} \, \frac{\partial f_0}{\partial v} \right) - S_0. \qquad (3.9)$$

This is a differential equation for the isotropic portion of the distribution function of a uniform weakly ionized plasma. When the quiver energy is below the energy required for ionization, the isotropic portion of the distribution is responsible for all ionization which occurs; therefore, it is the form of $f_0$ which determines the ionization rate. At quiver energies below 2-3 eV, the form of the isotropic portion of the distribution also determines the rate of collisions which excite optical resonances and cause dissociation, and the rate of collisions which result in attachment. Since these are the dominant energy and electron

30

loss mechanisms, $f_0$ may be used to accurately calculate the net rate of electron production. To solve this equation for $f_0$, it is necessary to determine the form of $S_0$, the term which represents the effects of collisions. This is discussed in the following section.

### 3.1.2 The Effect of Collisions

The collision term $S_0$, which represents the effect of collisions on the isotropic portion of the distribution $f_0$, is the isotropic portion of the spherical harmonic expansion of the Boltzmann collision integral. $S_0$ describes the probability of the transformation of an electron with velocity $v$ into an electron of a different velocity $v'$ due to a collision. It may be decomposed into two parts: one representing the effects of elastic collisions, $S_{0el}$, and one for inelastic collisions, $S_{0in}$. Each of these will be dealt with separately in the following sections.

### 3.1.2.1 Elastic Collisions

Elastic collisions between electrons and neutral molecules occur through the mechanism of electrostatic repulsion between the free electron and the electrons in the outer shells of the molecule. Because these forces act over large distances, electron interactions with molecules tend to be composed of many scattering events, each of which alters the directional velocity $v$ of the electron by only a small amount. The elastic collision term may therefore be represented by the somewhat different Fokker-Planck form, rather than a Boltzmann integral. This corresponds to expanding the complete collision integral in powers of $| v - v' | = \Delta v$, the vector change in velocity due to the collision, and retaining only the first term [Allis, 1956].

A full treatment of elastic collisions must account for the energy lost by the electron due to recoil of the molecule, and for the possibility that the electron will gain energy from the molecule's thermal motion. The complete collision term for elastic collisions between electrons and neutral molecules is [Allis, 1956]

$$S_{0el} = -\frac{1}{2v^2}\frac{\partial}{\partial v}\left[ v^2\left(\delta v_m v f_0 + \delta v_m \frac{kT}{m}\frac{\partial f_0}{\partial v}\right)\right],\qquad (3.10)$$

where

$\delta$ = $2m/(M + m)$, the fractional electron energy loss per collision,

$M$ = mass of the neutral molecule,

$v_m$ = electron-neutral momentum transfer collision rate,
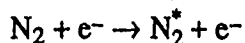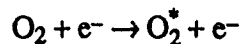
31

$k$ = Boltzmann's constant, and

$T$ = neutral temperature.

The first term within the inner parentheses represents the effect of collisions with motionless neutrals; the second term is a correction factor for neutrals with a Maxwellian velocity distribution of temperature $T$. It is important to note that, because of the very low levels of fractional ionization, only extremely inefficient ionization processes will alter the neutral temperature to any appreciable degree.
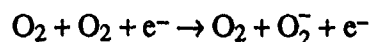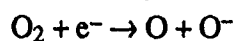
### 3.1.2.2 Inelastic Collisions

There are a large number of inelastic processes which may occur in the atmosphere. The most important of these are the following:

Excitation of atomic resonances (rotational, vibrational, and optical):
$$O_2 + e^- \rightarrow O_2^* + e^-$$
$$N_2 + e^- \rightarrow N_2^* + e^-$$

Attachment (2- and 3-body):
$$O_2 + e^- \rightarrow O + O^-$$
$$O_2 + O_2 + e^- \rightarrow O_2 + O_2^- + e^-$$

Dissociation:
$$O_2 + e^- \rightarrow O + O + e^-$$
$$N_2 + e^- \rightarrow N + N + e^-$$
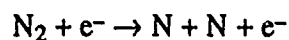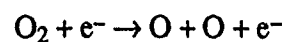
Ionization:
$$O_2 + e^- \rightarrow O_2^+ + 2e^-$$
$$N_2 + e^- \rightarrow N_2^+ + 2e^-$$
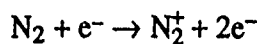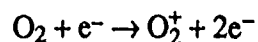
Several other processes have been excluded because the numbers of species available to participate are small. These include:

Superelastic collisions (de-energizing collisions with excited species):
$$O_2^* + e^- \rightarrow O_2 + e^-$$
$$N_2^* + e^- \rightarrow N_2 + e^-$$

Detachment:
$$O^- + e^- \rightarrow O + 2e^-$$
$$O_2^- + e^- \rightarrow O_2 + 2e^-$$

Recombination:
$$O_2^+ + e^- \rightarrow O_2$$
$$N_2^+ + e^- \rightarrow N_2$$

Efficient ionization requires that the losses due to excitation of high-energy resonances and attachment be kept small; this, combined with the low fractional ionization, makes the probabilities of superelastic collisions and detachment very low compared to the processes which are included. Excluding superelastic collisions and detachment produces a conservative estimate of the power required for a given electron production rate, because both of these processes aid electron production. The exclusion of recombination results in a slight overestimate of the production rate, but because of the very low fractional ionization, the error is negligible.
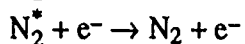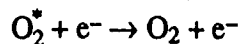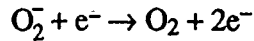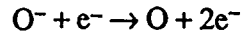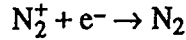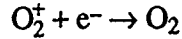
The total inelastic collision term may be written as a sum of terms due to each included process:

$$S_{0in} = S_{0in}^{rot} + S_{0in}^{vib} + S_{0in}^{opt} + S_{0in}^{dis} + S_{0in}^{att} + S_{0in}^{ion} \tag{3.11}$$

The form of the term describing each of these processes depends on whether the energy loss from the collision is small compared to the total electron energy, and whether the process modifies the total number of electrons. Each process will be considered in turn below.

If the energy loss due to an inelastic process is small compared to the total electron energy, the loss may be modeled as a continuous loss. This is the case for rotational excitations, where the effects may be described by [Gurevich, 1978]

$$S_{0in}^{rot} = -\frac{1}{2v^2} \frac{\partial}{\partial v} \left[ v^2 \left( \sum_k \frac{8 B_k N_k \sigma_k}{mv} \right) \left( v f_0 + \frac{kT}{m} \frac{\partial f_0}{\partial v} \right) \right], \tag{3.12}$$

where the summation is performed over $k$ species in the atmosphere, $N_k$ is the number density for species $k$, and $B_k$ and $\sigma_k$ are constants determined by the neutral species.

33

If the energy loss is not negligible compared to the electron energy, then a more general form of the expression describing the effects of the inelastic collision must be employed. For vibrational and optical resonances, and dissociation, the terms have the same form, and only the cross-sections change. Each term has the form

$$S_{0in}^{A} = -\frac{2}{mv} \sum_{k,j} N_k \left[ (\varepsilon + \varepsilon_{k,j}) f_0(\varepsilon + \varepsilon_{k,j}) \sigma_{Ak,j}(\varepsilon + \varepsilon_{k,j}) - \varepsilon f_0(\varepsilon) \sigma_{Ak,j}(\varepsilon) \right]. \quad (3.13)$$

Equation (3.13) describes the change in $f_0$ at electron energy $\varepsilon$, due to process $A$, which may be vibrational, optical excitation, or dissociation. Here the summation is performed over $j = 1,...,J$ energy levels for each of $k = 1,...,K$ species. $N_k$ is the neutral density for species $k$; $\varepsilon_{k,j}$ is the energy change associated with the $j$th level of the process in species $k$, and $\sigma_{Ak,j}$ is the cross-section for the $j$th level of process $A$ in species $k$. This expression has a simple interpretation: the first term in the inner brackets describes the influx of electrons at energy level $\varepsilon$ due to inelastic collisions at a higher energy $\varepsilon + \varepsilon_{kj}$; the second term is the loss of electrons at energy $\varepsilon$ to lower energies. The leading factor $2/mv$ arises from the change of variables in $f_0$.

The remaining processes, attachment and ionization, alter the total number of electrons. The expression for attachment is particularly simple

$$S_{0in}^{att} = -\left( N_{O_2} \sigma_{att2}(v) + N_{O_2}^2 \sigma_{att3}(v) \right) v f_0, \quad (3.14)$$

where $\sigma_{att2}$ and $\sigma_{att3}$ are the 2- and 3-body attachment cross-sections for $O_2$. This describes the removal of electrons at energies where the cross-section for attachment is large. The ionization term is given by

$$S_{0in}^{ion} = \sum_k \int_{v_{ion}}^{\infty} N_k v'^3 F_k(v,v') f_0 \sigma_{ion}(v') \, dv', \quad (3.15)$$

where $F_k(v,v')$ describes the probability that an electron of velocity $v$ will be produced by an ionizing collision of an electron at velocity $v'$ with a molecule of species $k$. Since 2 electrons remain after each ionizing collision, the integral of $F_k$ over all $v$ and $v'$ is 2.

34

### 3.1.2.3 Cross-Section Data

The cross-sections of the various elastic and inelastic processes described above determine the rates at which these processes occur for a given electron velocity distribution. To ensure the accuracy of the numerical calculations, a thorough review of available cross-section data for oxygen and nitrogen was performed. The cross-sections are revised versions of those given in [Ali, 1981], incorporating additional experimental data produced since then. The cross-section values are expected to be accurate to within 20%. The cross-sections are shown in the figures below, and represent the values which were used in the numerical solution of the Boltzmann equation.
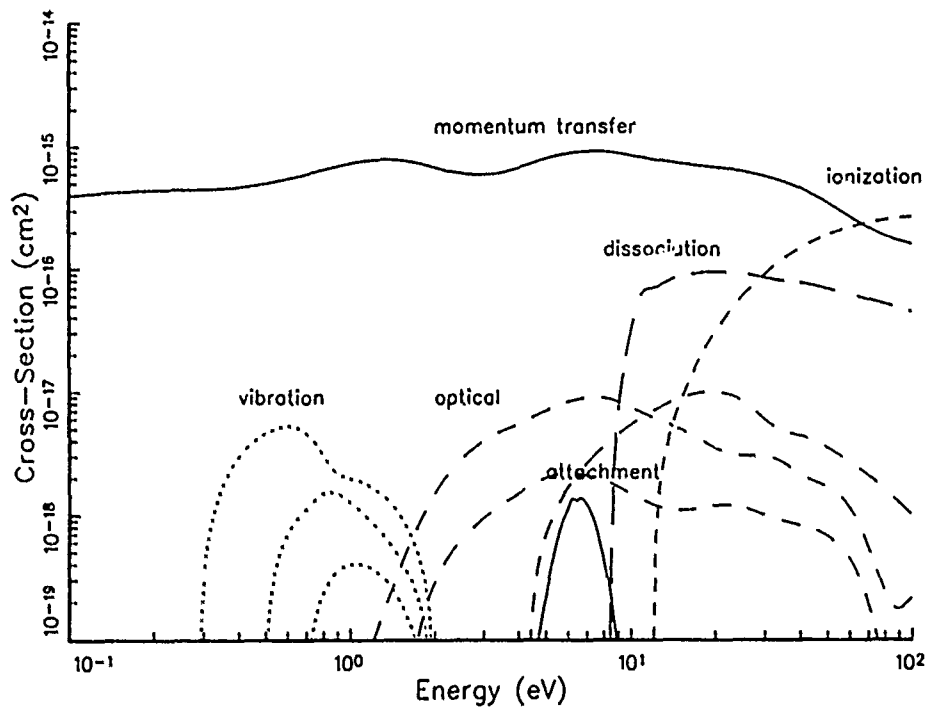


Figure 3.1. Oxygen Cross-sections
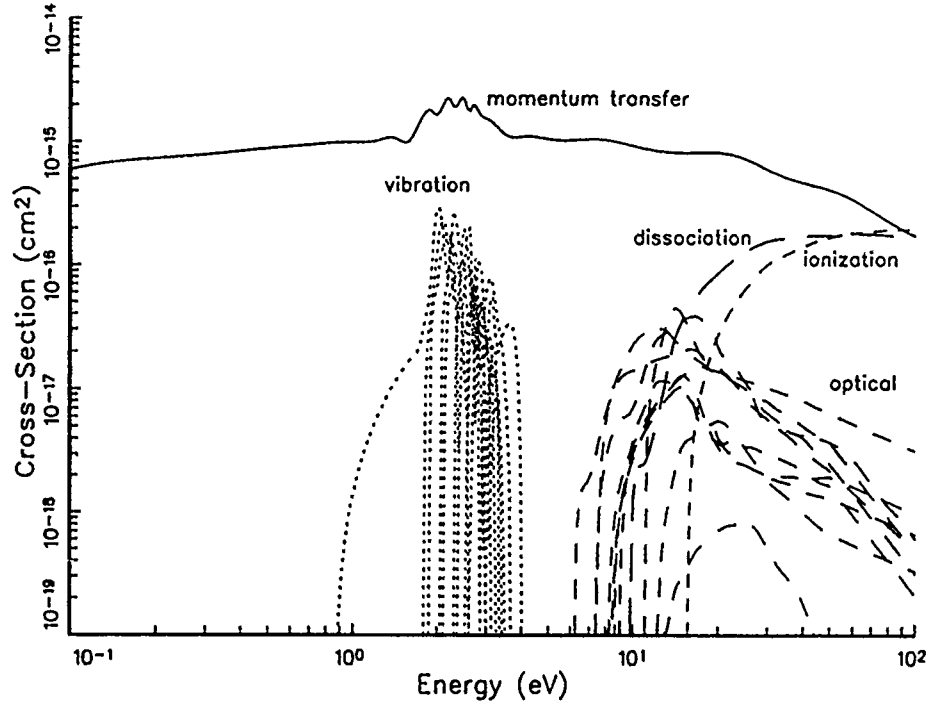
Figure 3.2. Nitrogen Cross-sections

### 3.1.3 Review of Assumptions

At this point, it may be helpful to reiterate the final form of the Boltzmann equation and the assumptions which were made in its derivation. The Boltzmann equation is

$$\frac{\partial f_0}{\partial t} = \frac{1}{2v^2}\frac{\partial}{\partial v}\left\{ v^2\left[ \delta v_m v f_0 + \left( \delta v_m \frac{kT}{m} + \frac{e^2 E_{pk}^2}{3\, m^2}\left(\frac{v_m}{v_m^2 + \omega^2}\right)\right)\frac{\partial f_0}{\partial v}\right] \right\} - S_{0in}. \quad (3.16)$$

Note that the product $E \cdot u$ in equation (3.9) has been replaced by its time-averaged value in the term which describes the effects of the field. This is equivalent to assuming that the field is rapidly alternating, relative to the heating of the electron distribution. In this case, the isotropic portion of the distribution responds only to changes in the average field intensity, because the sinusoidal variation is too rapid for its effects to be transmitted to the

36

distribution by collisions [Gurevich, 1978]. Because many elastic collisions are required to alter an electron's energy appreciably, the use of the averaged field value is possible as long as the collision frequency is of the same order of magnitude or smaller than the wave frequency. For the altitude and frequency regime of most interest to AIM, maximum collision frequency is less than $10^9$ and the heater frequency is at least 300 MHz, corresponding to an $\omega/\nu_m > 1.9$. The inelastic losses are described as follows:

$$S_{0in} = S_{0in}^{rot} + S_{0in}^{vib} + S_{0in}^{opt} + S_{0in}^{dis} + S_{0in}^{att} + S_{0in}^{ion} \qquad (3.11)$$

$$S_{0in}^{rot} = -\frac{1}{2v^2}\frac{\partial}{\partial v}\left[ v^2\left(\sum_k \frac{8B_k N_{nk}\sigma_k}{mv}\right)\left(vf_0 + \frac{kT}{m}\frac{\partial f_0}{\partial v}\right)\right] \qquad (3.12)$$

$$S_{0in}^{vib} = -\frac{2}{mv}\sum_{kj} N_{nk}\left[(\varepsilon + \varepsilon_{kj})f_0(\varepsilon + \varepsilon_{kj})\,\sigma_{kj}^{vib}(\varepsilon + \varepsilon_{kj}^{vib}) - \varepsilon f_0(\varepsilon)\,\sigma_{kj}^{vib}(\varepsilon)\right] \qquad (3.17)$$

$$S_{0in}^{opt} = -\frac{2}{mv}\sum_{kj} N_{nk}\left[(\varepsilon + \varepsilon_{kj})f_0(\varepsilon + \varepsilon_{kj})\,\sigma_{kj}^{op}(\varepsilon + \varepsilon_{kj}^{op}) - \varepsilon f_0(\varepsilon)\,\sigma_{kj}^{op}(\varepsilon)\right] \qquad (3.18)$$

$$S_{0in}^{dis} = -\frac{2}{mv}\sum_{k} N_{nk}\left[(\varepsilon + \varepsilon_{k})f_0(\varepsilon + \varepsilon_{k})\,\sigma_{k}^{dis}(\varepsilon + \varepsilon_{k}^{dis}) - \varepsilon f_0(\varepsilon)\,\sigma_{k}^{dis}(\varepsilon)\right] \qquad (3.19)$$

$$S_{0in}^{att} = -\left(N_{O_2}\,\sigma_{at2}(v) + N_{O_2}^2\,\sigma_{at3}(v)\right)v\,f_0 \qquad (3.14)$$

$$S_{0in}^{ion} = \sum_k \int_{v_{ion}}^{\infty} N_k\,v^3 F_k(v,v')f_0\,\sigma_{ion}(v')\,dv' \qquad (3.15)$$

Equation (3.16) together with the inelastic loss equations above form the set of equations which were solved numerically. The major assumptions required in the derivation of these equations are listed below:

- The quiver energy is below the threshold energy for the dominant loss processes, so rates of energy loss and electron production rates are determined by $f_0$.

- The plasma is locally uniform, and diffusion operates on much longer timescales than ionization, so transport may be neglected.

- The fractional ionization is low, so electron-electron and electron-ion elastic

37

collisions, as well as electron-ion inelastic processes such as detachment and recombination, may be ignored.

- The number of molecules in excited states is low, so superelastic collisions are unimportant.

- The electric field is rapidly alternating, so the time-averaged field may be used.

In addition, in the implementation of the numerical solution, the neutral atmosphere was assumed to consist of molecular oxygen and nitrogen only, excluding other trace neutral constituents.

The numerical solution of these equations will be described in detail in section 3.3. Before proceeding to this, an analytic approximation for the electron production rate will be developed.

## 3.2 Analytic Approximations

In order to develop a simple analytic approximation for the electron production rate, we must develop an expression for the rate at which electrons are energized by the field. To do this, equation (3.9) may be rewritten in terms of energy as

$$\frac{\partial f_0(\varepsilon)}{\partial t} = \frac{1}{\sqrt{\varepsilon}} \frac{\partial}{\partial \varepsilon} \left[ \varepsilon^{3/2} D(\varepsilon, \omega, \tilde{\varepsilon}) \frac{\partial f_0(\varepsilon)}{\partial \varepsilon} \right] - S_0(\varepsilon), \qquad (3.20)$$

where

$$D(\varepsilon, \omega, \tilde{\varepsilon}) = \frac{2}{3} \tilde{\varepsilon} \frac{v_m(\varepsilon)}{1 + v_m^2(\varepsilon)/\omega^2} \qquad (3.21)$$

and $\tilde{\varepsilon}$ is the quiver energy defined by equation (3.1). For $(v_m/\omega)^2 \ll 1$,

$$D(\varepsilon, \omega, \tilde{\varepsilon}) \approx \frac{2}{3} \tilde{\varepsilon} v_m(\varepsilon). \qquad (3.22)$$

Since the rate of increase of the energy of the average electron is

$$\frac{\partial(<\varepsilon>)}{\partial t} = \frac{1}{\sqrt{\varepsilon}}\frac{\partial}{\partial \varepsilon}\left(\varepsilon^{3/2}D(\varepsilon,\omega,\tilde{\varepsilon})\right), \tag{3.23}$$

the rate of energy increase when $(v_m/\omega)^2 \ll 1$ is

$$\frac{\partial(<\varepsilon>)}{\partial t} \approx \tilde{\varepsilon}\, v_m. \tag{3.24}$$

When the quiver energy is less than 2 eV, it is difficult to find valid analytic approximations for $f_0(\varepsilon)$, which would allow the direct solution of (3.20). Therefore, we will employ a test particle analysis to determine the ionization rates. The underlying physics can be understood by first ignoring the inelastic processes except for ionization. If $v_{net}$ is the net electron production rate, the effective ionization time $1/v_{net}$ is the sum of the energization time of a "test" electron from zero energy to an energy $\varepsilon$ above the ionization energy, $\tau_e(\varepsilon)$, and of the time it takes to make an ionizing collision, i.e. $1/v_i$. We thus have

$$\frac{1}{v_{net}} = \tau_e + \frac{1}{v_i}. \tag{3.25}$$

The value of $\tau_e(\varepsilon)$, in the absence of losses, is given by

$$\tau_e(\varepsilon) = \frac{\varepsilon}{v_m\tilde{\varepsilon}}. \tag{3.26}$$

If we fix the value of $\varepsilon$ at 20 eV, equations (3.25) and (3.26) give

$$v_{net} = \frac{v_m}{20}\tilde{\varepsilon}\frac{1}{1 + \frac{\tilde{\varepsilon}}{20}\frac{v_m(20\ eV)}{v_i(20\ eV)}}, \tag{3.27}$$

with $\tilde{\varepsilon}$ in units of eV. From the cross-section data in section 3.1.2.3, we can see that for energies of 20 eV, $v_m/v_i = \sigma_m/\sigma_i \approx 25$, so

$$v_{net} = \frac{v_m\tilde{\varepsilon}}{20} \tag{3.28}$$

for values of $\tilde{\varepsilon} < .5$-1 eV. The physical idea behind equation (3.28) is that for values of $\tilde{\varepsilon}$ < .5-1 eV the energization time is much slower than the time required for an electron with sufficient energy to ionize to make an ionizing collision; therefore, the effective production

rate is $v_{net} \approx 1/\tau_e(\varepsilon)$. Notice that if instead of $\varepsilon \approx 20$ eV we considered $\varepsilon \approx 25\text{-}30$ eV the production rate does not change to any significant degree.

Based on the $v_{net} \approx 1/\tau_e(\varepsilon)$ approximation, we proceed to calculate the energization time of a test electron to 20 eV energies in the presence of inelastic losses. We can approximate the value of the elastic collision rate by

$$v_m(\varepsilon) = v_{max} \frac{\varepsilon + .1}{\varepsilon + 5}, \tag{3.29}$$

were $\varepsilon$ is in units of eV, and the maximum elastic collision rate is given by $v_{max} = 3 \times 10^{-7}$ $N$. The average collision frequency for energies between 0 and $\varepsilon'$ is:

$$\bar{v}_m = v_{max} \frac{1}{\varepsilon'} \int_0^{\varepsilon'} \frac{\varepsilon + .1}{\varepsilon + 5} d\varepsilon = 1 - \frac{4.9 ln(.2\varepsilon' + 1)}{\varepsilon'}. \tag{3.30}$$

For $\varepsilon' = 20$ eV the average value of $v_m$ is $0.61 \, v_{max}$. From equations (3.21-24) and (3.30) we find that in the absence of inelastic losses

$$v_{max} \tau_e \approx \frac{33}{\tilde{\varepsilon}}. \tag{3.31}$$

In the presence of inelastic losses the energization time will increase. To account for the losses we introduce a probability $P(\tilde{\varepsilon})$ that the electron will pass through the excitation band on a single traversal and reach ionization energies. The average energization time would then be

$$v_{max} \bar{\tau}_e = \sum_{n=1}^{\infty} \left\{ v_{max} \, \tau_e \, n \, P(\tilde{\varepsilon}) (1 - P(\tilde{\varepsilon}))^{n-1} \right\} \approx \frac{33}{\tilde{\varepsilon} P(\tilde{\varepsilon})}. \tag{3.32}$$

To calculate the probability $P(\tilde{\varepsilon})$ we must examine the dominant inelastic loss processes. The energy loss function is shown in Figure 3.3. The major barriers to electron energization are the nitrogen vibrational resonances at 2-3 eV, and a larger barrier due to the combined effects of optical resonances and dissociation of both oxygen and nitrogen, between 8 and 20 eV.
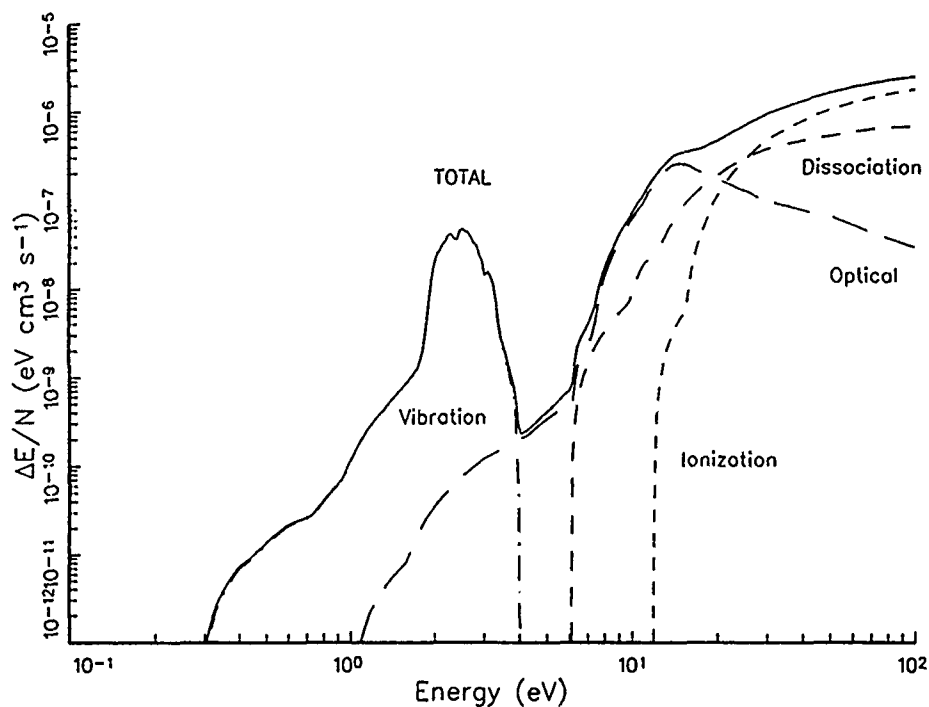
Figure 3.3. Electron Energy Loss Rates in Air

Consider first the nitrogen vibrational barrier. Since the band is relatively narrow we can approximate the vibrational excitation rate $v_{vib}$ by its value at the vibrational peak energy $\varepsilon_{vib}$. In this range the value of the diffusion coefficient in energy space $D_E = <\Delta_\varepsilon^2/\tau>$ is given by

$$D_E(\varepsilon_{vib}) = \varepsilon_{vib}D(\varepsilon_{vib}).$$  (3.33)

As a result, the energy diffusion time through the width $\Delta_{vib}$ of the vibrational barrier is

$$\tau_{D\text{-}vib} = \frac{\Delta_{vib}^2}{D_E(\varepsilon_{vib})}.$$  (3.34)

41

If $\tau_{vib} = 1/v_{vib}$ is the average time to excite vibrational states, then the probability $P_{vib}(\tilde{\varepsilon})$ that an electron will cross the vibrational barrier is given by

$$P_{vib}(\tilde{\varepsilon}) = exp\left[-\left(\frac{\tau_{D\text{-}vib}}{\tau_v}\right)^{1/2}\right]. \tag{3.35}$$

From (3.33-35) we find

$$P_{vib}(\tilde{\varepsilon}) = exp\left[-\left(\frac{3}{2}\frac{v_{vib}(\varepsilon_{vib})}{v_m(\varepsilon_{vib})}\frac{\Delta_{vib}^2}{\tilde{\varepsilon}\,\varepsilon_{vib}}\right)^{1/2}\right]. \tag{3.36}$$

From the cross-section data in section 3.1.2.3. we can see that $v_{vib}(\varepsilon_{vib}) \approx v_m(\varepsilon_{vib})/2$, $\varepsilon_{vib} \approx 2.6$ eV, and $\Delta_{vib} \approx 1.0$ eV. Making these substitutions, we find that

$$P_{vib}(\tilde{\varepsilon}) = exp\left[-\sqrt{\frac{.29\ eV}{\tilde{\varepsilon}}}\right]. \tag{3.37}$$

As can be seen from Figure 3.3, the losses in the 3-8 eV range are much smaller and may be ignored. The remaining barrier is due to both optical excitations and dissociation; it occupies the range between 8-20 eV and reaches a maximum near 14 eV. We can find the probability $P_{opt}(\tilde{\varepsilon})$ of penetrating this barrier by using an approach similar to the one above. In this case $v_{opt}(\varepsilon_{opt}) \approx 0.2\ v_m(\varepsilon_{opt})$, $\varepsilon_{opt} \approx 14$ eV, and $\Delta_{vib} \approx 6$ eV. For these values, we find that

$$P_{opt}(\tilde{\varepsilon}) = exp\left[-\sqrt{\frac{.77\ eV}{\tilde{\varepsilon}}}\right]. \tag{3.38}$$

The total probability that an electron will cross both barriers and reach the energies necessary to ionize is given by

$$P(\tilde{\varepsilon}) = P_{vib}(\tilde{\varepsilon})\,P_{opt}(\tilde{\varepsilon}) \approx exp\left[-\sqrt{\frac{2\ eV}{\tilde{\varepsilon}}}\right]. \tag{3.39}$$

As a result, we find from equation (3.32)

$$v_{max}\overline{\tau_e} = \frac{33}{\tilde{\varepsilon}}\,exp\left[\sqrt{\frac{2\ eV}{\tilde{\varepsilon}}}\right]. \tag{3.40}$$

42

From equations (3.25) and (3.40) we find

$$\frac{v_{net}}{v_{max}} = 3.0 \times 10^{-2} \, \tilde{\varepsilon} \, exp\left(-\sqrt{\frac{2\,eV}{\tilde{\varepsilon}}}\right). \tag{3.41}$$

Substituting the value of $v_{max}$, we arrive at

$$v_{net} = 9.0 \times 10^{-9} \, N \, \tilde{\varepsilon} \, exp\left(-\sqrt{\frac{2\,eV}{\tilde{\varepsilon}}}\right). \tag{3.42}$$

An improvement to the above equation may be made by noting that we used the approximation

$$D(\varepsilon,\omega,\tilde{\varepsilon}) \approx \frac{2}{3} \, \tilde{\varepsilon} \, v_m(\varepsilon) \tag{3.22}$$

instead of the complete form

$$D(\varepsilon,\omega,\tilde{\varepsilon}) = \frac{2}{3} \, \tilde{\varepsilon} \, \frac{v_m(\varepsilon)}{1 + v_m^2(\varepsilon)/\omega^2}. \tag{3.21}$$

For $\omega \gg v_m$ the form of $D(\varepsilon)$ given by equation (3.22) is a good approximation over the entire energy range. However, for $\omega \approx v_m$ over a substantial fraction of the energization process the differences may become important. This leads to an obvious modification of equation (3.42) to

$$v_{net} = 9.0 \times 10^{-9} \, N \, \frac{\tilde{\varepsilon}}{1 + v_m^2(\varepsilon)/\omega^2} \, exp\left(-\sqrt{\frac{2\,eV}{\tilde{\varepsilon}/(1 + v_m^2(\varepsilon)/\omega^2)}}\right). \tag{3.43}$$

The proper value of $v_m(\varepsilon)$ is the value at the barrier energy. Since the most important barrier is the one due to optical and dissociation processes, at this high energy barrier, $v_m(\varepsilon) \approx v_{max}$, and

$$v_{net} = 9.0 \times 10^{-9} \, N \, \frac{\tilde{\varepsilon}}{1 + v_{max}^2/\omega^2} \, exp\left(-\sqrt{\frac{2\,eV}{\tilde{\varepsilon}/(1 + v_{max}^2/\omega^2)}}\right), \tag{3.44}$$

43

where $v_{max} = 3 \times 10^{-7} N$. This approximate formula gives net electron production rates which agree well with the results of kinetic computations (see section 3.3.4), and is used in the one-dimensional simulations of plasma generation described in section 6.1.

## 3.3 Numerical Modeling

We now return to the numerical solution of the full set of equations for the electron energy distribution. Equations (3.11-12 )and (3.14-19) in section 3.1.4 together form a partial differential equation for the distribution $f_0$ in velocity (or energy) and time. This equation was solved numerically using a finite-difference technique with a variable energy grid and an adaptive timestep mechanism.

### 3.3.1 Approach

To solve the equations for the distribution function numerically, it is necessary to transform them into an equivalent set of equations on discrete time and energy (or velocity) grids. One method for performing this transformation is the finite-difference method; it may be developed very simply from the definition of the derivative. Because the equations to be solved are first-order in time, this will yield an equation for the distribution function at a given timestep in terms of the function at the previous timestep.

Modeling of ionization in the atmosphere is accomplished by setting the distribution function to its initial value, a Maxwellian at the ambient electron temperature, and calculating successive distributions by applying the finite-difference equation repeatedly. This will result in a time history of the distribution function, which may be integrated over velocity according to equation (3.6) to give the electron density, and which may also be used to calculate average collision rates for momentum-transfer, attachment, and ionization using the formula

$$v = K \int_0^\infty \sqrt{\varepsilon} f_0(\varepsilon)\, \sigma(\varepsilon)\, d\varepsilon, \qquad (3.45)$$

where $v$ is the desired rate, $K$ is a normalization constant, and $\sigma$ is the cross-section for the process in question.

The set of equations (3.11-12) and (3.14-19) may be approximated by the finite-difference equation

$$\frac{f_0^{t+\Delta t} - f_0^t}{\Delta t} = (T + U)\, f_0^{t+\Delta t}. \tag{3.46}$$

Here the continuous function $f_0$ has been replaced by the vector $f_0$, a one-dimensional array which approximates the value of $f_0$ at discrete energies; the time derivative has been replaced by its difference approximation; and the effects of the electric field and of collisions have been combined into the matrices $T$ and $U$. The matrix $T$ is a tridiagonal matrix representing the effects of the electric field, elastic collisions, and rotational inelastic collisions, all of which appear in the original equations as terms containing the first and second derivatives of $f_0$ with respect to $\varepsilon$. The other inelastic processes cause discontinuous changes in electron energies and cannot be represented in this way; their effects are combined in the upper triangular matrix $U$. This is a fully implicit equation because the operators representing the energy derivatives are applied to the value of $f_0$ at the succeeding timestep; it is unconditionally stable and convergent to the solution of the corresponding differential equation.

The solution of this equation for values of $f_0$ at the succeeding timestep $t+\Delta t$ is simplified because of the form of the matrices $T$ and $U$. Instead of the full matrix inversion implied by the equation

$$f_0^{t+\Delta t} = \left(I - \Delta t\,(T + U)\right)^{-1} f_0^t, \tag{3.47}$$

where $I$ is the identity matrix, a much faster solution may be obtained by starting with

$$\left(I - \Delta t\,(T + U)\right) f_0^{t+\Delta t} = f_0^t . \tag{3.48}$$

The matrix multiplying $f_0^{t+\Delta t}$ is an upper Hessenburg matrix, with only one element immediately below the diagonal in each column. If these are removed by row elimination, then the resulting upper triangular matrix equation may be solved by backsubstitution. This is much faster than solution techniques using more general methods of matrix inversion.

The number of elements in $f_0$ will determine the accuracy of the solution and the computational effort required. It is necessary for the values to be closely spaced in the

45

region where the cross-sections are highly detailed. The nitrogen vibrational resonances in the region below 4 eV are very sharp; these require energy values spaced no more than 0.1-0.2 eV apart for the cross-sections to be accurately modeled. At higher energies, there is less need for closely spaced samples because the cross-sections are much smoother. A variable energy grid was used to allow accurate modeling of the energy regions where fine details existed without the inefficiency which would result from fixed spacing. The energy levels were placed at constant intervals between 0.01 and 4 eV, and at constant ratios between 4 and 100 eV. The lower limit, upper limit and breakpoint were all selected on the basis of tests of the numerical simulation in a wide variety of situations; they represent the best compromise between numerical accuracy and computational speed.

A valuable check on the accuracy of the numerical simulation is to compute the energy balance. Because the cross-section for each process is available and the energy loss due to each event is known, the energy absorbed by each process may be computed on each timestep. The energy lost by the electric field may also be computed and compared to the sum of the energies absorbed. Agreement between the two totals was excellent, typically with errors less than .01%.

### 3.3.2   Results

The equations described above were numerically solved over a wide range of altitudes and frequencies. Figures 3.4 to 3.6 below show the time evolution of $f_0$ at intervals of 200 ns for power densities of 300 W/m$^2$, 3 kW/m$^2$, and 30 kW/m$^2$, respectively. In all three cases, the altitude was 70 kilometers and the frequency was 300 Megahertz.
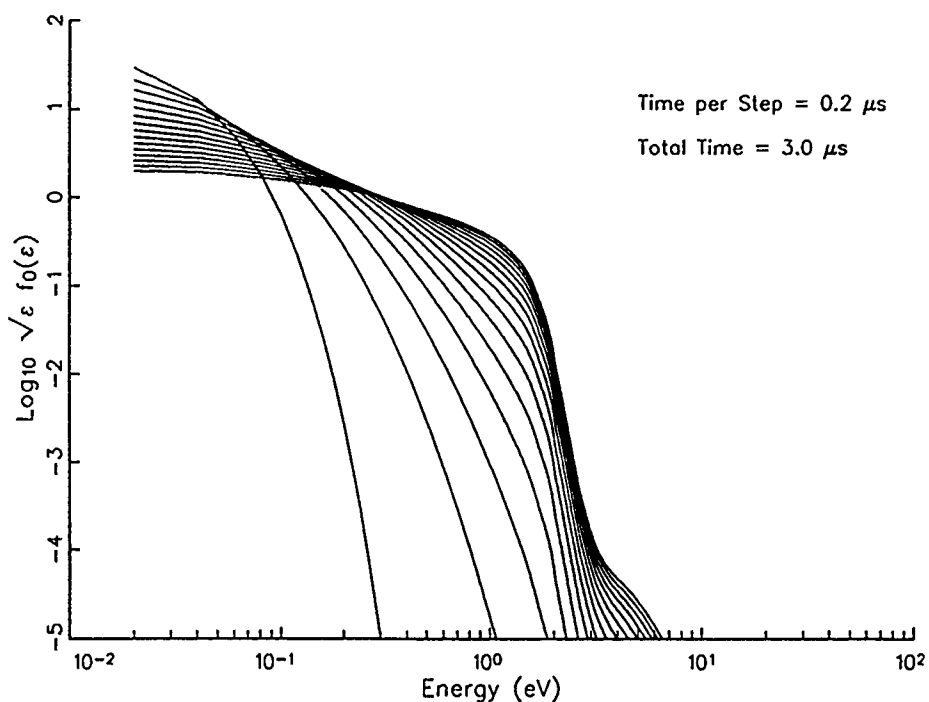
Figure 3.4. Evolution of $f_0$ for Power Density of 300 W/m$^2$

The low-power case corresponds to a quiver energy of 0.0056 eV. Note the abrupt drop in the distribution when the vibrational barrier at 2-4 eV is encountered, and the further drop in the 6-8 eV range due to optical excitations and dissociation. Virtually no electrons reach energies sufficient to ionize. Note also the relatively long time (> 2 μs) required for a stable shape to be reached.

Figure 3.5. Evolution of $f_0$ for Power Density of 3 kW/m$^2$

Figure 3.5 shows the density evolution for a quiver energy of 0.056 eV. Here the drop due to the vibrational barrier is not as pronounced, and some electrons reach the energies required to ionize. The steady-state shape of the distribution function is reached in .8-1 μs.
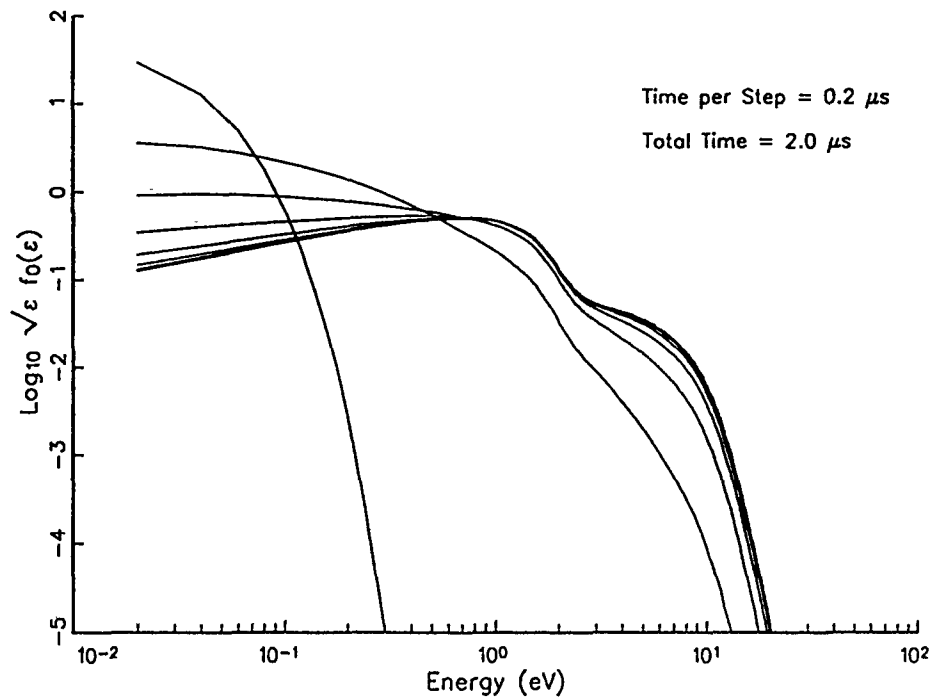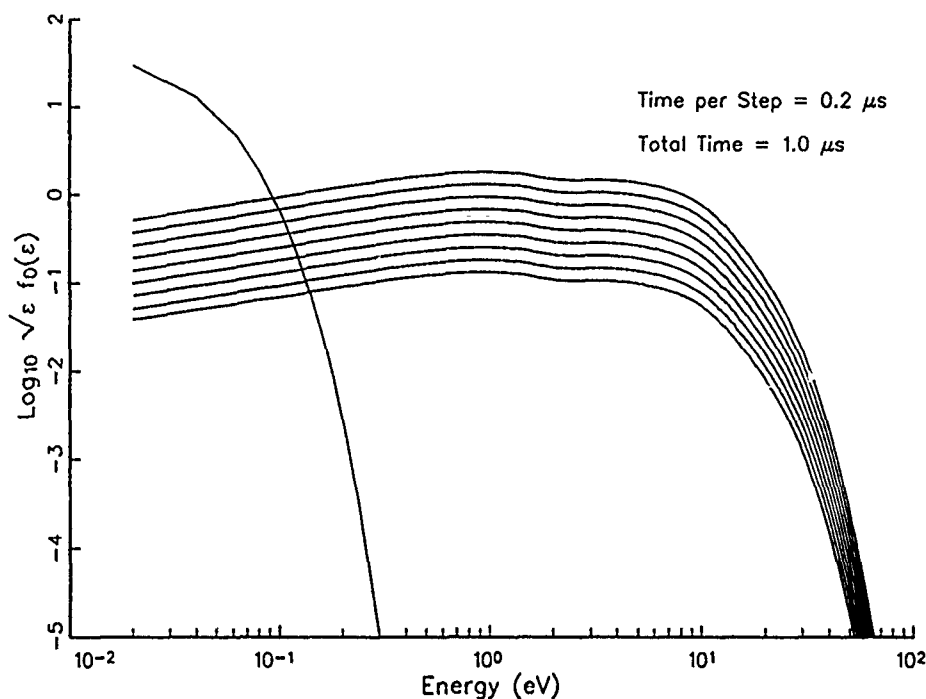
Figure 3.6. Evolution of $f_0$ for Power Density of 30 kW/m$^2$

At a power density of 30 kW/m$^2$, corresponding to a quiver energy of 0.56 eV, large numbers of electrons reach energies of 20 eV or more. The vibrational loss barrier has very little effect, and the distribution reaches a stable shape within 200 ns. The upward motion of the distribution indicates that substantial electron production is taking place.

The data of primary interest are the net electron production rates $v_{net}$. These are shown in Figure 3.7 for frequencies from 150-600 MHz and power levels from 1 kW/m$^2$ to 1 MW/m$^2$, at an altitude of 70 kilometers. While Figure 3.7 seems to suggest that lower heater frequencies are favored, for their corresponding lower power density requirements, it should be remembered that for a constant power-aperture product, the power density scales as $\omega^2$, which compensates for the higher power density requirements.
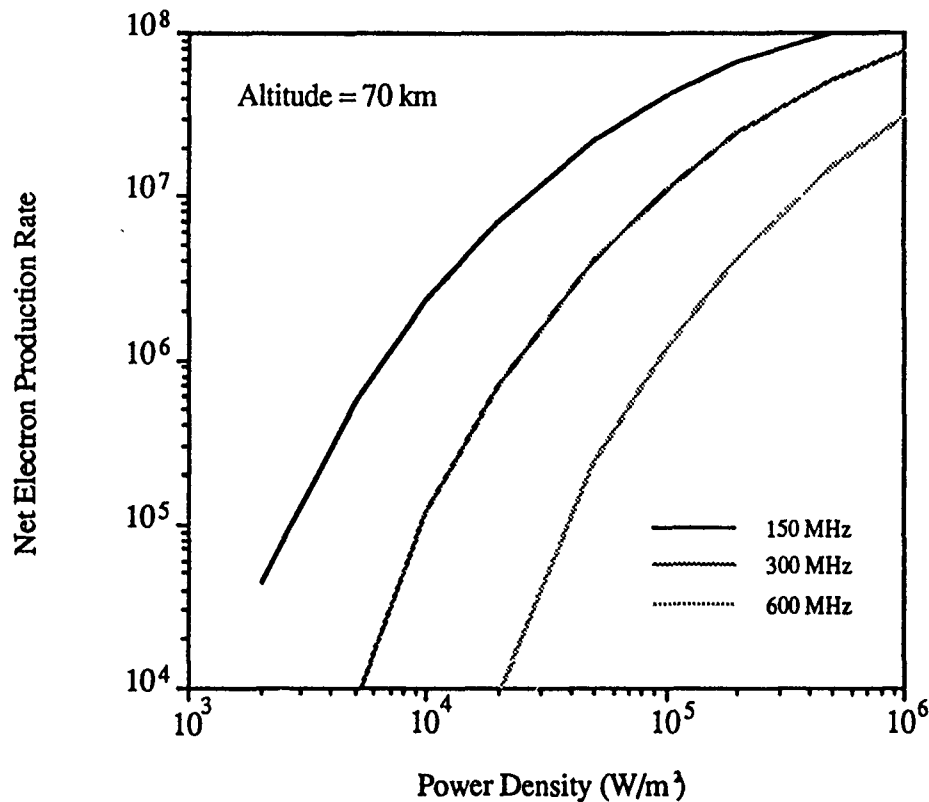
Figure 3.7. Net Electron Production Rates

### 3.3.3  Comparison with Experimental Data

As discussed in section 2 above, the derivation of net ionization rates from most breakdown experiments involves making several assumptions about the initial and final electron densities. These assumptions introduce uncertainty into the experimentally derived rates which make comparisons with the rates predicted by kinetic calculations difficult. One of the few experiments which directly measured ionization rates was performed by Hays, et. al. [Hays, et. al., 1987]. In this experiment, the net electron production rate was measured for microwave ionization of pure $N_2$. A magnetic field was imposed on the test cell, and the microwave frequency was adjusted to the electron gyrofrequency, in order to perform gyroresonance heating. Under these conditions, the electric field of the microwave radiation can be equated with an effective DC electric field, and the results may be used to predict ionization rates for DC fields. (A more complete discussion of this is given in the cited paper.)

To compare the results of this experiment with the kinetic calculations described above, a series of kinetic computations was made for pure $N_2$ at a number density of $1 \times 10^{15}$ cm$^{-3}$

50

(0.03 Torr). The computations were performed for a DC field at various intensities. The substitution of the time-averaged field for the product $E \cdot u$ which was made in equation (3.16) was removed, and the proper DC electric field was inserted. This removed the frequency constraint which would otherwise have prevented the use of the simulation to model DC breakdown. A comparison between the calculations and experimental data is shown in Figure 3.8 below.
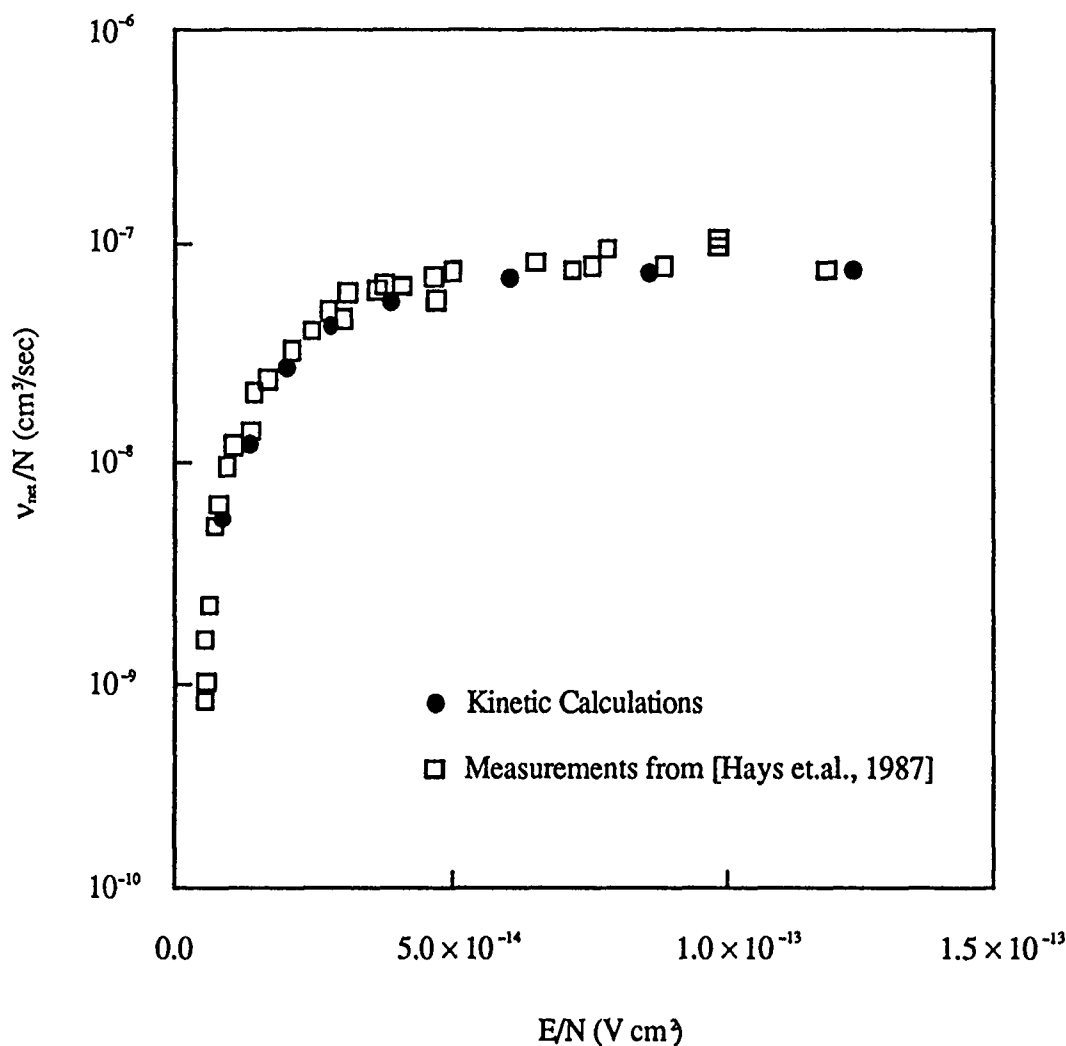


Figure 3.8. Comparison With Experiment for Pure $N_2$.

The agreement between predicted and measured electron production rates is excellent. Although the DC breakdown is not the region of primary interest, the results provide some degree of confidence in the correctness of the implementation and the quality of the cross-section data for nitrogen.

Comparisons with conventional breakdown data for air are complicated by the difficulties of accurately measuring ionization rates, as discussed in section 2. A comparison between kinetic calculations for typical AIM heater frequencies (200-600 MHz) and experimental data are shown in Figure 3.9. The data are shown in $E_e/P$ format. (A full discussion of the sources of the experimental data shown is given in section 2.1.)
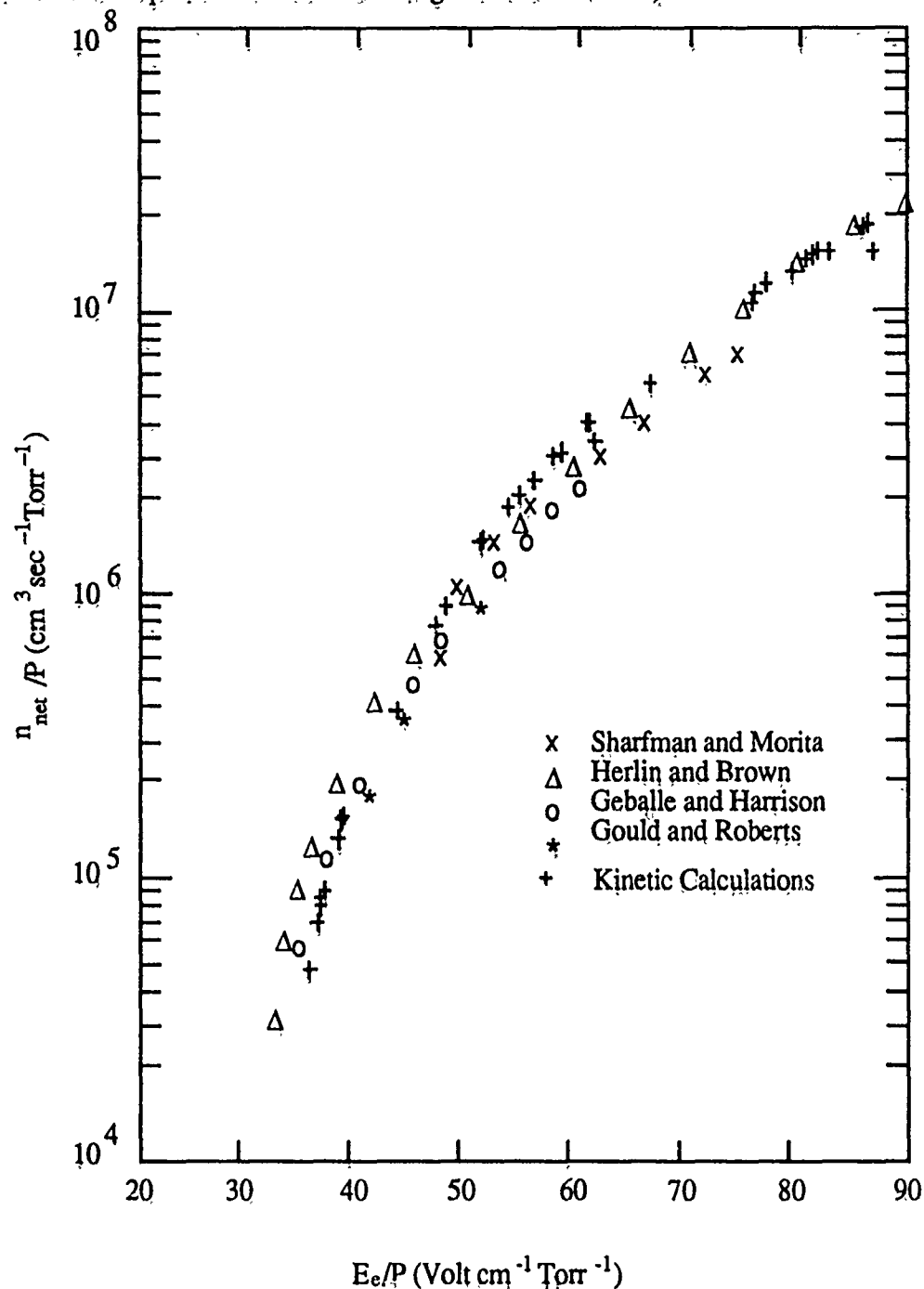


Figure 3.9. Comparison of Kinetic Calculations with Experiments

The kinetic computations show good agreement with experimental data over the region for which data are available, and provide a source of electron production rates over a much wider range of frequencies and power levels. It has been used for zero-dimensional analysis and as a check on the analytic approximation developed in section 3.2.

### 3.3.4 Comparison with Analytic Approximation

The results of a comparison between the analytic approximation given by equation (3.44) and kinetic calculations for a typical altitude and frequency are shown in Figure 3.10. The agreement between the two methods is quite good. The use of the analytic approximation in one-dimensional simulations of plasma formation is discussed in detail in section 6.1.
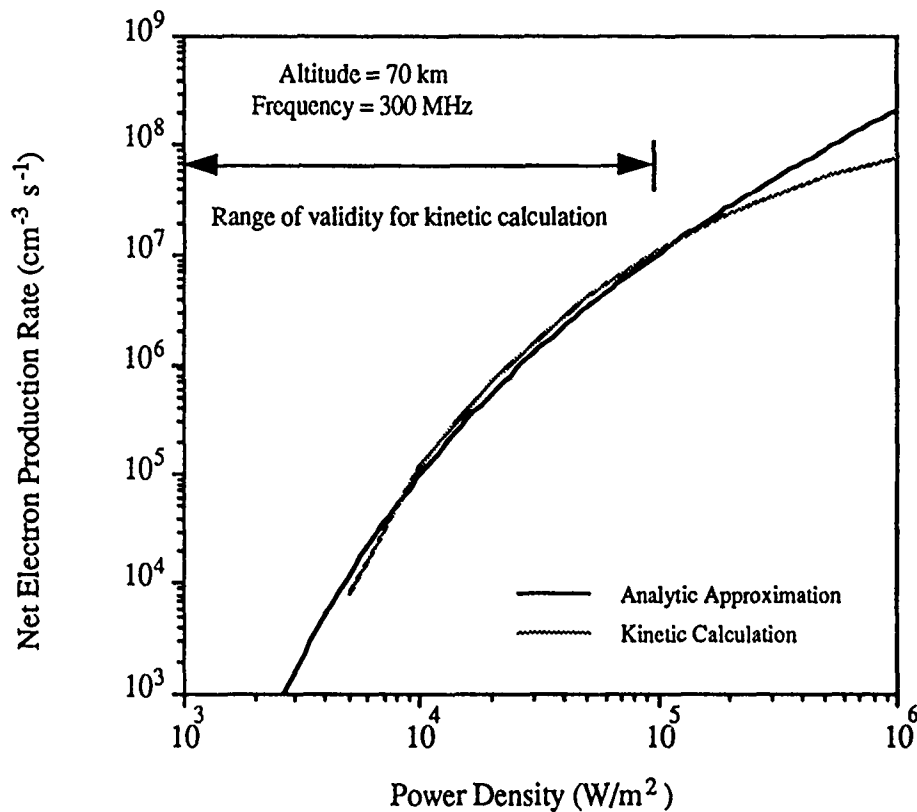


Figure 3.10. Comparison of Kinetic Calculations and the Analytic Approximation

The analytic approximation shows good agreement with both kinetic computations and experimental data. Because it is much less difficult to apply the approximation than to

perform a kinetic computation, the approximation has been used in the one-dimensional simulation of the plasma formation process.

## 3.4 Conclusion

A theoretical examination of the breakdown process has been performed, culminating in the development and application of two complimentary methods for calculating electron production rates. The first, a kinetic computation based on the Boltzmann equation, has been used to develop an understanding of the conditions necessary for efficient ionization, and to calculate electron production rates for a wide variety of situations. A simpler analytic approximation has also been developed for use in multidimensional simulations where the kinetic calculation is too computationally intensive.

## 4.0 FORMATION, MAINTENANCE, AND CONTROL OF AIM

Formation and control of the AIM cloud presents both a physics as well as a technological challenge. To minimize the cost and technical risk challenge, it is necessary to explore a parameter space of extremely broad range related to the spatial and temporal behavior of the RF power projected in the ionosphere. The physical parameters, which determine AIM formation and are under our control, are the heater frequency, $\omega$, the location of the focal point, the power density and the power density gradient in the vicinity of the focal point (i.e. the focal length) and the temporal profile of the power density. These are, of course, coupled to the design of the RF antenna and its associated power system.

A key factor controlling the profile and maximum density of the AIM cloud is self absorption. At the onset of ionization the externally imposed power density profile is strongly modified by the presence of the newly created plasma, which for the regime of interest has an RF power absorption length comparable to the imposed power density gradient (100 - 1000 m typical). The controlling role of the nonlinear self absorption distinguishes the AIM breakdown physics from the conventional breakdown regime that has been explored in chamber experiments. In the latter case, the focal length was at all times shorter than the absorption length. As a result, the plasma frequency attained was comparable to the ionizing RF (i.e. $\omega_p \approx \omega$). It should be noted that the ionized clouds produced by chamber experiments have strong spatial irregularities due to the final stage of ionization being performed under critical density conditions, resulting in strong nonlinear focusing of the RF.

In the early stages of this research effort, it was realized that self absorption effects limit the maximum density achievable in atmospheric breakdown. This requires creating the AIM cloud under strongly underdense conditions (i.e. $\omega_p < .1\omega$) resulting in an absence of nonlinear focusing and its attendant irregularity structure. At the same time, self absorption leads to an extremely inefficient ionization process, where the energy required for the formation of an electron-ion pair can be several orders higher than the optimum 30-40 eV/pair measured in laboratory chamber experiments. Thus, overcoming the inefficiency of the breakdown process under AIM conditions constitutes a critical task. A variety of approaches using frequency chirping, focal point steering and short RF pulse "sneak-through" has been suggested, and will be considered during the next phase of the program. It is important to note that, because of the high number of neutrals relative to electrons ($10^{15}$ vs. $10^7$), AIM formation and evolution is not subject to the dynamic motions and

plasma instabilities normally encountered in plasma physics. Cost and efficiency considerations place a high premium on the construction of reliable multidimensional dynamic models of the AIM cloud formation which can be used to reduce the uncertainties associated with an AIM heater design. We discuss below the critical uncertainties that can be resolved by using experimental, computational, and analytic techniques.

Our literature review identified two potential weaknesses associated with the conventional thinking on AIM breakdown:

1. Laboratory experimentation has focused on breakdown where the losses were non-local. The losses were dominated by transport, either free or ambipolar to the walls. Added complications in transferring laboratory breakdown experiences to AIM include:

    a. Standing wave patterns produced by crossed beams or reflection from plates are used to achieve critical fields.

    b. Most experimentation has been performed using continuous wave (CW) or long pulse width sources.

    c. Although deviations from Maxwellian electron distributions have sometimes been considered in the interpretation of the data, none of the investigations considered situations related to runaway ionization.

2. Theoretical and numerical work on D region breakdown, conducted predominantly in the USSR by Gurevich and his colleagues, emphasized the long pulse regime by considering steady state ionizing electron distribution functions that were balanced by long time (i.e. $t > 10$ $\mu sec$) losses. These distribution functions were also used in studying short pulses with field strengths much above those required for breakdown [Gurevich, 1978]. For such regimes the theory based on distributions balanced by long time scale losses was clearly inapplicable.

The above, as well as the fact that our analysis identified the presence of a high-energy tail in the electron distribution as the determining factor of the heater ERP required for achieving the AIM density profile, indicated that early emphasis should be placed on the kinetics of the energy transfer. A newly developed computer model, based on the Boltzmann equation, and including appropriate kinetic elastic and inelastic losses, is

operational. It has been used along with some theoretically obtained formulas to create a computationally efficient one-dimensional plasma formation code, which simulates the propagation of a pulse of microwave energy in the ionosphere and the resulting changes in electron density.

In this section we describe the work that has been done with this plasma formation code, and conclusions about the AIM system that were reached with its use. Next, a detailed description of the AIM heater analysis performed by APTI is presented along with a description of the current AIM baseline heater design. Finally, a two-dimensional version of the plasma formation code is presented, along with the reasons for its creation and the results it has produced.

## 4.1  One-Dimensional Plasma Formation Model

The simulation known as FAIM (Formation of an Artificial Ionospheric Mirror) has been an integral and essential tool for analysis of the breakdown process. The code simulates the microwave breakdown of air through avalanche ionization by propagating a pulse of microwave energy upwards and using several alternative formulas for net electron production rate to calculate changes in the electron density. For a detailed description of the numerical techniques and formulas in the FAIM code, the reader is referred to section 6.1. In this section we explore the analysis that was performed with the FAIM code, the conclusions reached and their impact on the overall performance of the AIM system.

### 4.1.1  Far Field Breakdown

In this section, atmospheric breakdown by an unfocused heater is analyzed. When the prospective location of the cloud is in the far field of the heater beam, the power density profile from the heater falls off as $1/r^2$ with altitude. This obviously favors ionization at lower altitudes where the power density is higher. However, the neutral density (or pressure) decreases exponentially with altitude. Collision frequency grows proportionately with neutral density. This favors ionization at higher altitudes. In practice, these opposing conditions permit ionization to occur over an altitude regime, where the loss in power density by $1/r^2$ is not too much and where the neutral density is still sufficiently high. Figure 4.1 shows the profile of net ionization frequency from an unfocused heater beam operating at 300 MHz. The reader will note the decrease in power density beginning at 38

57

km altitude and continuing as $1/r^2$. The point of maximum net ionization frequency is 46 km. This phenomenon is due to the energy transfer rate to electrons, described by the term $D(\varepsilon, \omega, \tilde{\varepsilon})$ in equation (3.21). The equation shows that coupling of energy to electrons is determined by

$$\frac{S}{\omega^2} \frac{v_m}{1 + v_m^2 / \omega^2} ,\qquad (4.1)$$

where $S$ and $\omega$ are the power density and radian frequency of the field, and $v_m$ is the electron-neutral collision frequency.

Figure 4.1 shows the dependence of $v_m / (1 + v_m^2 / \omega^2)$ as a function of altitude for a 300 MHz heater frequency. The formula is multiplied by a constant so that it can be viewed on the same graph as ionization frequency. Although the net ionization frequency depends upon (4.1) in a nonlinear way, it is a monotonic, increasing function; therefore, the maximum ionization rate occurs at the maximum of (4.1). The corresponding plasma frequency profile will also have its maximum at 46 km, as seen in Figure 4.2. The significance of this phenomenon is that the vertical position of the cloud is not adequately controlled by the heater. While it is true that the altitude of this breakdown could be changed by using a varying frequency, this approach has several problems: the resulting electron density profiles have a shallow gradient, resulting in too much absorption of the RF signal to be reflected; the breakdown altitude is so low that AIM lifetime is too short and RF signal absorption is again too high; finally, the fine control of breakdown location required to make a tilted AIM cloud is questionable with this approach. The use of an AIM cloud as a coherent reflector for an RF signal necessitates that the system have control over the position, gradient and inclination of the plasma cloud; an unfocused heater beam will not meet these requirements.
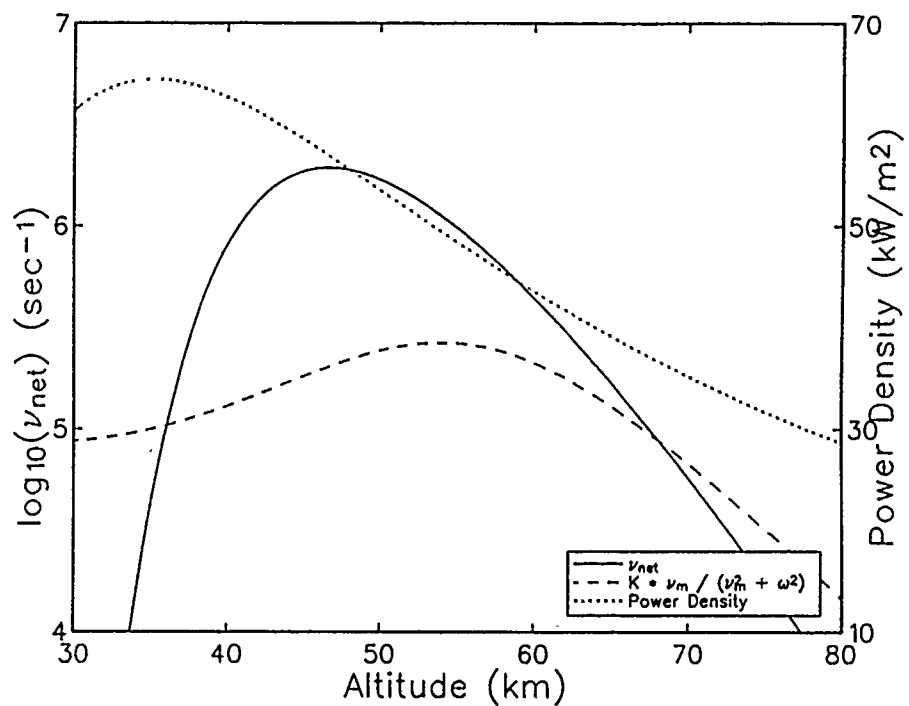
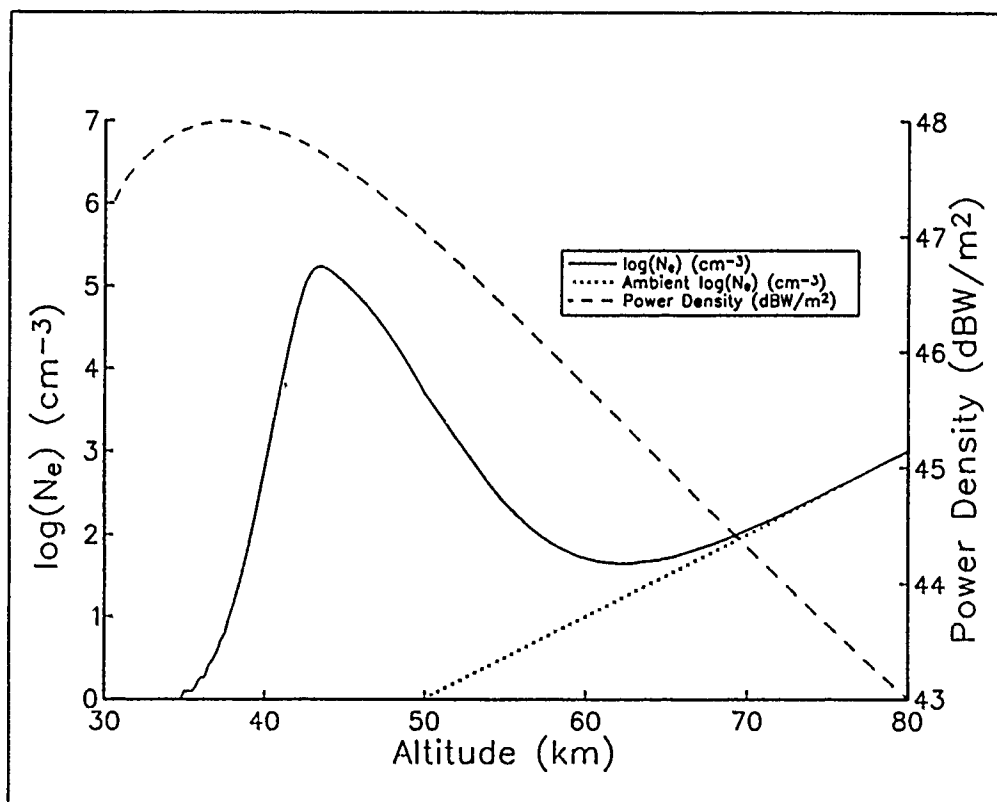Figure 4.1. Ionization Frequency for an Unfocused Beam $(\omega = 6\pi \times 10^8)$



Figure 4.2. Plasma Frequency Profile of an Unfocused Beam

## 4.1.2  Near Field Breakdown

The need to control the altitude of the AIM cloud requires the use of a different approach with the heater antenna.  If the elements of the heater are spread out over a wider area, the desired location of the AIM cloud is in the near field of the heater, where focusing through phase correction of individual elements is possible.  The result is a vertically increasing electric field from the heater antenna at a controlled altitude.  The reader is referred to section 4.2 for a detailed description of near field focusing.  Figure 4.3 shows the same curves as Figure 4.1 for a focused beam.  In this case the effect of the collision frequency term discussed above is overshadowed by the power density profile, which peaks sharply at the desired altitude.  Figure 4.4 shows the resulting electron density profile made by a focused beam.  The advantages of this approach address the disadvantages of the unfocused beam approach.  This method allows breakdown to occur at higher altitudes, thereby increasing AIM lifetime and decreasing absorption effects.  The resulting electron density profiles have a very sharp gradient, which further reduces absorption effects, and fine control over the position of the breakdown is possible.
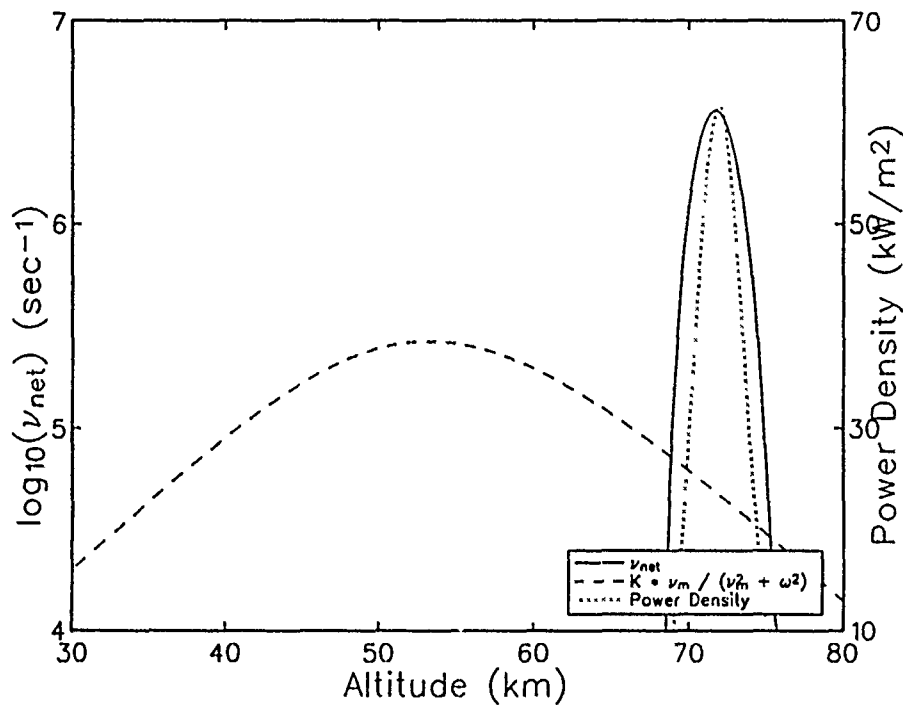


Figure 4.3. Net Ionization Frequency for a Focused Beam  $(\omega = 6\pi\times10^8)$

60
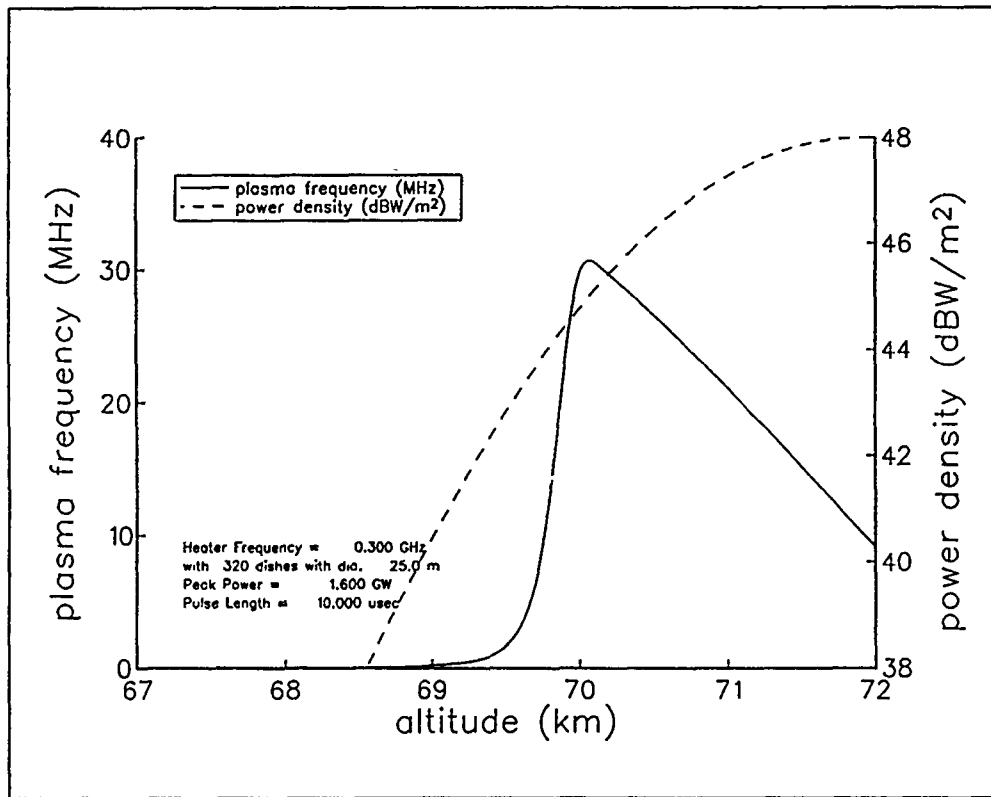
Figure 4.4. Heater Focusing at 72 km Altitude

### 4.1.3 The Clamping Phenomenon

In this section we describe a long pulse effect that increases the gradient of the plasma cloud, thereby reducing the absorption of the radar signal as it bounces off the patch. We first define the critical power density, $S_c$, as the value at which ionization can first occur at a particular altitude. As a long pulse (> 5 $\mu$sec) of microwave energy propagates upwards in the atmosphere and ionization takes place, self-absorption of the pulse decreases the field strength in the pulse. Moreover, the areas with the highest induced electron density will absorb more of the pulse. Eventually, the area of peak ionization will absorb so much of the pulse that the remaining power density will fall below $S_c$. At this point, further ionization can only occur below and in front of the point of peak electron density. This moves the electron density peak down vertically with time, bringing it closer to the point where the unattenuated power density is $S_c$. Figure 4.5 shows the formation of a one-dimensional profile made by a 10 $\mu$sec pulse, at 1.5 $\mu$sec time samples.

Power Density (dBW/m²)

38   40   42   44   46   48

Altitude (km)

72

71

70

69

68

67

Initial Power

Final Plasma Profile

— — — Power Density
———— Plasma Frequency

0   10   20   30   40

Plasma Frequency (MHz)   Samples are 1.5 μsec apart
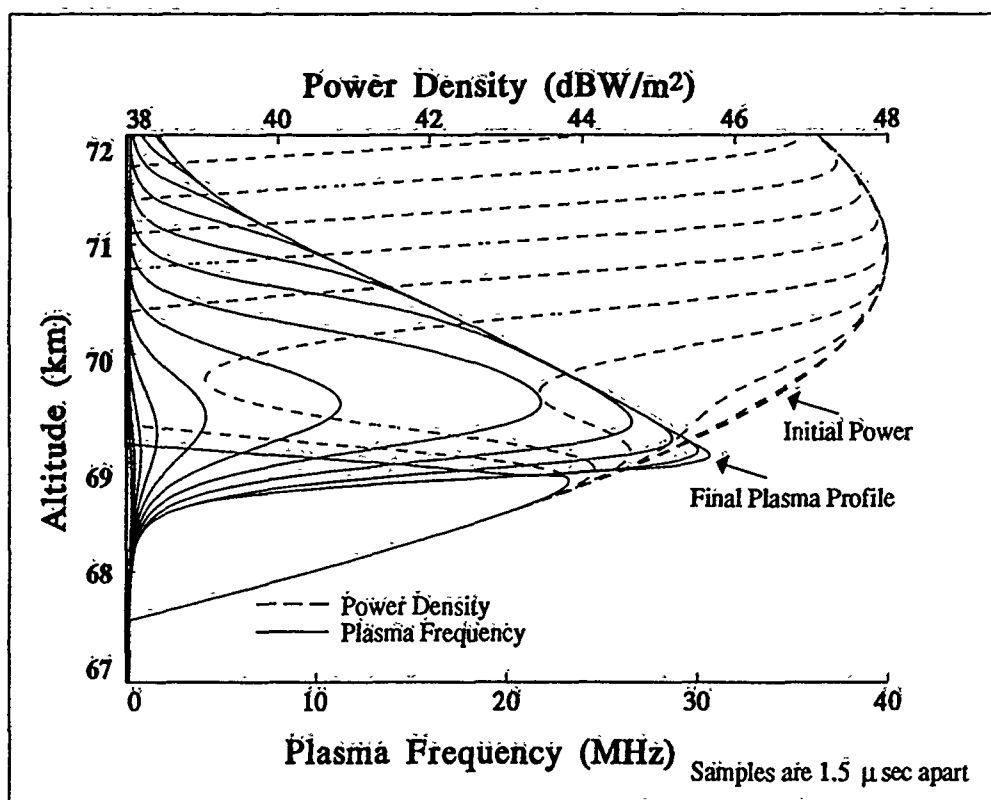
Figure 4.5. Growth Through Time of AIM Cloud with $f$ =300 MHz, $\tau$ = 10 μsec

In addition to the plasma formation, Figure 4.5 also illustrates the reduction in heater power density as the newly created electrons absorb the field. Upon examination of the graph, we note that $S_c$ for this situation is approximately 42 dBW/m². Moreover, when the power density has attenuated below 42 dBW/m² at $h$ = 70.5 km, there is no further ionization at that altitude.

The gradient of the electron density profile is dependent on the slope of the heater antenna's array factor near the initial breakdown point and the heater frequency. A steeper slope in power density creates a corresponding sharper electron density gradient along with a higher peak in electron density profile. Parameter studies show a linear dependence between power density slope and resulting electron density slope. Since self-absorption or attenuation goes down as the heater frequency is increased, a higher frequency will achieve a greater electron density before the clamping phenomenon occurs, and subsequently a steeper slope as well.

## 4.1.4 One-Dimensional Breakdown Simulation Results

The goals of the one-dimensional FAIM simulation encompassed many of the goals of the overall AIM effort. The simulation was designed as a tool for the analyst to develop a better understanding of the atmospheric breakdown process. Its purpose included forming a functional range for many of the heater parameters involved: frequency, pulse length, power requirement, breakdown altitude, heater aperture, etc. Furthermore, FAIM was designed to be a tool for performing tradeoff studies between these parameters and for evaluating candidate heater systems in their ability to form a useful AIM cloud.

As a simulation that modeled the propagation of the heater pulse, FAIM showed that the absorption of the heater beam by existing electrons could aid in the generation of a useful plasma cloud. The clamping phenomenon present in long pulse scenarios enables the system to create a steep electron density gradient without decreasing the heater's beamwidth. The simulation also showed that the peak electron density attainable is related to the heater frequency. Basically, the absorption effects are greater with a lower heater frequency, which in turn means that clamping will occur sooner and the peak electron density will not be as high as with a higher frequency. However, the use of higher frequencies is precluded by available energy sources at those frequencies.

In this section we briefly present some of the results obtained with the FAIM one-dimensional plasma formation simulation. The following profiles show the resulting electron density profiles using alternative AIM heater configurations. The examples are presented to demonstrate the uses of the FAIM code and to illustrate some of the phenomena that the FAIM code helped uncover.
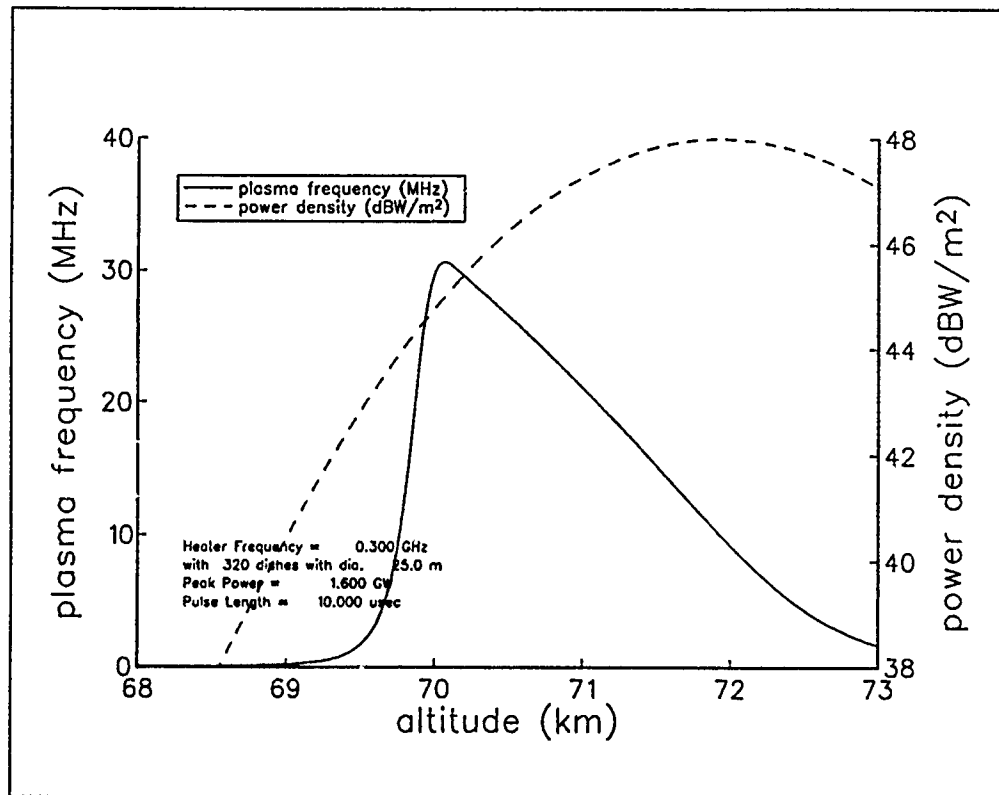
Figure 4.6. AIM Baseline Heater Test Case

Figure 4.6 shows the plasma frequency profile of the AIM baseline system described in section 4.2.4. The reader will note that the heater described in this section has 400,000 elements, each with a 1 meter square aperture. In the simulation, these elements are grouped together in groups of 625 (a 25 × 25 block) called sub-arrays. Grouping the elements into large subarrays allows the simulation to be performed at a substantial saving of computer time with no observable difference in the ionization results. This particular heater system takes full advantage of the clamping phenomenon discussed in section 4.1.3. In this example, the heater beamwidth at the breakdown altitude is 35 meters.
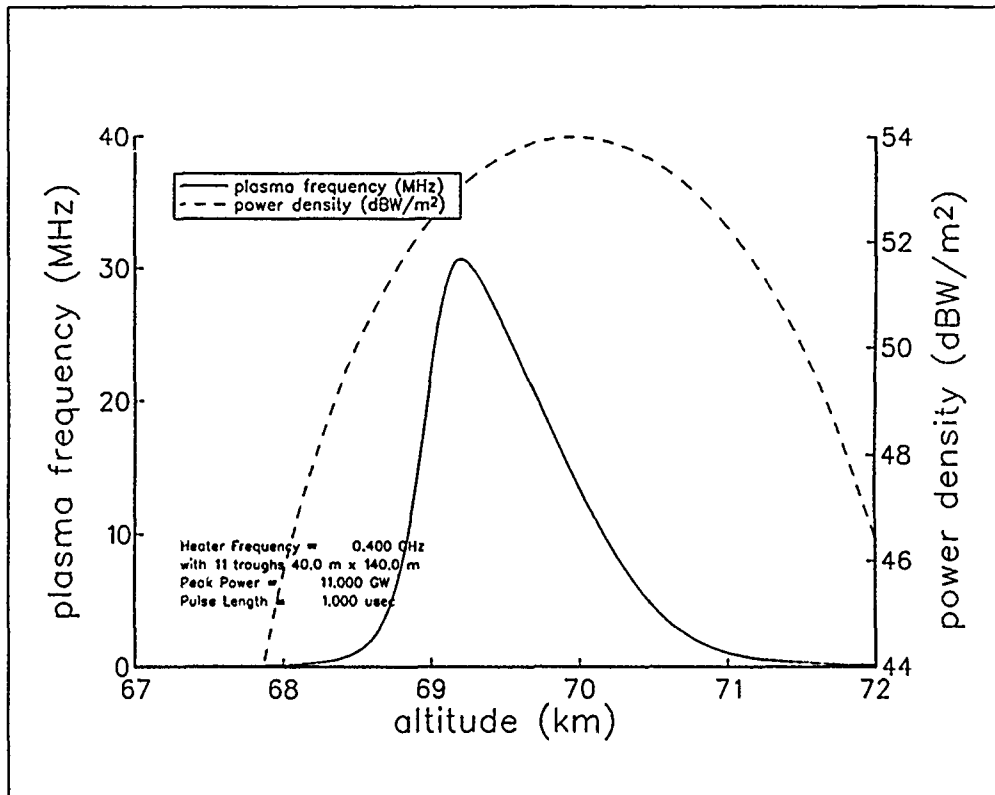
Figure 4.7. UHF Large Trough Array Test Case

Figure 4.7 shows a system using large UHF trough antennas with high power and short pulse. Here the effects of attenuation are much less pronounced since the pulse length is only 1 μsec. The steep electron density gradient in this profile is achieved by using a steeper power density profile than in the previous example. The reader will note that this tradeoff is done at the expense of the heater's beamwidth. In this case, the heater's beamwidth is approximately 20 meters. The surface area of the patch ionized by the system in the previous example with one pulse is therefore 3 times as large as the patch in this example.
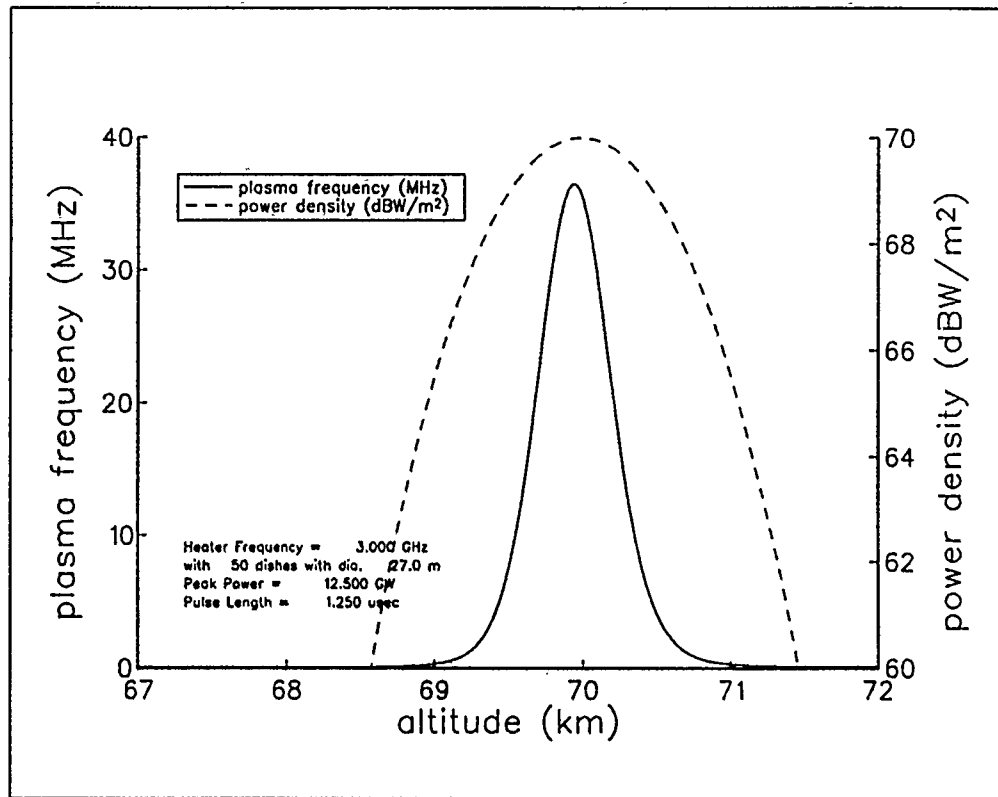
Figure 4.8. S-Rand Large Array Test Case

Figure 4.8 uses an array of large S-band dishes, high power and a short pulse. The effects of attenuation are even less pronounced in this case, since the complex dielectric constant (absorption rate) is proportional to $1/f^2$. The reader will note that the peak electron density achievable is also higher for the same reason. Taken together, these last three examples show the wide functional range of heater frequency, with candidate systems possible from 300 MHz to 3 GHz. In this particular example, the energy source (probably a high power klystron) is not available yet at 3 GHz, and would have to be designed and built.
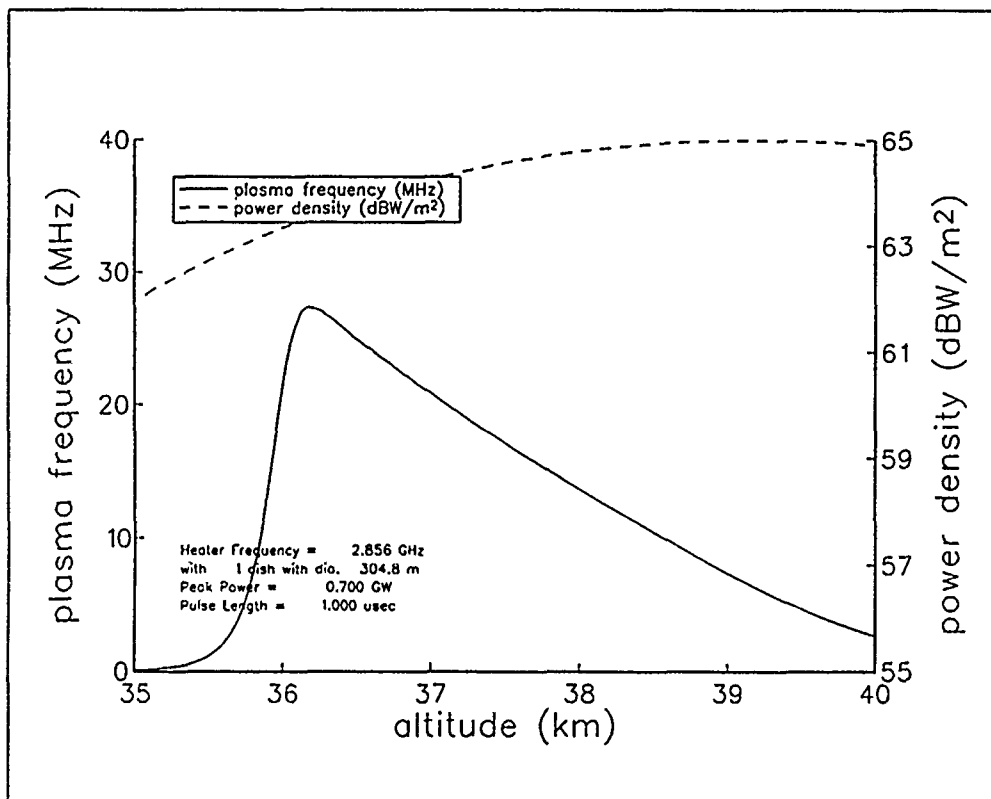
Figure 4.9. Arecibo Test Case

Figure 4.9 uses a model of the Arecibo facility in Puerto Rico. This particular model assumes the use of a feed that would permit efficient focusing with Arecibo's circular dish. In this case the antenna is focused at a much lower altitude since Arecibo's aperture is too small to focus at 70 km with an S-band frequency. The power requirements also preclude Arecibo from working at a higher altitude. This facility should be considered only for a limited concept demonstration because the lifetime of an AIM cloud at 30 - 40 km altitude is much shorter than at 60-70 km altitude, and is of the order of 1 millisec.

## 4.2   Heater Analysis

As discussed in the previous section, controlled formation of an ionized cloud requires a focused beam with ionization occurring in front of the focal point. A very sharp rise in the electric field at the ionization altitude is needed to create high peak density and steep density gradients.
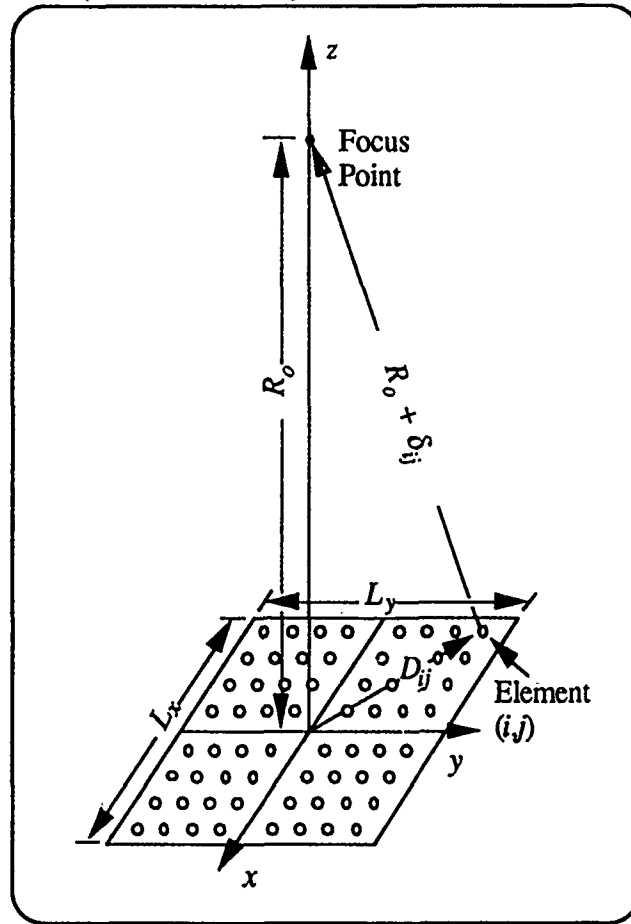
Figure 4.10. Spatial Relationships in a Focused Array

Figure 4.10 shows the spatial relationship for a focused heater array. To have the electric fields from all of the array elements arrive in phase at a distance $R_o$ in the near field of the array, it is necessary to correct the phase of each element to compensate for the phase delay relative to the center element due to the additional phase path $\delta_{ij}$. If $R_o$ is much larger than the maximum $D_{ij}$ in Figure 4.10 then the phase delay can be approximated in wavelengths to be

$$\delta\phi_{ij} = \frac{\delta_{ij}}{\lambda} = \frac{D_{ij}^2}{2 R_0 \lambda} \qquad (4.2)$$

where $\lambda$ is the wavelength of the heater frequency. Equation 4.2 is referred to as the quadratic phase error. If this delay is less than $\lambda/8$ when the element (i,j) is on the outer edge of the array then the distance $R_o$ is said to be in the far field of the array.

In order to usefully focus the array at $R_o$, it is necessary to have several wavelengths of phase error from the outer elements of the array. That is, the term focusing is used in this context to mean that the electric field from the array is concentrated in a desired spatial region. To what degree this can be accomplished is shown in Figure 4.11, which illustrates the vertical pattern of an array whose elements have been phased for focusing at 70 km. The array has 400,000 elements, $f = 300$ MHz, and a total width and length of 2000 $\lambda$. The peak of the pattern equals that of the $1/R^2$ dependence.
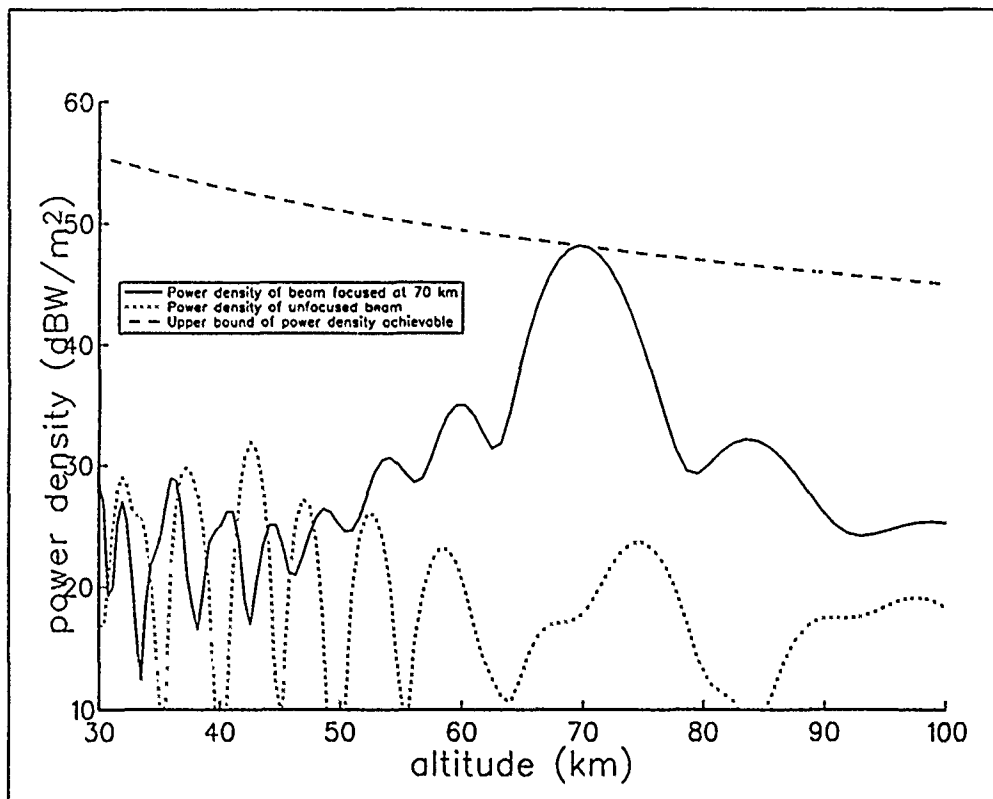


Figure 4.11. An Array Focused at 70 km

### 4.2.1  The Focusing Parameters and their Effects

The focused pattern is a picture of constructive and destructive interference of the fields from the individual elements of the array. The range extent of the focus depends on the ratio of focal range to aperture. The vertical half power width, $\Delta$, from the peak to the half power point is approximately

69

$$\Delta \approx 2 \lambda \left(\frac{R_0}{L}\right)^2 \tag{4.3}$$

where $L$ is the length of the array which is assumed square for equation (4.3). The corresponding power gradient at the half power point, grad $P$, is:

$$\text{grad } P \approx \frac{10}{\Delta} \tag{4.4}$$

Figures 4.12 and 4.13 illustrate these relationships. It is desirable that the power gradient be high since this directly determines the gradient of the electron density of the ionized cloud, which must be high to minimize RF refraction losses. Hence $\Delta$ should be small, preferably less than 2 km.
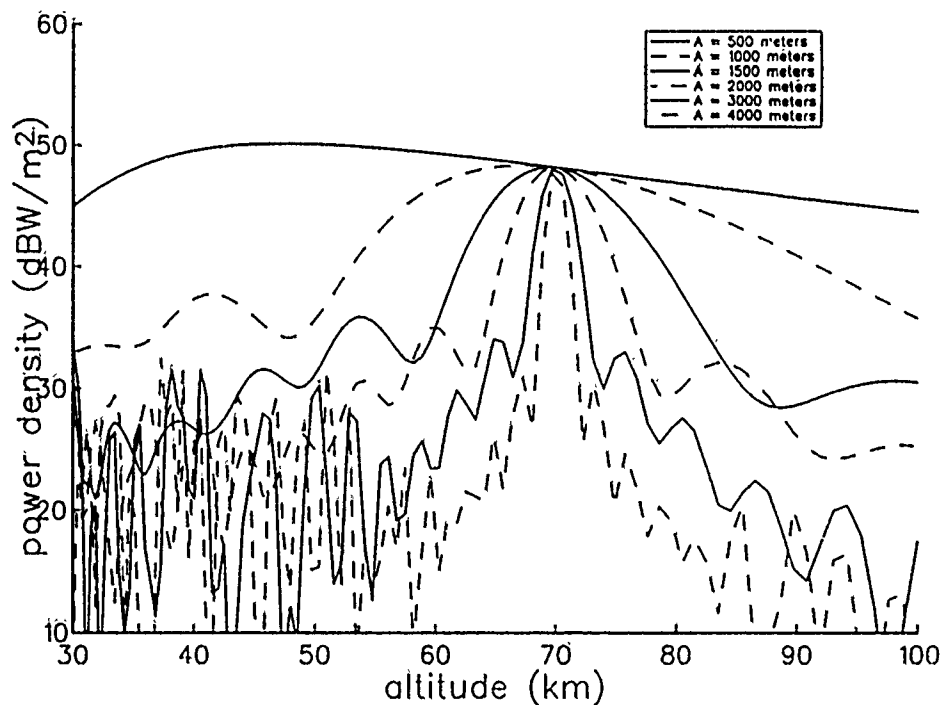


Figure 4.12. Focusing vs. Aperture ($f$ = 300 MHz, ERP = 156 dBW)

70
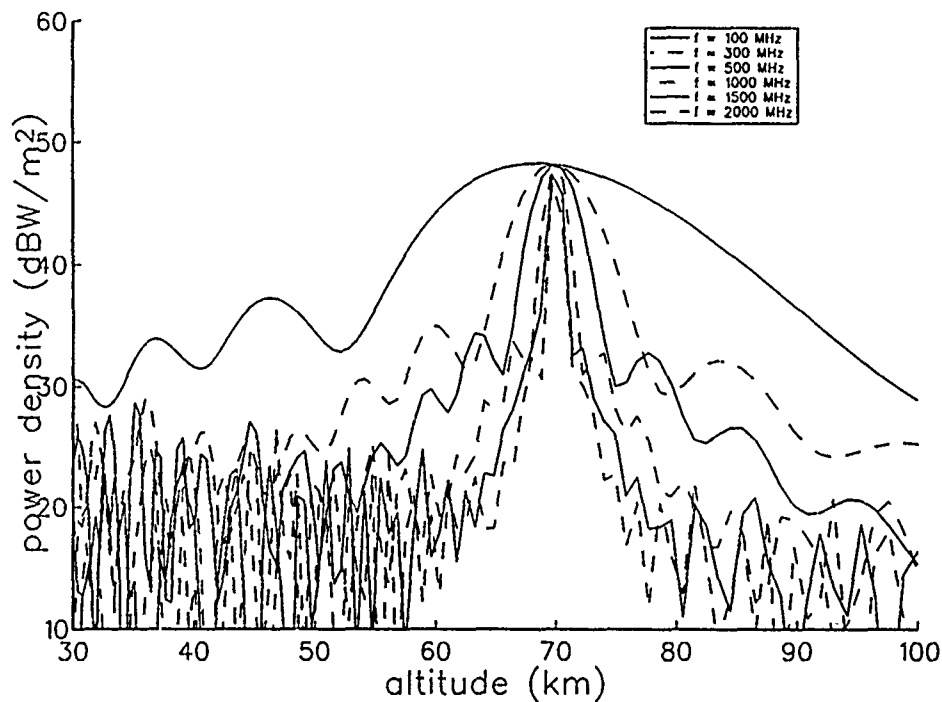
Figure 4.13. Focusing vs. Frequency ($L = 2$ km, ERP = 156 dBW)

For a 300 MHz heater frequency, a 70 km focal distance, and $\Delta < 2$km, Equation (4.3) requires an antenna aperture of 2 km across. Equation (4.3) indicates that aperture dimension $L$ scales with the square root of frequency.

It may not be practical or economically feasible to fill this entire aperture with elements[1], hence a thinned array is being considered for the AIM heater array. If the thinned array has its elements uniformly distributed, then there will be many grating lobes in the radiation pattern of the array, where significant numbers of elements add up in phase. These grating lobes can be eliminated by randomly or irregularly spacing the elements, causing the focal point to be the only place where *all* elements are in phase. For square arrays with 400 elements or more, the sidelobes can be kept down by at least 20 dB from the focal maximum. Figure 4.14 shows the pattern of the same heater array with its elements thinned in a uniform and a random way.

---

[1]The term element is used here to represent all conceivable antennas, that is, dipoles, slots, small or large horns, log-periodics, large parabolic reflectors, etc.

71
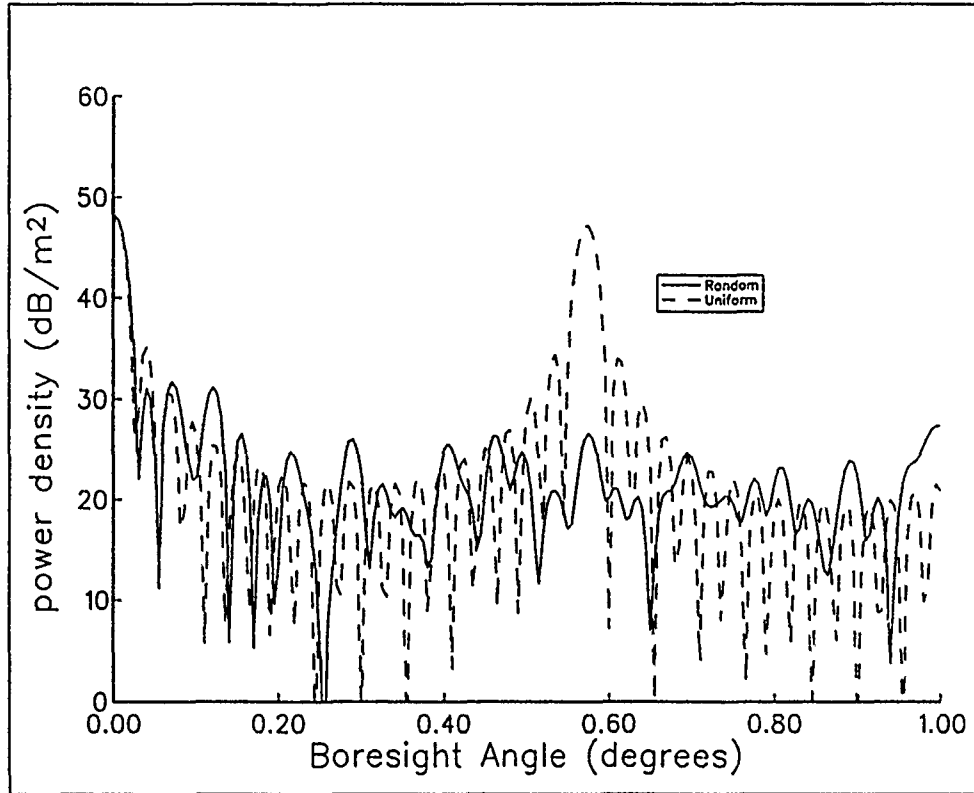
Figure 4.14. Element Positioning ($f = 300$ MHz, ERP = 156 dBW, $A = 2$ km)

Elimination of the grating lobes by this method transfers the power from the grating lobes into the average side lobe level. When the array elements are spread out or thinned the beamwidth of the main lobes reflects the total aperture size. If no new elements are introduced when the aperture is increased, then the peak power of the main lobe remains constant and it receives less of the total power as its beamwidth decreases. The ratio of power that the main lobe receives is directly proportional to the ratio of the effective radiating area and the total area of the array. In order to preserve the efficiency of the heater array, either the grating lobes must be utilized in creating the AIM cloud or the array can not be heavily thinned.

## 4.2.2 Heater Control Errors

The objective of the following analysis and associated discussion is to derive and evaluate some rough measures of sensitivity between the inherent uncertainties in generating the individual heater element waveforms, the resulting perturbations in AIM breakdown location, and subsequent impact on radar system performance. Deviations in waveform generation

at the element level result in corresponding deviations in the desired power density profile in the breakdown region. Three specific potential sources of error will be considered:

- simple additive noise,
- amplitude distortions, and
- phase distortions.

Examples of potential causes of these errors include quantization errors in the digital circuitry, digital-to-analog conversion errors, power amplifier gain deviations and distortions, and timing errors in the waveform control circuitry. Each of these factors is considered relative to what is readily achievable with current technology and how these performance limitations impact the patch integrity.

Results of this analysis indicates that although the power density/breakdown dependencies require relatively accurate control of the power density profile (e.g.. to within .003 dB, which corresponds to a SNR at the focal point of 68 dB), the large number of independent heater elements results in significant integration gains (e.g.. a design with 40,000 elements reduces the 68 dB requirement at the focal point by 46 dB to only 22 dB at the element level). A summary of the impact of this integration gain on what is achievable with currently available hardware technology is summarized in Table 4.1.

Table 4.1. Heater Error Budget Achievable with Currently Available Hardware

| Error Factor | Deviation in AIM Location |
| --- | --- |
| Quantization Noise | 0.13 m |
| D/A Noise | .009 m |
| Power Amplifier Distortions | < .13 m |
| Phase Deviations | .33 m |
| Cumulative Error | .36 m |

For an application requiring refraction of a 50 MHz RF, the patch irregularities indicated by the cumulative error is on the order of .06 wavelengths. An aperture with rms phase errors

of this order of magnitude will experience minimal performance degradation (less than .3 dB reduction in gain, less than .2% increase in beamwidth, and root-mean-square (rms) beam canting less than 10% of the beamwidth). Furthermore, when path averaging of the radar wave within the plasma is taken into account, the results indicate that the net effect on radar performance is negligible (~ .02 dB). (A complete discussion of the averaging phenomenon is given in section 5.6.)

In the following discussion, we derive the relationship between element waveform errors and the resulting error in plasma breakdown location. Each potential error source is related to an equivalent element waveform error. These two relationships are then combined to determine the sensitivity of the AIM breakdown location to each noise factor.

### 4.2.2.1 Sensitivity Relationships

Figure 4.15 illustrates the basic patch-heater geometry with the indicated parameters defined as:

| | | |
|---|---|---|
| $r$ | = | desired location of the array focus |
| $x_n$ | = | location of the $n$th heater element |
| $E(r,t)$ | = | desired electric field at location $r$ and time $t$ |
| $E_n(t)$ | = | desired element waveform |
| $g(\varphi_n)$ | = | element amplitude gain pattern, where $\varphi_n$ is the direction vector from the element. |

For a heater array with $N$ elements and $c$ denoting the speed of light, the ideal electric field intensity is given by the summed contributions from each element,

$$E(r,t) = \sum_{n=1}^{N} g\left(\frac{(r - x_n)}{\|r - x_n\|}\right) \cdot \frac{E_n(t - \|r - x_n\|/c)}{4\pi\|r - x_n\|^2} \tag{4.5}$$

Equation (4.5) provides the relationship between the electric field intensity at location $r$ and the ideal element waveforms. For a non-ideal waveform, we assume that $g(\varphi_n) \cdot E_n(t)$ has been perturbed by an additive noise process, $\eta_n$, which has zero mean and variance $E\{|\eta_n(t)|^2\} = \sigma_\eta^2$.

The actual contribution to $E(\underline{r},t)$ by each element is

$$g(\underline{\varphi}_n) \cdot E_n(t) + \eta_n(t)$$

In the analysis to follow, we assume the element errors are uncorrelated from element to element. This appears to be a reasonable assumption for the error sources mentioned above.[2] Given this assumption, the desired power density and potential noise power at $\underline{r}$ are

$$P_r = E\left\{|E(\underline{r},t)|^2\right\} = N^2 \cdot \frac{|E|^2}{2} \tag{4.6}$$

and

$$\sigma_{n_r}^2 = E\left\{\left|\sum_{n=1}^{N} \eta_n(t)\right|^2\right\} = N \cdot \sigma_\eta^2 . \tag{4.7}$$

In equations (4.6) and (4.7) we have approximated the $1/\|\underline{r} - \underline{x}_n\|^2$ spreading loss to be the same for each element, thus omitting the common $1/(4\pi R^2)$ factors from (4.6) and (4.7). In addition, to simplify the analysis, we assume that $E_n$ is generated such that $|g(\underline{\phi}_n) \cdot E_n| = |E|$ . Combining (4.6) and (4.7) gives the signal-to-noise ratio of the power density at the focal point of the heater

$$SNR = \frac{N \cdot |E|^2}{2\sigma_h^2} = N \cdot SNR_E \tag{4.8}$$

where $SNR_E$ is the signal-to-noise ratio at the output of each individual heater element.

---

[2] One possible exception is the timing circuitry. Timing errors due to system clock jitter would correlate across all of the heater elements. This is discussed in more detail at a later point in the paper.
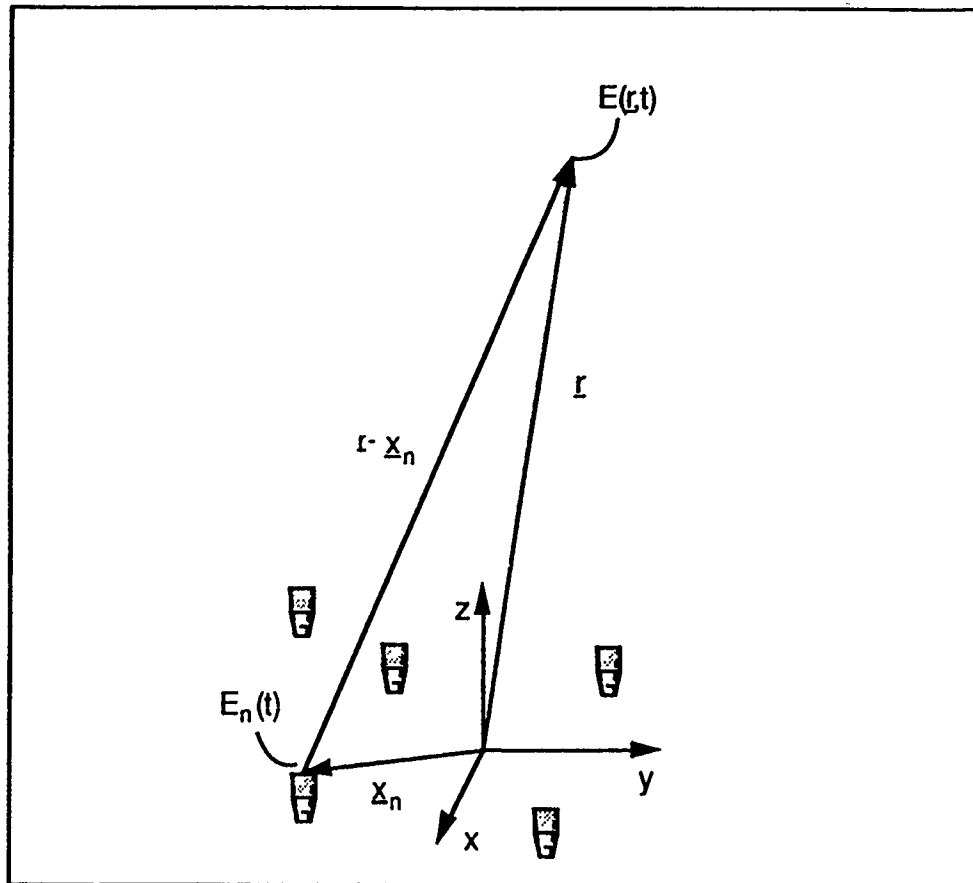
Figure 4.15. Geometry of Heater Array Sensitivity Analysis

In order to relate the SNR at the focus of the array to resulting irregularities in the patch breakdown location, we will consider the effects of deviations from the desired power density profile on breakdown location. Figure 4.16 illustrates a representative power density profile in one dimension with the corresponding plasma electron density after breakdown. In the region of breakdown, the power density is approximated by

$$10 \cdot \log_{10}(P) = \alpha \cdot z + \beta \tag{4.9}$$

where $z$ is the altitude from the heater array. Using (4.9), a small deviation in power, $\Delta P$, will result in a related offset in altitude, $\Delta z$,

$$\Delta z = \frac{10}{\alpha} \cdot \log_{10}(1 + \frac{\Delta P}{P_r}) \tag{4.10}$$

76

A linear approximation in (4.10) gives

$$\Delta z \approx \frac{10}{\alpha \cdot \log_e(10)} \cdot \frac{\Delta P}{P_r} \qquad (4.11)$$

If the $\eta_n$ 's are independent random processes, the central limit theorem implies that $\Delta z$ is a non-central chi-squared random variable, with mean and variance derived from (4.11)

$$E\{\Delta z\} \approx \frac{10}{\alpha \cdot \log_e(10)} \cdot \frac{\sigma_{\hat{n}_r}^2}{P_r} \qquad (4.12)$$

and

$$\sigma_{\Delta z}^2 \approx \left[\frac{10}{\alpha \cdot \log_e(10)}\right]^2 \cdot \frac{4 \cdot \sigma_{\hat{n}_r}^2}{P_r} \cdot \left(1 \cdot \frac{\sigma_{\hat{n}_r}^2}{2 \cdot P_r}\right) \approx \left[\frac{20}{\alpha \cdot \log_e(10)}\right]^2 \cdot SNR^{-1} . \qquad (4.13)$$



Figure 4.16. Illustration of the Breakdown Dependence Upon Power Density
Perturbations

Combining equations (4.8), (4.12), and (4.13) gives the rms deviation between the desired breakdown location, $z$, and the actual location, $z + \Delta z$,
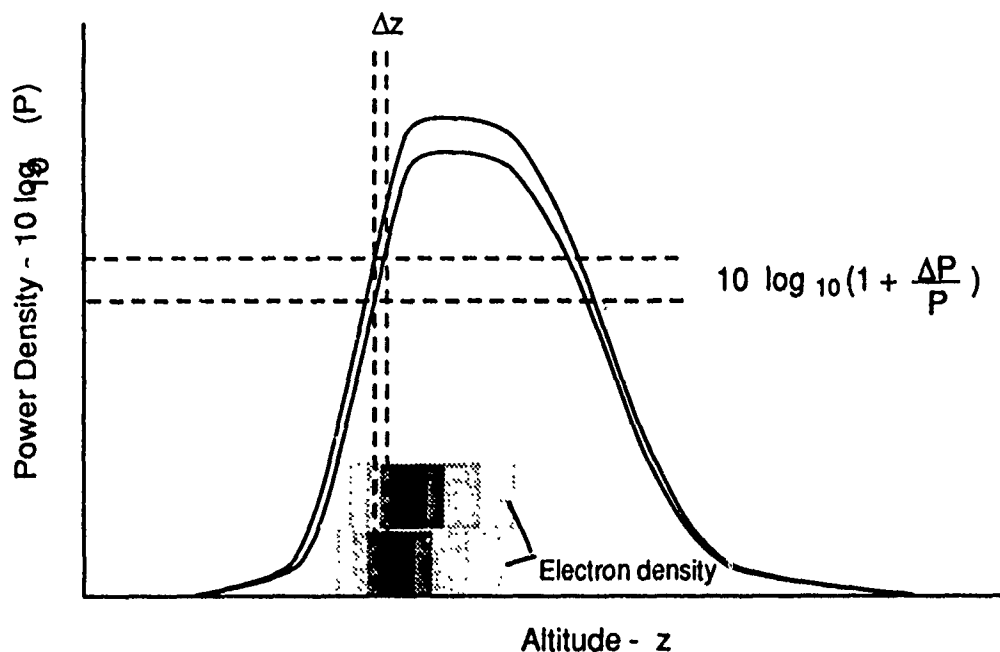
$$\text{rms}_{\text{error}} = \sqrt{\left(E\{\Delta z\}\right)^2 + \sigma_{\Delta z}^2} \approx \frac{20}{\alpha \cdot \log_e(10) \cdot \sqrt{N \cdot \text{SNR}_E}} \qquad (4.14)$$

In order to use (4.14) as the basis for evaluating the impact of potential heater array errors on patch location, each of the error sources to be evaluated must be tied to an equivalent additive noise error. For small scale errors, the three potential sources of error can be related to $\text{SNR}_E$ as shown in Table 4.2. In Table 4.2, $\gamma(t)$ corresponds to the relative amplitude distortion (i.e. $100 \cdot \sigma_\gamma$ is the percent rms distortion) and $\phi(t)$ is the absolute phase error.

Table 4.2. Equivalent Additive Element Noise $\text{SNR}_E$'s for Three Classes of Errors

| Additive Noise $\eta(t)$ | Amplitude Distortion $\gamma(t)$ | Phase Error $\phi(t)$ |
|:---:|:---:|:---:|
| $\dfrac{\|E\|^2}{2\sigma_\eta^2}$ | $\dfrac{1}{\sigma_\gamma^2}$ | $\dfrac{1}{2 \cdot \left(1 - e^{-\sigma_\phi^2/2}\right)}$ |

## 4.2.2.2 Sensitivity Trade-offs

In this section we combine the results $\omega$ 'able 4.2 with equation (4.14) to obtain a family of trade-off curves that indicate the expected rms AIM location error as a function of the error contributions of the three classes of error sources. For a given error budget assigned to each contributing factor, the total rms error can be found by

$$\text{rms}_{\text{total}} = \sqrt{\text{rms}_1^2 + \text{rms}_2^2 + \text{rms}_3^2} \qquad (4.15)$$

where $\text{rms}_i$ is the rms error due to factor $i$. Figure 4.17 shows the dependence of the rms breakdown location error on the element signal-to-noise ratio for three different power density gradients.
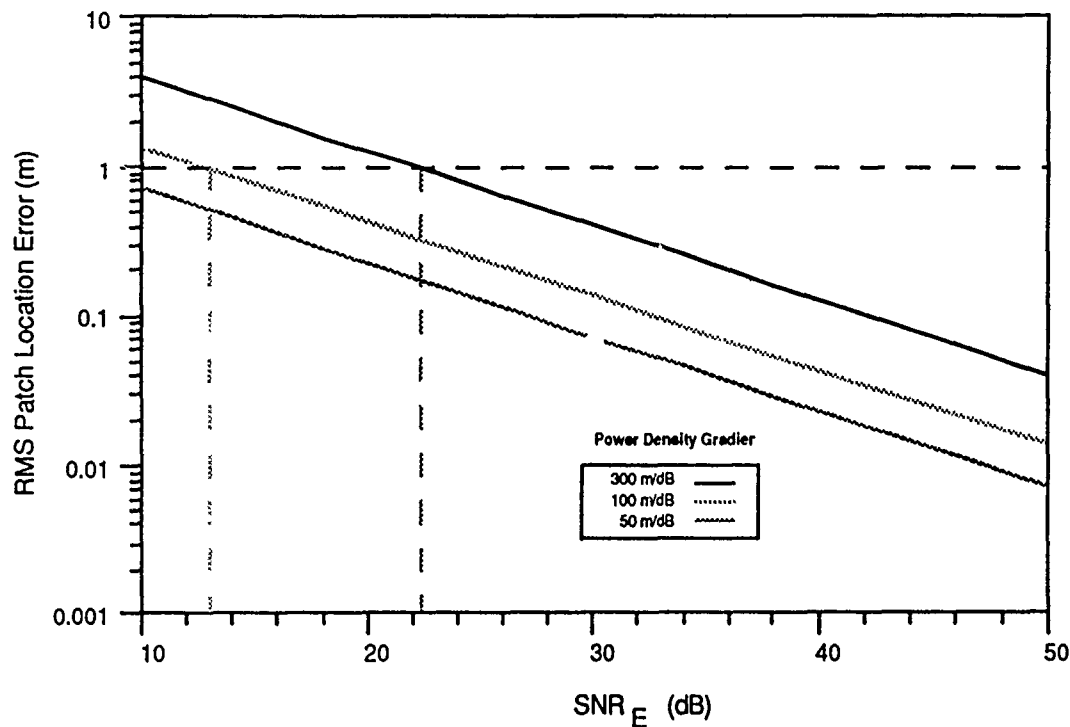
Figure 4.17. Sensitivity of Breakdown Location to
Heater Element Signal-to-Noise Ratio

Expressing the noise levels for $\eta(t)$ and $\gamma(t)$ in dB relative to the unperturbed waveform, the impact of these perturbations on $\Delta z$ can be assessed directly from Figure 4.17. Figure 4.18 gives the sensitivity of $\Delta z$ to the phase error, $\phi(t)$.

Table 4.3 provides an assessment of the achievable performance levels using currently available technology. These numbers have been obtained from vendor specification data sheets and in-house experience with related hardware. The cumulative rms error from all factors in Table 4.3 provide an rms deviation in breakdown altitude of no more than .36 meters. This corresponds to an rms deviation across the AIM patch of less than .06 wavelengths for a 50 Mhz RF.

79

Table 4.3. Impact of Achievable Heater Element Performance Factors on AIM Breakdown

| Error Factor | Achievable Performance | Equivalent $SNR_E$ | $\Delta z$ rms |
|---|---|---|---|
| Quantization Noise | 10 to 12 bits | 60 dB | 013 m |
| D/A Noise | $\sim\frac{1}{2}$ bit | 63 dB | .009 m |
| System Clock Jitter | $\sim\frac{1}{3}^{\circ}$ @ 350 Mhz | N/A[3] | N/A |
| Power Amplifier Distortion | < -40 dB THD @ 350 Mhz < 1° rms | > 40 dB | < .13 m |
| Phase Deviations | | > 32 dB | .33 m |
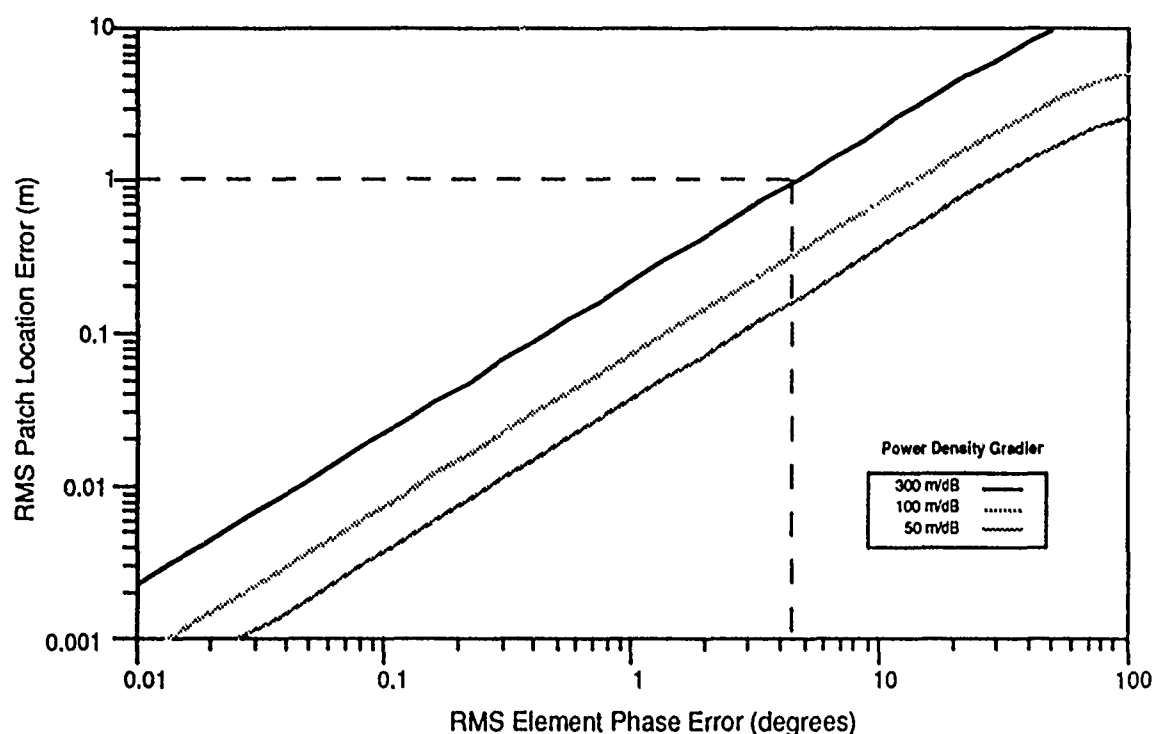


Figure 4.18. Sensitivity of Breakdown Location to Heater Element Phase Errors

---

[3] System clock jitter will affect all elements uniformly and will therefore result in a timing error, but not a power density perturbation.

### 4.2.3 Scanning the Focal Spot

In order to create a tilted cloud it will be necessary to refocus the array as the beam is scanned. Moving the focal point by changing the phase of each element of the heater in a very precise manner may not be practical for some heater designs. Moving the focal point away from its initial position will require changing the phase on each element individually. Figure 4.19 shows the required phase corrections on a series of elements at different distances from the center of the aperture for an antenna initially focused at 70 km.
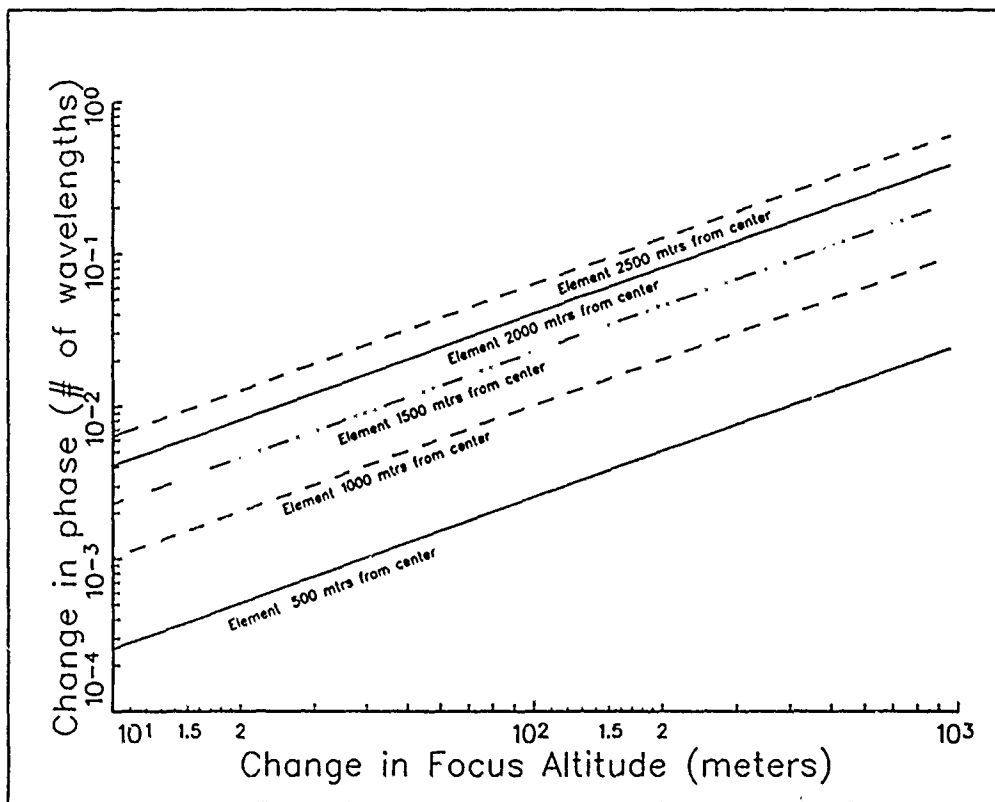


Figure 4.19. Vertical Scan with Phase Correction ($f$ = 300 MHz, ERP = 156 dBW)

The rms tolerance level, typically 1 degree is equivalent to $2.8 \times 10^{-3} \lambda$. As will be discussed in section 4.3, the AIM system requires the ability to do vertical scans in 1/4 beamwidth increments (approximately 10 meters), which is at the very edge of the rms tolerance level.

The second method of refocusing is accomplished by first setting the phases of all elements for the initial focal point and then moving the focal point by changing the frequency and

leaving the phase correction unaltered. If the heater frequency is slightly increased, then the phase correction at the original altitude is not exactly correct. In fact, the altitude where the electric field is at its maximum is now slightly higher than the original altitude. Of course, the phases at the peak are no longer perfectly constructive. Figure 4.20 illustrates this phenomenon.



When frequency is "chirped" to $f_2 > f_1$, energy concentrates here at $h_2$. ($\lambda_2 < \lambda_1$)

Original Focus at $h_1$ with frequency $f_1$

$h_2$

$h_1$

$m\lambda_2 < m\lambda_1$ is now the effective phase error

phase error $= m\lambda_1$
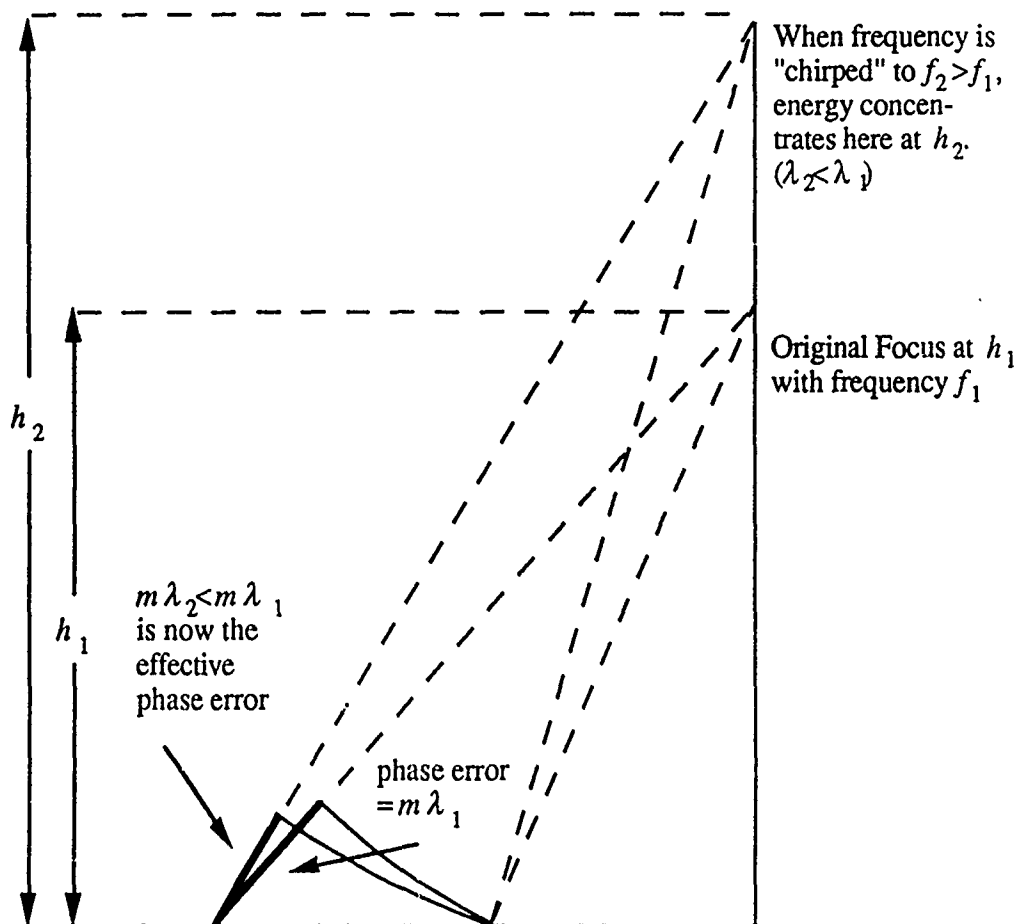
Figure 4.20. Effects of Frequency Chirping

Figure 4.21 shows the results of a simulation of frequency chirping. The heater is initially focused at 70 km using a frequency of 300 MHz. As the frequency is increased to 310 MHz the location of the peak moves to approximately 71 km. The simulation also shows that the loss in coherence since the phase match at the peak is not perfect is offset by the in-

crease in antenna gain due to the frequency chirp. In contrast to phase control, these slight changes in the heater frequency are within current technology constraints.
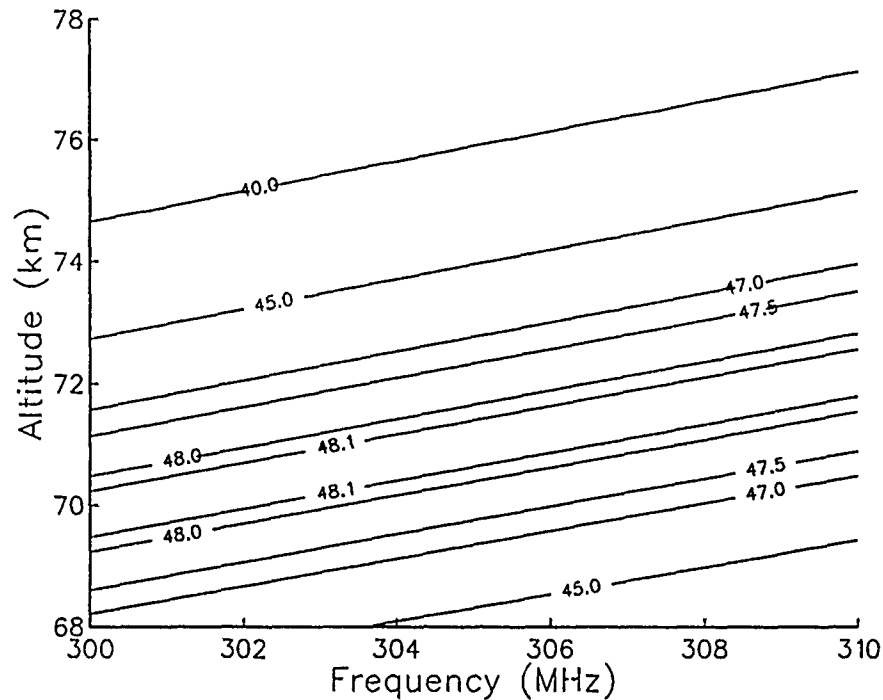


Figure 4.21. Power Density (dBW/m²) Contours of Vertical Scan With Frequency

## 4.2.4 Baseline Concept

This section describes the current baseline heater system and describes trade-off studies that have been performed to arrive at this baseline. There are two rather distinctive approaches for simultaneously obtaining the high ERP, achieving the positive field gradient needed for controlled breakdown, and controlling the plasma cloud:

1) a large sparse, solid-state phased array, or
2) high-power tubes (klystrons, likely) feeding numerous dishes.

Our current understanding of the phenomenology and the available technology leads us to favor the solid-state approach for the Full Scale Engineering Development system because

83

of its greater controllability, simple CW pulse generation, likely lower life cycle costs, and greater reliability. The tube approach is currently favored for an atmospheric proof of principle demonstration because of its lower development cost.

Based on APTI's study of the plasma creation process and associated control requirements, formation of an AIM that will efficiently reflect HF/VHF waves requires a heater with baseline design characteristics as follows:

- Heater frequency in the UHF band,
- Moderate (about 10%) frequency agility,
- Antenna gain of 70 dB,
- Peak transmitter power of 86 dBW,
- Duty cycle of 0.1-5 %, and
- Flexible and accurate control of the E field focus.

APTI's baseline concept for the heater antenna consists of a large, sparse phased array (about 4 km$^2$) with solid state transmit elements, each radiating about 1 KW at a nominal frequency of 425 MHz (Figure 4.22). It is envisioned that the array will consist of a sparse grid of 16,000 irregularly-spaced panels, each consisting of a sub-array of 25 uniformly-spaced 1 m$^2$ aperture elements.

To support the requirement for near-field focusing of the heater, each sub-panel will be digitally calibrated and synchronized. Reference signals will be measured by receivers used to provide calibration for each sub-panel. Digital control and waveform synthesis will provide very accurate synchronization of the transmit waveforms, allowing complete flexibility in synthesizing the field distribution at the breakdown region by specifying the phase and amplitude weights for each sub-panel as shown in Figure 4.23. Digitally encoded samples of the desired transmit waveform are clocked at 1 GHz to an ultra-fast digital-to-analog converter (DAC), the output of which is fed to the RF input to the panel amplifier and antenna elements.

**ALL SOLID STATE TRANSMITTER**

**DIGITAL WAVEFORM SYNTHESIS & CONTROL**

**LOW POWER DENSITY AT THE ANTENNA**

**IRREGULAR SPACING FOR GRATING LOBE CONTROL**

**WAVEFORM/BEAMSTEERING COMMANDS DISTRIBUTED OVER FIBER OPTIC OR RF LINK**

PAIR OF REFERENCE/TRIGGER ANTENNAS

SUBARRAY PANEL

Panels have only power cables; no signal cables

1 km

1 km

SPARSE, NONUNIFORMLY-SPACED ANTENNA ARRAY

Figure 4.22. The FSED AIM Heater Phased Array Antenna

An alternate approach would consist of an array of reflectors up to 25 meters in diameter driven by high powered L or S band klystrons. The number of reflectors may vary from 25 to several thousand depending on the size of the reflector, AIM requirements, and output characteristics of the klystron. The number of klystrons may vary from 10 to several hundred depending on their output. A design for a L band klystron with 1 GW output power for a 1 microsecond pulse has been proposed. There exists a commercially available L band klystron at 250 MW with a 1 $\mu$sec pulse. This array of reflectors could be focused as the baseline concept with digital waveform synthesis and control, or by frequency means, as described above. The ultimate choice will be determined based on system trade-offs of AIM creation phenomenology, performance requirements, and cost.
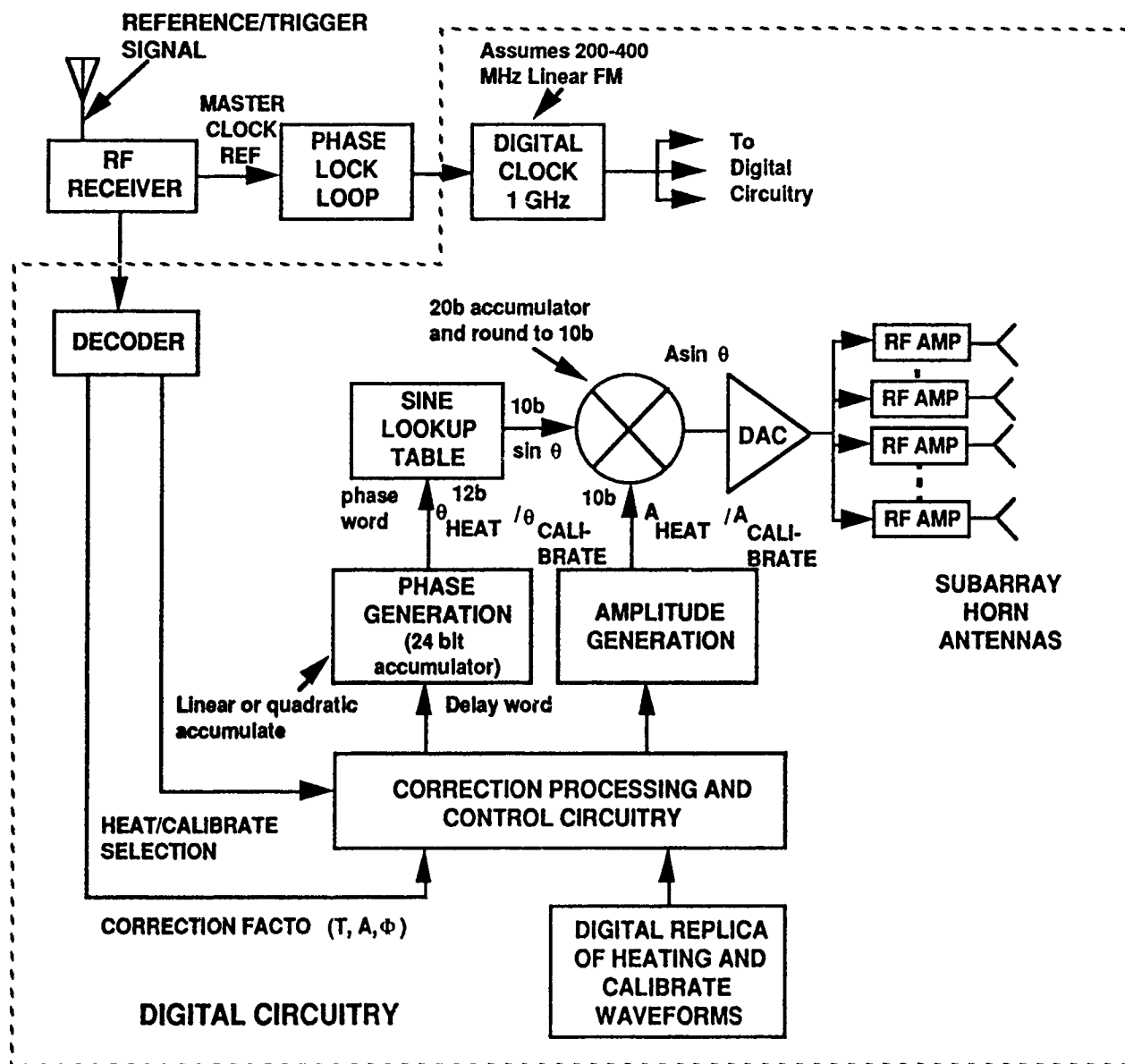
Figure 4.23. The AIM Heater Antenna With Digital Waveform Synthesis and Control

## 4.3 Two-Dimensional Plasma Formation Model

APTI's investigation of the AIM cloud formation process has led to the creation, implementation and use of a two-dimensional plasma formation model to help answer questions that can not be addressed by the one-dimensional model described in section 4.1. Principle among these are the effects of discrete scanning of the heater beam on the AIM cloud and the total AIM cloud formation time.

### 4.3.1 Mechanics of the Code

The algorithm of the plasma formation code is basically unchanged from the one-dimensional version described in section 6.1. The extension of this algorithm to two dimensions is straight forward. We now have a two-dimensional grid of points on a vertical plane in the atmosphere, and a second mobile 2-D grid of points describing the microwave pulse of energy. As before, the pulse propagates upwards with time. The width of the pulse is 3 times the half-power beamwidth of the heater antenna. This insures that all pertinent parts of the pulse are included. Figure 4.24 illustrates the mechanics of the code.
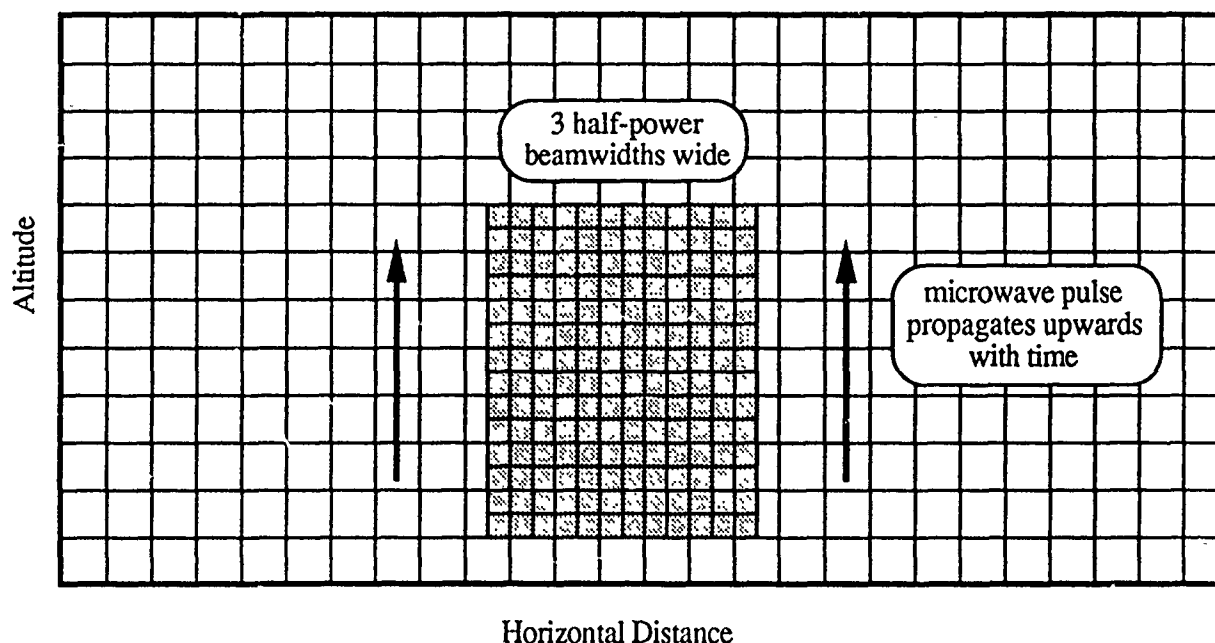


Figure 4.24. Two-Dimensional Enhancements to Plasma Formation Code

After one pulse has gone completely through the grid the simulation scans the heater horizontally (with phase) and upwards vertically (with frequency as described in section 4.2.3) and then sends another pulse. The amount of ionization that occurs off of boresight depends on shape of the beam and on the beamwidth. In this simulation, the horizontal shape of the beam is taken into account, and the resulting differences in ionization over the extent of the beam can be studied. The next section presents an analytic discussion of finite step discrete scanning and consequent AIM irregularities.

## 4.3.2 Beam Scanning Effects

In the following discussion, we address the issue of AIM irregularities due to finite step heater beam motion in the direction of the AIM inclination. Figure 4.25 illustrates the step scanning of the heater beam along a short segment of the AIM contour. In this figure, the heater dwells for a given time, $\tau$ seconds, and then steps the focal point a third of a beamwidth in the cross beam direction and a corresponding distance in the bore-sight direction. This dwell and step process is repeated for the extent of the AIM. As Figure 4.25 shows, while the desired constant electron density contour is a line inclined at 45°, the actual contour due to the quantization of the beam step has a ripple that oscillates about the desired contour. This irregularity in the AIM will produce a corresponding ripple in the phase front of the refracted wave. The extent of wavefront ripple will depend both upon the magnitude of the contour ripple, as well as the depth of the plasma density. A deeper plasma provides more refraction and correspondingly more smoothing of the AIM irregularity, thus less phase front distortion as discussed in earlier sections.
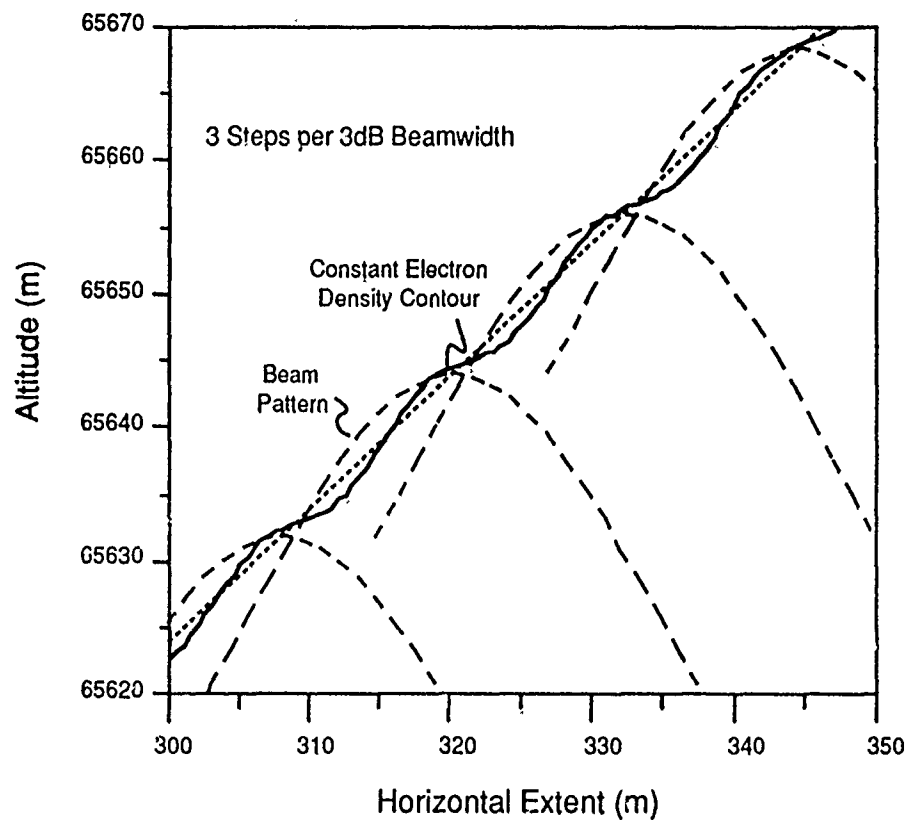
Figure 4.25. Illustration of Heater Step Scanning

The objective of this section is to quantify the magnitude of these contour fluctuations and determine what beam step sizes are required for acceptable system performance. These irregularities are studied both from an analytic perspective, as well as a straight forward numerical simulation of the heater step scanning and consequent ionization along the desired constant electron density contour. Quantitative results are provided for the analytic derivations and compared to electron density irregularities produced by the numerical simulation. These results indicate that, within the nominal parameter regime for the current AIM conceptual design,

1) the magnitude of electron density irregularities falls off rapidly for paint step sizes less than 1/2 beam width and

2) a 1/4 beam step size produces a density fluctuation with magnitude less than .1% of the average and a corresponding location fluctuation less than .1 m.

The next section presents a derivation of the analytic relationships. These relationships are then used in Section 4.3.2.2 to derive trad_-off expressions for a specific heater beam example. Section 4.3.2.3 uses this result to present a quantitative trade-off between beam step size and resulting density fluctuations. In addition, Section 4.3.2.3 compares the analytic results with a numeric simulation of a stepped heater beam and associated ionization.

## 4.3.2.1 Analysis Of Stepped Beam Induced Density Fluctuations

In the following discussion, the heater array is assumed to be centered at $(x,z) = (0,0)$ and is painting a patch by stepping the beam focus from $(- D_x/2, z_f - \gamma D_x/2)$ to $(- D_x/2, z_f - \gamma D_x/2)$. Figure 3.17a illustrates. Each step moves the beam uniformly in $x$ and $z$, $(\delta x, \delta z) = (\Delta, \gamma \Delta)$.
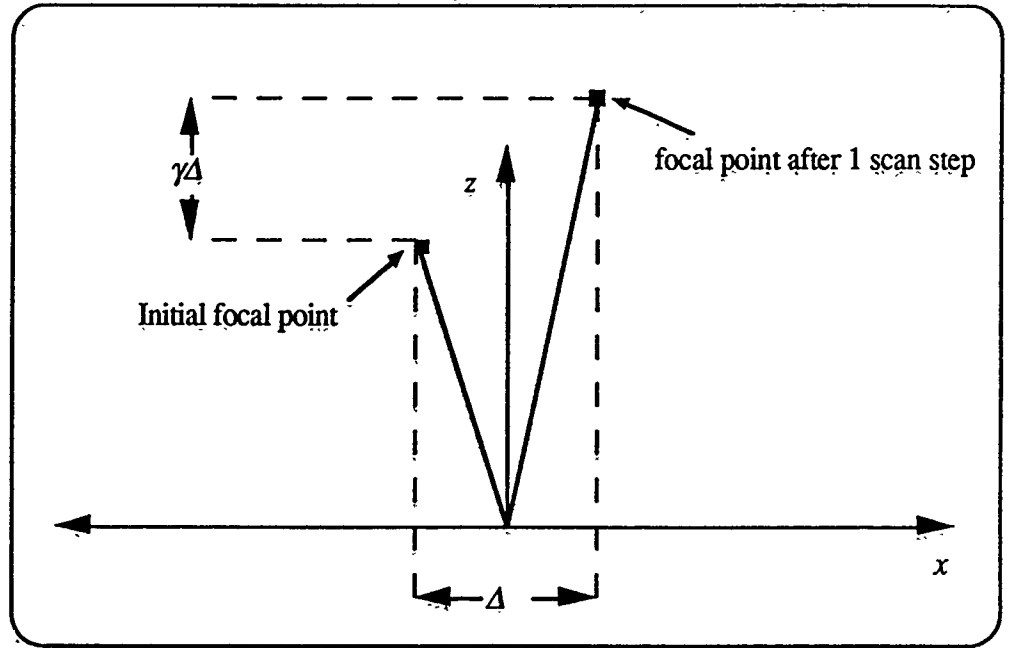
Figure 4.25a. Geometry of Beam Scanning Effects Study

The power density of the heater[4] can be described at the nth beam step by

$$P_n(x,z) = P_0 \cdot g(x\text{-}n\Delta, z n \Delta \gamma) \tag{4.16}$$

where $g(x,z)$ is the heater beam relative gain pattern ($g(0, z_f) = 1$) in the $(x, z)$ coordinates and $P_o$ is the heater power density at the focus. For a step size $\Delta = \dfrac{D_x}{N}$, the cumulative energy per square meter is found by summing the contribution of each beam dwell at $(x, z)$

$$E(x, z) = \sum_{n=-N/2}^{N/2} P_o \cdot \left(g x - n\Delta, z - n\Delta\gamma\right) \cdot \tau \tag{4.17}$$

To simplify the following analysis, we assume that $g(x, z)$ takes on a particularly convenient form

---

[4] In this analysis we have ignored the effects of self absorption on the heater wave. While this is an important phenomenon during the the patch creation process (leading to the self-limiting nature of the peak electron density), the effect on the fluctuation appears to be one of limiting the electron density to some maximum. This will lead to fluctuations in practice that are less than those predicted here.

$$g(x, z) = g\left(ax^2 + b(z - z_f)^2\right) \qquad (4.18)$$

This form implies that the gain depends upon a weighted distance between $(x, z)$ and the focal point $(0, z_f)$, where the weights, $a$ & $b$, determine the beamwidth and width of focus respectively. While this form is not completely general, it does allow for a wide class of beam patterns, such as $\exp(-d^k)$ and $\left(\frac{\sin d}{d}\right)^k$ in the focal region of the beam, where $d = \sqrt{ax^2 + b(z - z_f)^2}$. For a pattern satisfying (4.18), we can show that

$$g\left(x - n\Delta, z - n\Delta\gamma\right) = g\left(\frac{ab(x\gamma - (z - z_f))^2}{a + b\gamma^2} + (a + b\gamma^2) \cdot \left(n\Delta - \frac{(ax + b\gamma(z - z_f))^2}{a + b\gamma^2}\right)\right) \qquad (4.19)$$

and, for a contour in the $(x, z)$ plane defined by $(z - z_f) = \xi + \gamma x$, we have

$$g(x; \xi) = g\left(\frac{ab\xi^2}{a + b\gamma^2} + (a + b\gamma^2) \cdot \left(n\Delta - x - \frac{b\gamma}{a + b\gamma^2}\xi\right)^2\right) \qquad (4.20)$$

If we now define

$$h(u; \xi) = g\left(\frac{ab\xi^2}{a + b\gamma^2} + (a + b\gamma^2) \cdot u^2\right) \qquad (4.21)$$

the energy flux per square meter along the contour can be approximated by

$$E(x, z) \approx \sum_{n = -\infty}^{\infty} P_o \cdot h\left(n\Delta - x - \frac{b\gamma}{a + b\gamma^2}\xi; \xi\right) \cdot \tau$$

$$= \tau P_o \int_{-\infty}^{\infty} h\left(u - x - \frac{b\gamma}{a + b\gamma^2}\xi; \xi\right) \sum_{n = -\infty}^{\infty} \delta(u - n\Delta) \, du$$

91

$$E(x,z) = \tau P_o \int_{-\infty}^{\infty} h\left(u - x - \frac{b\gamma}{a+b\gamma^2}\xi; \xi\right) \sum_{n=-\infty}^{\infty} \exp\left(j2\pi\frac{n}{\Delta}u\right) du$$

$$= \tau P_o \sum_{n=-\infty}^{\infty} H^*(n/\Delta; \xi) \cdot \exp\left(j2\pi\frac{n}{\Delta}x + j2\pi\frac{n}{\Delta}\frac{b\gamma\xi}{a+b\gamma^2}\right) \qquad (4.22)$$

$$= \tau P_o\left(H(0; \xi) + \sum_{n=1}^{\infty} 2H(n/\Delta; \xi) \cdot \cos\left(2\pi\frac{n}{\Delta}x + \phi_n(\xi)\right)\right)$$

In Equation (4.22) $H(f; \xi)$ is the Fourier transform of $h(u; \xi)$ in the $u$ variable,

$$H(f; \xi) = \int_{-\infty}^{\infty} h(u; \xi) \exp(-j2\pi fu)\, du \qquad (4.23)$$

Equation (4.22) shows that the energy flux along contours parallel to the AIM surface consists of an average flux, $\tau P_0 \cdot H(0; \xi)$, and a fluctuation with period equal to the beam step size. The Fourier coefficients of the fluctuation are given by the Fourier transform of the beam pattern at frequencies $\frac{n}{\Delta}$. For beam patterns and step sizes of interest to us, the majority of fluctuation is contained in the first harmonic, $f_x = 1/\Delta$. From (4.22), the first harmonic ripple relative to the average is

$$\delta_E = \frac{2H(1/\Delta; \xi)}{H(0; \xi)} \qquad (4.24)$$

While the energy flux represented by equation (4.22) is related to the ionization rate and consequent electron density, the relationship is highly nonlinear and therefore (4.22) only gives a sense of how the resulting density irregularities will depend upon the heater step size. Derivation of a more accurate relationship follows.

The electron ionization rate has been shown to have the following dependence on heater power density

$$v_i(x,z;n) = N_o \cdot A_2 \cdot \exp(-P_B / P_n(x, z)) \cdot \exp\left(-\sqrt{20P_B / P_n(x, z)}\right) \qquad (4.25)$$

where $N_o$ is the ambient neutral density, $P_B$ is the critical power density required for breakdown, and $A_2$ is a scaling constant. Along the $\xi$ contour the ionization rate can be written as a function of $h(u; \xi)$

$$v_i(x; \xi, n) = v\left(\frac{P_o}{P_B} \cdot h\left(n\Delta - x - \frac{b\gamma}{a + b\gamma^2}\xi; \xi\right)\right) \qquad (4.26)$$

Since the buildup of electron density in the regime of interest for AIM is of the cascade type, it is described by an exponential function of $\int v_i(t)dt$. Using (4.26) for the ionization rate during the nth beam dwell and letting $N_a(x, \xi)$ denote the ambient electron density, the electron density after the complete heater scan is

$$N_e(x; \xi) = N_a(x; \xi) \cdot \exp\left(\sum_{n=-N/2}^{N/2} v\left(\frac{P_o}{P_B} \cdot h\left(n\Delta - x - \frac{b\gamma}{a + b\gamma^2}\xi; \xi\right)\right) \cdot \tau\right)$$

$$\approx N_a(x; \xi) \cdot \exp\left(\tau \cdot \left\{N(0; \xi) + \sum_{n=1}^{\infty} 2N(n/\Delta; \xi) \cdot \cos\left(2\pi\frac{nx}{\Delta} + \phi_n(\xi)\right)\right\}\right) \qquad (4.27)$$

$$\approx N_a(x; \xi) \cdot \exp(\tau \cdot N(0; \xi))\left\{1 + \tau \cdot \sum_{n=1}^{\infty} 2N(n/\Delta; \xi) \cdot \cos\left(2\pi\frac{n}{\Delta}x + \phi_n(\xi)\right)\right\}$$

where

$$N(f; \xi) = \int_{-\infty}^{\infty} v\left(\frac{P_o}{P_B} \cdot h(u; \xi)\right)\exp(-j2\pi fu) \, du \qquad (4.28)$$

The steps for deriving (4.27) are analogous to Equation (4.22). Equation (4.27) shows that the electron density along contours parallel to the AIM surface will exhibit fluctuations due to heater beam step scanning. These fluctuations have a period equal to the beam step size, $\Delta$, with a relative first harmonic fluctuation magnitude proportional to the beam dwell time and the value of the Fourier transform in (4.28) at $f_x=1/\Delta$. If we let the average electron density on contour $\xi$ be defined as

$$N_{e,ave} = N_a(x; \xi) \cdot \exp(\tau \cdot N(0; \xi)) \qquad (4.29)$$

the relative fluctuation in the first harmonic is

$$
\begin{aligned}
\delta_{N_e} &= \frac{\delta N_e}{N_{e,ave}} \\
&= \tau \cdot 2N(1/\Delta; \xi) \qquad (4.30) \\
&= \log\left(\frac{N_{e,ave}}{N_a(x; x)}\right) \cdot \frac{2N(1/\Delta; \xi)}{N(0; \xi)}
\end{aligned}
$$

### 4.3.2.2  An Illustrative Example

In the following discussion we use the results in Section 4.3.2.1 with a specific heater beam pattern to develop explicit relationships for Equations (4.24) and (4.31). For the purpose of illustration we assume a gaussian beam pattern in the focal region of the heater. For a 3 dB half-width of $B_x$ and $B_z$ in the $x$ and $z$ directions respectively, the heater beam pattern is expressed as

$$g(x, z) = \exp\left( \ln\left(\frac{1}{2}\right)\left(\frac{x^2}{B_x^2} + \frac{(z - z_f)^2}{B_z^2}\right) \right) \qquad (4.31)$$

Using (4.18) and (4.31) to identify the appropriate expressions for $a$ and $b$, (4.31) can be written in the same form as (4.18); hence, equation (4.21) gives

$$h(u; \xi) = \exp\left(\frac{\ln\left(\frac{1}{2}\right)\xi^2}{B_z^2 + \gamma^2 B_x^2}\right) \cdot \exp\left(\frac{\ln\left(\frac{1}{2}\right) \cdot (B_z^2 + \gamma^2 B_x^2)}{B_z^2 \cdot B_x^2} \cdot u^2\right) \qquad (4.32)$$

The Fourier transform of (4.32) in the $u$ variable may be performed analytically, producing

$$H(f; \xi) = \sqrt{\frac{\pi B_z^2 B_x^2}{-\ln\left(\frac{1}{2}\right)(B_z^2 + \gamma^2 B_x^2)}} \exp\left(\frac{\ln\left(\frac{1}{2}\right)\xi^2}{B_z^2 + \gamma^2 B_x^2}\right) \cdot \exp\left(\frac{\pi^2 B_z^2 B_x^2}{\ln\left(\frac{1}{2}\right)(B_z^2 + \gamma^2 B_x^2)} \cdot f^2\right) \qquad (4.33)$$

Substituting (4.33) into (4.25) and simplifying gives the relative energy fluctuation along the AIM surface contour

$$\delta_E = \frac{2H(1/\Delta; \xi)}{H(0; \xi)} = 2 \cdot \exp\left( \frac{\pi^2}{\ln\left(\frac{1}{2}\right)} \cdot \frac{B_x^2 B_z^2}{B_z^2 + \gamma^2 B_x^2} \cdot \left(\frac{1}{\Delta}\right)^2 \right) \qquad (4.34)$$

Figure 4.26 shows a plot of $\delta_E$ as a function of $\frac{2B_x}{\Delta}$, the number of heater scanning increments per beamwidth. Although this plot is for specific parameter values, $B_x = 36$ m and $B_z = 2{,}700$ m, the results are widely applicable across the potential operational regime of the AIM heater; since, for $B_x \ll B_z$,

$$\delta_E = 2 \cdot \exp\left( \frac{\pi^2}{4 \ln\left(\frac{1}{2}\right)} \cdot \left(\frac{2B_x}{\Delta}\right)^2 \right) \qquad (4.35)$$

In order to obtain a closed form expression for the ionization rate and resulting electron density, we will approximate the ionization rate by a *Kth* order polynomial in $\frac{P_n}{P_B}$ . Substituting (4.32) into (4.35), defining $\xi_B$ such that $P_B = P_o \cdot g(0, z_f + \xi_B)$, and using the polynomial approximation,

$$\nu\left(\frac{P_n}{P_B}\right) \approx N_o \cdot A \cdot \sum_{k=1}^{K} a_k \left(\frac{P_n}{P_B}\right)^k$$

$$= N_o \cdot A \cdot \sum_{k=1}^{K} a_k \left( \begin{array}{c} \exp\left( k \cdot \ln\left(\frac{1}{2}\right) \cdot \left( \frac{\xi^2}{B_z^2 + \gamma^2 B_x^2} - \frac{\xi_B^2}{B_z^2} \right) \right) \\ \cdot \exp\left( \frac{k \cdot \ln\left(\frac{1}{2}\right) \cdot \left(B_z^2 + \gamma^2 B_x^2\right)}{B_z^2 \cdot B_x^2} \cdot u^2 \right) \end{array} \right) \qquad (4.36)$$

95
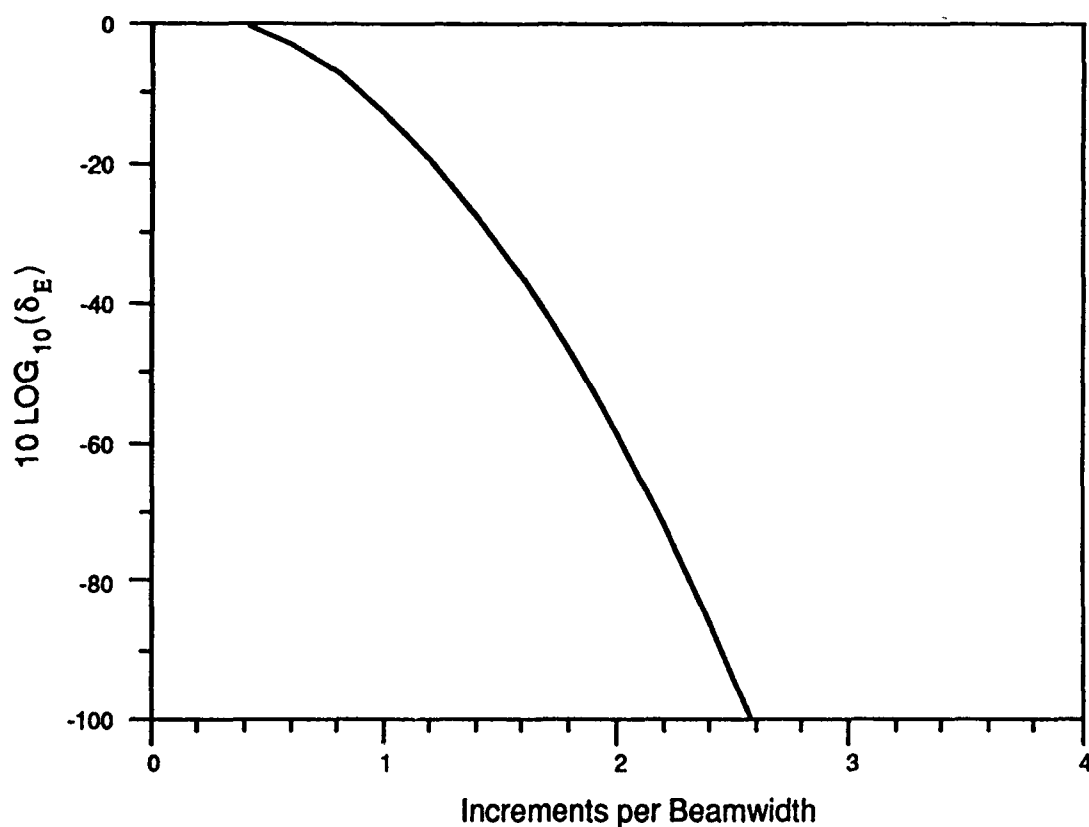
Figure 4.26. Fluctuation in Energy Flux Versus Scanning Increment

Substituting equation (4.36) into (4.28) and performing the integration gives the following Fourier transform of $v$:

$$v(f; \xi) = N_o \cdot A \cdot \sqrt{\frac{\pi B_z^2 B_x^2}{-\ln\left(\frac{1}{2}\right)\left(B_z^2 + \gamma^2 B_x^2\right)}}$$

$$\cdot \sum_{k=1}^{K} \frac{a_k}{\sqrt{k}} \left\{ \exp\left(k \ln\left(\frac{1}{2}\right)\left(\frac{\xi^2}{B_z^2 + \gamma^2 B_x^2} - \frac{\xi_B^2}{B_z^2}\right)\right) \exp\left(\frac{\pi^2 B_z^2 B_x^2}{k \cdot \ln\left(\frac{1}{2}\right)\left(B_z^2 + \gamma^2 B_x^2\right)} f^2\right) \right\}$$

(4.37)

Finally, using (4.37) to evaluate (4.30),

$$
\delta_{N_e} = \log\!\left(\frac{N_{e,ave}}{N_a(x;\,\xi)}\right)
$$

$$
\cdot\;\frac{2\displaystyle\sum_{k=1}^{K}\frac{a_k}{\sqrt{k}}\left\{\exp\!\left(k\,\ln\!\left(\tfrac{1}{2}\right)\!\left(\frac{\xi^2}{B_z^2+\gamma^2 B_x^2}-\frac{\xi_B^2}{B_z^2}\right)\right)\exp\!\left(\frac{\pi^2 B_z^2 B_x^2}{k\cdot\ln\!\left(\tfrac{1}{2}\right)\left(B_z^2+\gamma^2 B_x^2\right)}\cdot\left(\tfrac{1}{\Delta}\right)^2\right)\right\}}{\displaystyle\sum_{k=1}^{K}\frac{a_k}{\sqrt{k}}\left\{\exp\!\left(k\,\ln\!\left(\tfrac{1}{2}\right)\cdot\left(\frac{\xi^2}{B_z^2+\gamma^2 B_x^2}-\frac{\xi_B^2}{B_z^2}\right)\right)\right\}}
\tag{4.38}
$$

As was indicated above, over the parameter regime relevant to AIM, $B_x \ll B_z$; therefore, (4.38) may be approximated by

$$
\delta_{N_e} = \log\!\left(\frac{N_{e,ave}}{N_a(x;\,\xi)}\right)\cdot\;\frac{2\displaystyle\sum_{k=1}^{K}\frac{a_k}{\sqrt{k}}\left\{\exp\!\left(\frac{k\cdot\ln\!\left(\tfrac{1}{2}\right)}{B_z^2}\cdot\left(\xi^2-\xi_B^2\right)\right)\cdot\exp\!\left(\frac{\pi^2}{k\cdot 4\ln\!\left(\tfrac{1}{2}\right)}\cdot\left(\frac{2B_x}{\Delta}\right)^2\right)\right\}}{\displaystyle\sum_{k=1}^{K}\frac{a_k}{\sqrt{k}}\left\{\exp\!\left(\frac{k\cdot\ln\!\left(\tfrac{1}{2}\right)}{B_z^2}\cdot\left(\xi^2-\xi_B^2\right)\right)\right\}}
\tag{4.39}
$$

### 4.3.2.3  Quantitative Results

A numerical simulation has been performed for a specific set of heater beam parameters. The simulation uses the one dimensional breakdown model, as defined in line 1 of Equation (4.27), for a fixed value of $\xi$ over a range of $x$ encompassing the patch. Figure 4.27 shows the results of this simulation over a short segment of the patch for the following heater beam parameters:

Table 4.4. Heater Beam Parameters

| | | | | | |
|---|---|---|---|---|---|
| $z_f$ | = | 72,000 m | $\xi_B$ | = | -5,500 m |
| $B_x$ | = | 36 m | $B_z$ | = | 2,750 m |
| $\xi$ | = | -4,675 m | $\tau\frac{2B_x}{\Delta}$ | = | 55 μsec |

The fluctuation level measured for this simulation is compared to the analytic predictions derived in the previous section. In order to quantify equation (4.40), a 12th order polynomial approximation to $v\left(\frac{P}{P_B}\right)$ was derived by selecting polynomial coefficients to minimize the mean-square-error, over the power density range of interest. Figure 4.28 compares the the resulting approximation with the actual curve for Equation (4.27) over the range .1 to 10. This includes the range of $\frac{P(x; \xi)}{P_B}$ values along
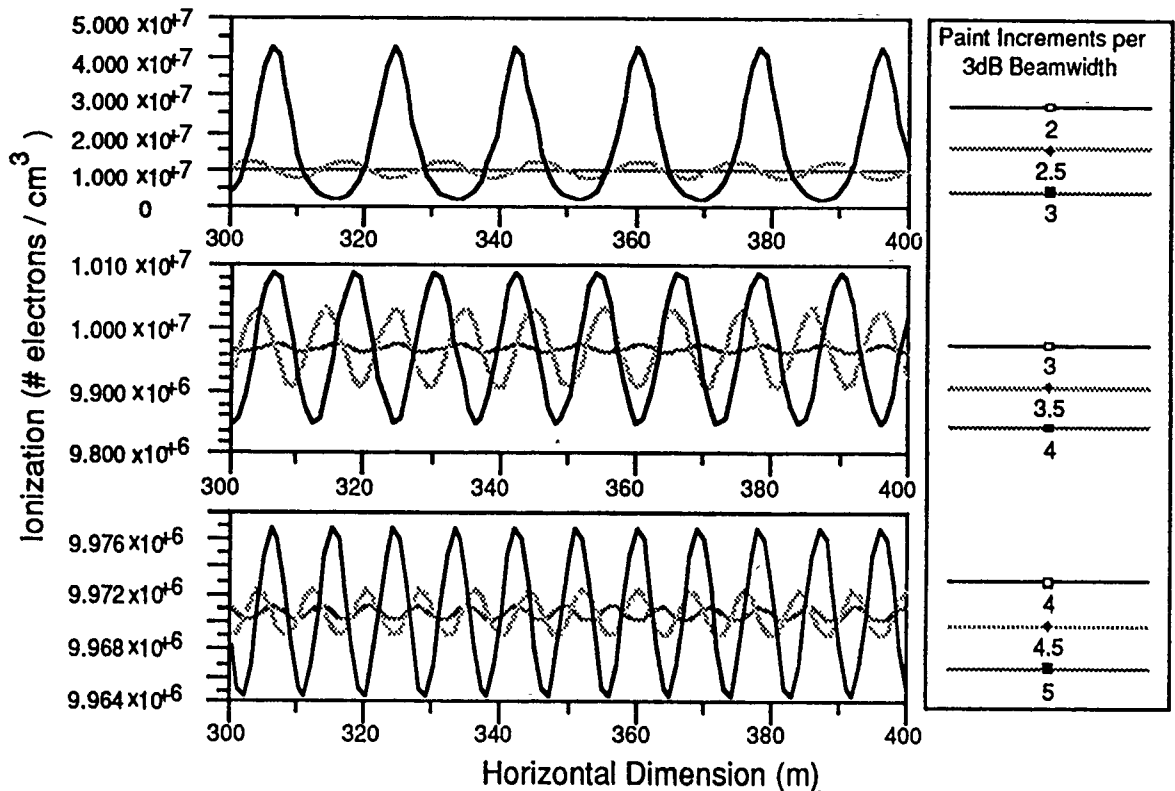


Figure 4.27. Numerical Simulation Of Electron Density Fluctuations Due to Step Scanning

the $\xi$ contour, for which significant ionization occurs. Using the resulting coefficients and substituting the relevant heater parameters into (4.39) provides a quantitative expression for trading off the heater step size against the resulting level of electron density fluctuation.

This relative fluctuation can be translated into a corresponding location perturbation. When the fluctuations are small scale, perturbations are approximately linear. Therefore, the location perturbation is related to the density gradient by

98

$$\delta z = \left(\frac{\partial N_e}{\partial z}\right)^{-1} \cdot \delta_E \cdot N_{e,ave} \qquad (4.40)$$

For a linear gradient with depth $L$, (4.40) is bounded by $\delta z < L \cdot \delta_E$. Figure 4.29 shows the quantitative tradeoff between the heater's scanning step size and the resulting electron density fluctuation and corresponding altitude fluctuation for the heater parameters given above. As this plot indicates, the density fluctuation drops dramatically as the scan step size decreases below the half beamwidth size. For a $\frac{1}{4}$ beam increment, density fluctuations are less than .1%, with corresponding location errors less than .1 meter.
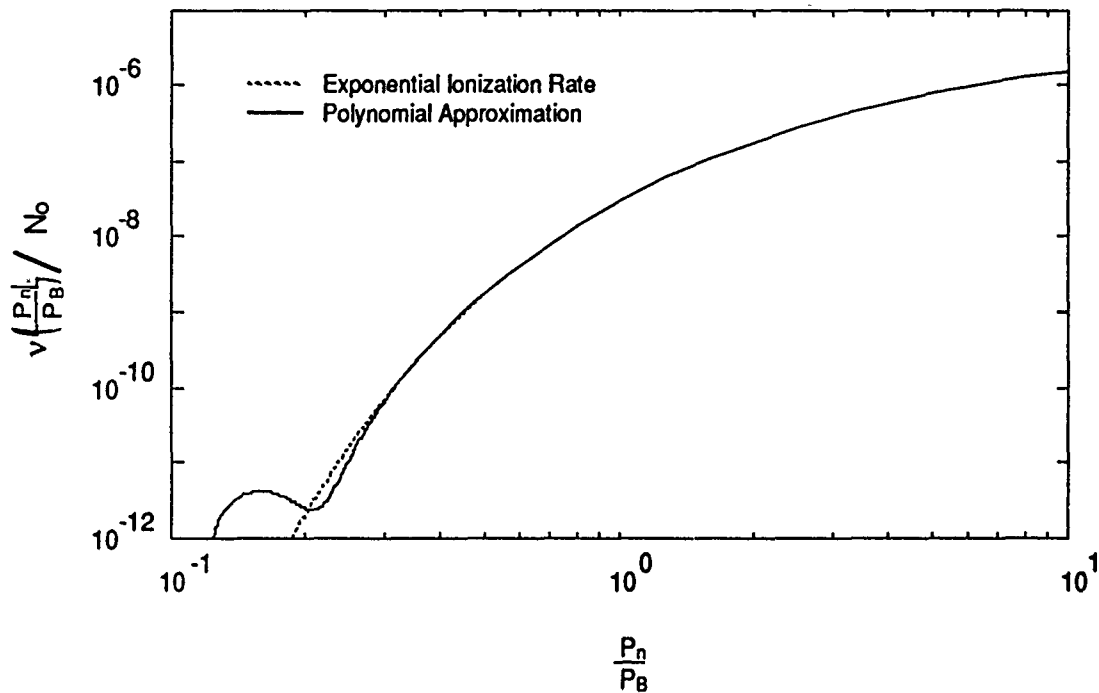


Figure 4.28. Polynomial Approximation to Ionization Rate
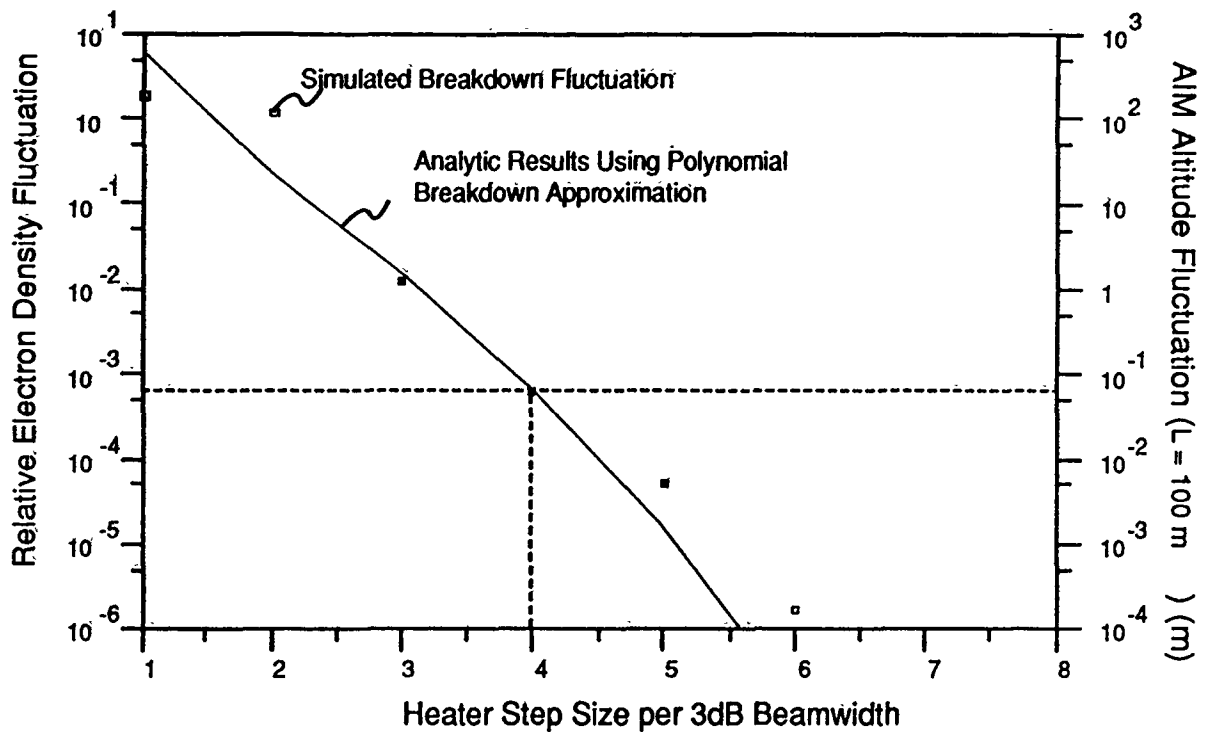
Figure 4.29. Electron Density Fluctuations Versus Heater Step Size

## 4.3.3 Results of Two-Dimensional Simulation

In this section we display some results from the 2-D plasma formation code. The two graphs shown substantiate the results of the analytic study of the previous section. In the first run, with the results shown in Figure 4.30, the heater sends pulses of length $\tau = 10$ $\mu$sec and scans to the right by 1/2 of a half-power beamwidth at each step. The result is a broken, jagged surface as described by Figure 4.30.
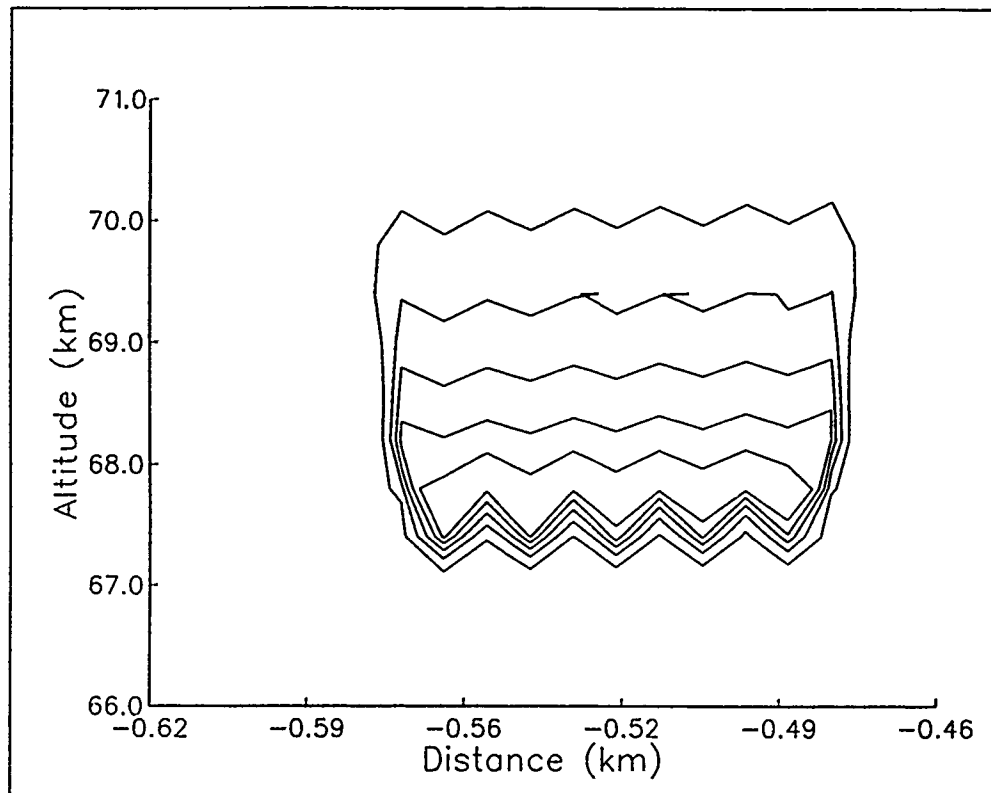
Figure 4.30. Scanning in 1/2 Beamwidth Steps, $\tau = 10$ μsec

In the Figure 4.31 the same heater now sends pulses of length $\tau = 5$ μsec and scans to the right by 1/4 of a half-power beamwidth at each step. The reader will note that total energy expended has not changed from the first run. Also a slight frequency chirp (see section 4.2.3) is used in increase the altitude of the cloud as the heater scans horizontally.
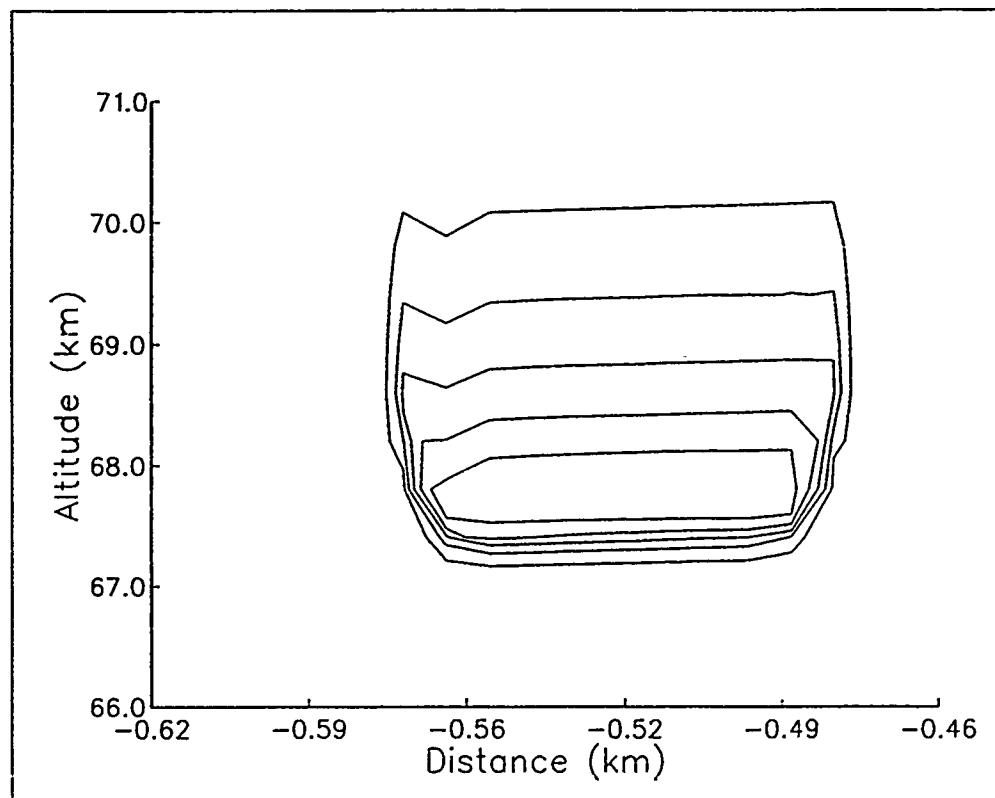
Figure 4.31. Scanning in 1/4 Beamwidth Steps, $\tau = 5$ μsec

## 4.4 Conclusion

This section described APTI's research in the formation, maintenance and control of AIM. Several tools used in this part of the project were the one-dimensional plasma formation code, its two-dimensional extension, and the microwave heater simulation used in section 4.2. The need to use near-field focusing to achieve a workable AIM cloud to be used as a coherent reflector was demonstrated. With the help of these simulations, APTI has chosen the AIM baseline heater as the starting point for future research. The simulations show that this design is a good candidate for an AIM heater and that the AIM formation time (5 μsec pulses, 1/4 half-power beamwidths apart) is consistent with AIM System Timing Diagram presented in Section 1.

# 5.0 AIM CHARACTERISTICS AND PROPAGATION EFFECTS

The reflective properties of artificially generated plasmas are of critical importance to the performance and feasibility of an AIM based system. In this section we examine the most important propagation effects and the techniques used for modeling them. We begin with a qualitative description of the reflection process.

## 5.1 The Reflection Process

Consider a region of plasma with a boundary as shown in Figure 5.1 below, with an incident electromagnetic signal being refracted by the plasma.
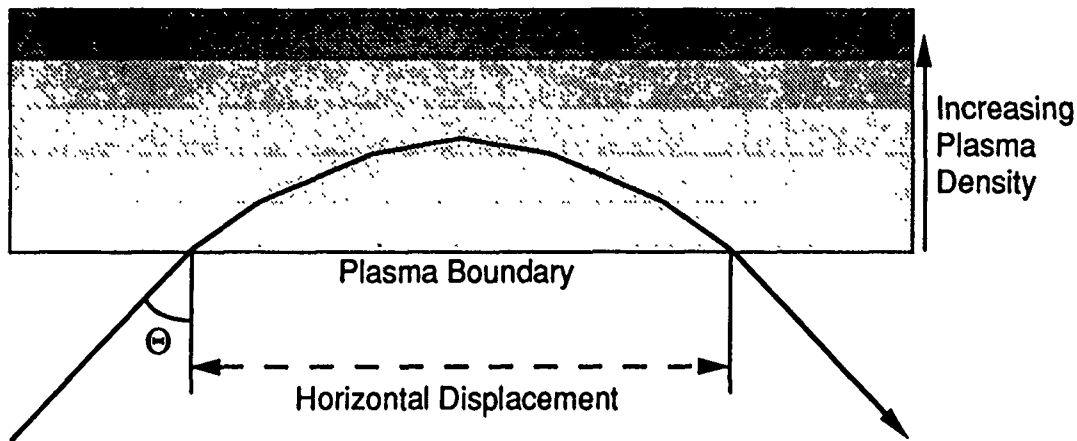


Figure 5.1. Reflection of a Ray by a Plasma

The incident electromagnetic wave is modeled in this simple conceptualization as a single ray; as long as the size and depth of the patch are much greater than the RF wavelength, this approach is quite accurate. The ray penetrates the plasma, undergoing refraction, until it reaches the turning point, at which:

$$\omega_p = \omega \cos \theta \qquad (5.1)$$

Above the turning point, only an evanescent wave exists.

The refraction process alters the signal in several ways. The most important of these are the loss of power due to absorption, the alteration of the wave polarization due to Faraday rotation, Doppler effects due to motion of the ionized region, and loss of phase coherence due to variations in position or inhomogeneities of the ionized region. Frequency

dispersion is expected to be insignificant compared to the effects above, because the total transit time of the signal through the plasma is small.

The magnitude of each of these effects depends on the physical properties of the plasma region. Depending on the depth to which the signal penetrates, the vertical plasma density profile, and the ratio $v_m/\omega$, the signal will suffer a certain degree of power loss. The polarization rotation experienced by the signal is determined by the penetration depth, the profile shape, and the ratio of the electron cyclotron frequency to the wave frequency $\omega_c/\omega$. The phase of the exiting signal is affected by the properties of the plasma region over the entire distance which the ray traverses within the plasma. The effects of random density perturbations are thus averaged over the path length. This integration over a relatively long distance (typically hundreds of meters) causes the reflective properties of the plasma region to be much less sensitive to small-scale irregularities than a hard-surfaced reflector.

## 5.2 Patch Size

The size of the patch which may be created is an important determinant of the utility of an AIM system. To act as a coherent reflector at HF and VHF frequencies, patch dimensions in the range of 200 meters to 2 kilometers are required in order to intercept and reflect adequate signal power.

The size of the ionized region is limited by the capabilities of the heater and the useful lifetime of an ionized region. If an ionized area the size of the heater focal spot may be created in time $\tau_c$, and remains useful for time $\tau_l$, then the maximum time which may be taken to form a complete reflecting region by scanning the heater focal spot is $\tau_l$, and the complete ionized region must consist of $\tau_l/\tau_c$ or fewer individual spots.

A lower bound on the size of the patch is imposed by heating of the patch electrons by the RF signal. This increases the electron-neutral collision frequency, resulting in increased absorption. For a given RF signal power, a larger patch area delays the onset of this effect, which is described in more detail in the section on absorption below.

## 5.3 Patch Lifetime

The time of utility of the AIM cloud is controlled by two physical considerations. The first of these is the cooling rate of the electrons following formation of the cloud. The reason for this is that the absorption of the incident signal is high for energetic electron dis-

104

tributions such as those produced during the formation of AIM clouds. Following the cutoff of the heater pulse, the electron distribution relaxes rapidly to a lower energy. Cooling rate estimates, based on kinetic simulations of the cooling process, are of the order of $10^{-4}$ seconds. The useful life of the AIM cloud starts following the electron relaxation, since at this point the fractional absorption of the signal is minimized. A more detailed discussion of the cooling process is given in section 5.4.2 below.

The end of the useful lifetime of the patch is controlled by either local decay processes or by transport process. Because the precise location of the patch (within 100-200 meters) is not important in most cases, transport processes such as winds which do not alter the shape or orientation of the patch do not affect its useful lifetime. The effects of wind shear and turbulence are briefly discussed in sections 5.4.2 and 5.4.3, respectively; they are generally not the limiting factors in patch lifetime. Of the remaining transport processes, the most important is diffusion, which is very slow because it is ambipolar. For the range of altitudes under consideration (60-80 km.) the dominant factor in determining the useful lifetime of a patch is the rate of decay due to local processes.

The three most important local decay processes are recombination, 3-body attachment to oxygen, and 2-body attachment to oxygen. Because of the very low fractional ionization, recombination operates on time scales of 1-10 seconds or longer. Three-body attachment is also very slow in the altitude range in question. The dominant decay process for AIM systems between 60 and 80 km. altitude is 2-body attachment to oxygen. Because the cross-section for attachment peaks at 7-8 eV, attachment proceeds rapidly until the electron population has cooled. After this, the rate of decay due to attachment is slower. Preliminary studies employing a kinetic simulation indicate that the useful lifetime of a patch in the altitude range of interest is between .1 and 1 seconds.

## 5.4  Absorption

Absorption is determined by the electron-neutral collision frequency $v_m$, and the distance which a ray travels within the plasma. This distance, in turn, is determined by the signal frequency and the way in which the plasma density varies with distance as the signal passes deeper into the patch.

An intuitive appreciation of the importance of these factors in determining absorption may be gained by examining an analytic result for the power absorption in decibels of a patch whose plasma density varies linearly with distance into the patch, until $\omega_p = \omega$ at a depth $L$:

$$A_{dB} = 3.64 \cos^3\theta \, \frac{L}{\lambda} \frac{v_m}{\omega}$$

(5.2)

Here $\theta$ is the angle of incidence, typically 35-45°. Although a linear plasma density variation is not typical of those produced by AIM heaters, this expression is useful for the qualitative insight it provides. Since $\theta$ is fixed by the geometry, the absorption is determined by $L/\lambda$ and $v_m/\omega$; if their product is small, the overall absorption will be small. For a given RF signal frequency, the minimum value of $v_m/\omega$ is determined by the ambient collision frequency, and $L/\lambda$ is determined by the the vertical electric field profile generated by the heater system.

### 5.4.1 Numerical Calculations of Absorption

In evaluating the performance of an AIM system, it is necessary to calculate the absorption of the plasma density profiles which are produced by simulations of the patch formation process. This requires a method capable of accepting an arbitrary plasma profile; the two methods employed were ray tracing and finite-difference full wave calculation. Both of these methods were implemented in computer simulations; a ray-tracing absorption calculation is incorporated in the system simulation described in section 6.

### 5.4.1.1 Ray Tracing

Ray tracing methods are derived from Fermat's principle, which requires that the path followed by a ray through a medium is such that the transit time associated with that path is stationary with respect to small variations in the ray path. The equations of the ray path are:

$$\frac{d\mathbf{n}}{dt} = \frac{c}{n} \frac{\partial n}{\partial \mathbf{r}}$$

(5.3)

$$\frac{d\mathbf{r}}{dt} = \frac{c\mathbf{n}}{n^2}$$

(5.4)

where

$\mathbf{n}$ = the refractive index vector, whose magnitude is equal to the scalar refractive index $n$, and

106

r = the location of the tip of the ray.

The ray equations may be solved by numerical integration given a function $n(x,y,z)$. For an isotropic plasma of plasma frequency $\omega_p$ and an incident wave of frequency $\omega$:

$$n = \sqrt{1 - \left(\frac{\omega_p^2}{\omega^2 + v_m^2}\right)} \tag{5.5}$$

This method of solution is known as real-valued ray tracing, and is valid when the imaginary part of the complex refractive index

$$\tilde{n} = \sqrt{1 - \left(\frac{\omega_p^2}{\omega^2 + v_m^2}\right)\left(1 + j\frac{v_m}{\omega}\right)} \tag{5.6}$$

is small, that is, when $v_m/\omega$ is small. (An alternative technique, complex ray tracing, is used when $v_m/\omega$ is large.) Subject to this condition, the losses suffered by a ray on reflection may be calculated by simultaneously integrating the loss equation:

$$\frac{d}{dt}(\ln E) = -\omega \frac{Im(\tilde{n})}{Re(\tilde{n})} \tag{5.7}$$

### 5.4.1.2 Finite-Difference Full-Wave Methods

Finite difference methods are conceptually the simplest approaches to numerical solution of partial differential equations such as the electromagnetic wave equation:

$$\nabla^2 \mathbf{E} - \mu\varepsilon \frac{\partial^2 \mathbf{E}}{\partial t^2} - \mu\sigma \frac{\partial \mathbf{E}}{\partial t} = 0 \tag{5.8}$$

For an isotropic plasma, the constitutive parameters are:

$$\varepsilon = \varepsilon_0 \left(1 - \frac{\omega_p^2}{\omega^2 + v_m^2}\right) \tag{5.9}$$

$$\sigma = \varepsilon_0 v_m \left(\frac{\omega_p^2}{\omega^2 + v_m^2}\right) \tag{5.10}$$

$$\mu = \mu_0 \tag{5.11}$$

Finite difference methods calculate solutions of the difference equation corresponding to the above wave equation:

$$\left(\delta_x^2 + \delta_y^2 + \delta_z^2\right)E_i - \mu\varepsilon\frac{\Delta^2}{\Delta_t^2}\delta_t^2 E_i - \mu\sigma\frac{\Delta^2}{\Delta_t}\delta_t E_i = 0 \qquad (5.12)$$

where;

$E_i$ = any component of the E-field vector **E**

$\Delta$ = spatial grid step size

$\Delta_t$ = time step size

and the difference operators are defined by:

$$\delta_x^2\left(E_i(x,y,z,t)\right) = E_i(x+\Delta,y,z,t) - 2E_i(x,y,z,t) + E_i(x-\Delta,y,z,t)$$
$$\delta_y^2\left(E_i(x,y,z,t)\right) = E_i(x,y+\Delta,z,t) - 2E_i(x,y,z,t) + E_i(x,y-\Delta,z,t)$$
$$\delta_z^2\left(E_i(x,y,z,t)\right) = E_i(x,y,z+\Delta,t) - 2E_i(x,y,z,t) + E_i(x,y,z-\Delta,t)$$
$$\delta_t^2\left(E_i(x,y,z,t)\right) = E_i(x,y,z,t+\Delta_t) - 2E_i(x,y,z,t) + E_i(x,y,z,t-\Delta_t)$$
$$\delta_t\left(E_i(x,y,z,t)\right) = E_i(x,y,z,t) - E_i(x,y,z,t-\Delta_t)$$

This can be rearranged to give an expression for $E_i(x,y,z,t+\Delta_t)$ in terms of current and previous values of $E_i$ at $(x,y,z)$ and adjacent points. In this case, the equation is:

$$E_i(t+\Delta_t) = \frac{\Delta_t^2}{\mu\varepsilon\Delta^2}\left(\delta_x^2 + \delta_y^2 + \delta_z^2\right)E_i(t) + \left(2 + \frac{\sigma}{\varepsilon}\Delta_t\right)E_i(t) - \left(1 + \frac{\sigma}{\varepsilon}\Delta_t\right)E_i(t-\Delta_t) \qquad (5.13)$$

The above form of the wave equation is used to calculate the losses caused by reflection. This approach is an explicit finite difference method for solution of the differential equation above. For the solution to the difference equation to converge to the solution of the matching differential equation, the Courant-Friedrichs-Lewy (CFL) condition must be satisfied over the entire grid:

$$\frac{1}{\sqrt{N}} \geq \frac{\Delta_t^2}{\mu\varepsilon\Delta^2} \qquad (5.14)$$

where N is the number of dimensions. In addition, minimum values of $\Delta$ are influenced by the shortest wavelength present in the incident signal; generally $\Delta$ must be at least an order of magnitude smaller than the shortest wavelength. A satisfactory value of $\Delta_t$ may then be determined from the equation above.

### 5.4.1.3 Selection of Method

The results of the two techniques described above have been compared for a wide variety of plasma parameters. Because ray tracing requires much less computational effort, it has been employed wherever possible, that is, wherever the ray approximation is valid. It has thus been used for all absorption calculations, with a full-wave simulation used as a check. The techniques described above have also been applied to the analysis of other propagation phenomena, notably in examining the effects of irregularities. The results of these studies are described in the sections below.

### 5.4.2 Factors Affecting $v_m$

Immediately after the patch is created, the electron-neutral collision frequency $v_m$ is very high. The energetic electrons in the patch rapidly transfer their energy to the neutral atmosphere by first exciting optical lines, and subsequently vibrational and rotational resonances, and the collision frequency quickly returns to its ambient value. The ambient value, which is the lowest possible collision frequency at a given altitude, is shown in figure 5.2.
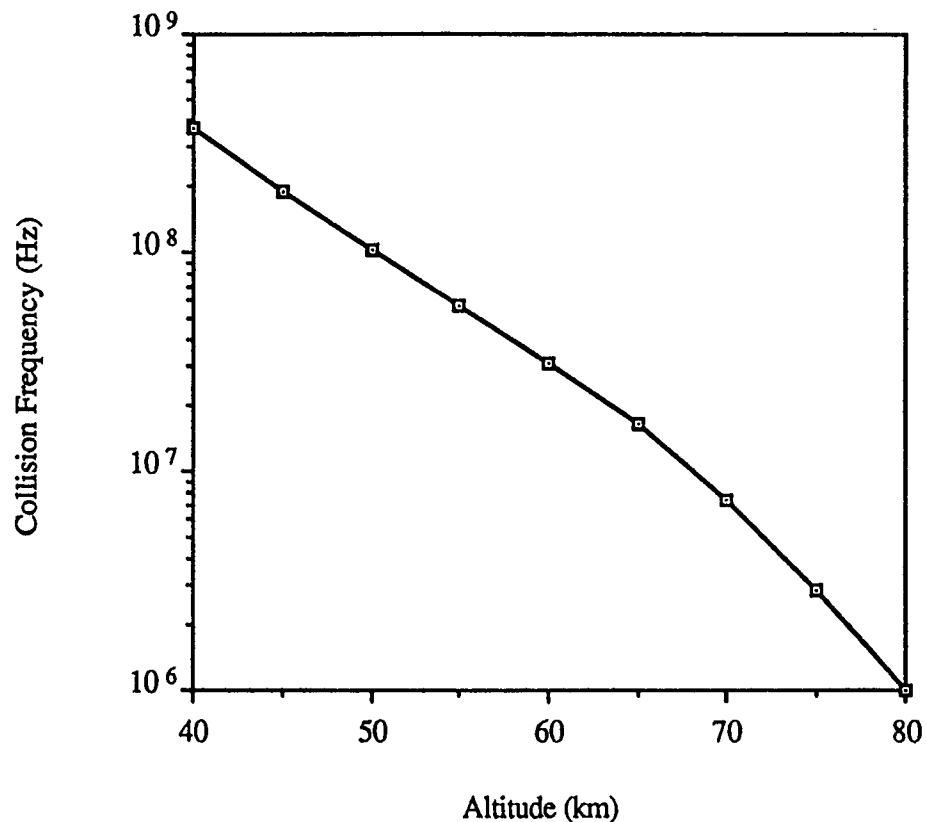
Figure 5.2. Ambient Electron-Neutral Collision Frequencies.

The ambient collision frequencies shown in Figure 5.2 represent an important restriction on the altitude of the patch for practical AIM systems. For example, if we require that $v_m/\omega$ be less than .1, we can see that a 50 MHz system is restricted to patch altitudes above 60 kilometers.

The time required for the patch to cool after formation also varies with altitude. Figure 5.3 below shows the time required to cool so that $v_m$ is within a factor of 2 of its ambient value as a function of altitude. Because the fractional ionization is very low, the cooling does not result in any significant change in the neutral temperature. Note that in terms of the usable lifetime of a patch, which is expected to be of the order of 100 milliseconds, the cooling times are quite short.
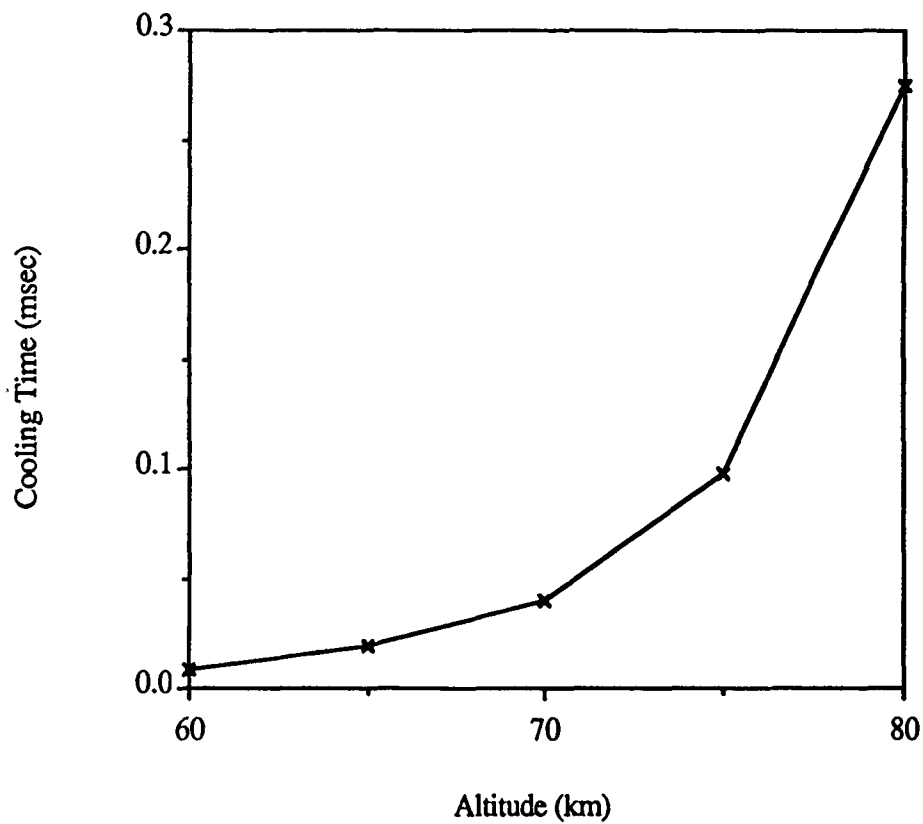
Figure 5.3. Cooling Time Variations with Altitude.

As mentioned above, the cooled plasma may be reheated by the incident wave if its power density is high enough. The time required for reheating is of the order of $10^{-3}$ seconds, and becomes shorter as the incident power is increased, so the use of short pulses to avoid this effect is limited. Figure 5.4 shows the ratio of $v_m$ after heating to the ambient value, for a frequency of 50 MHz and a patch altitude of 70 kilometers.
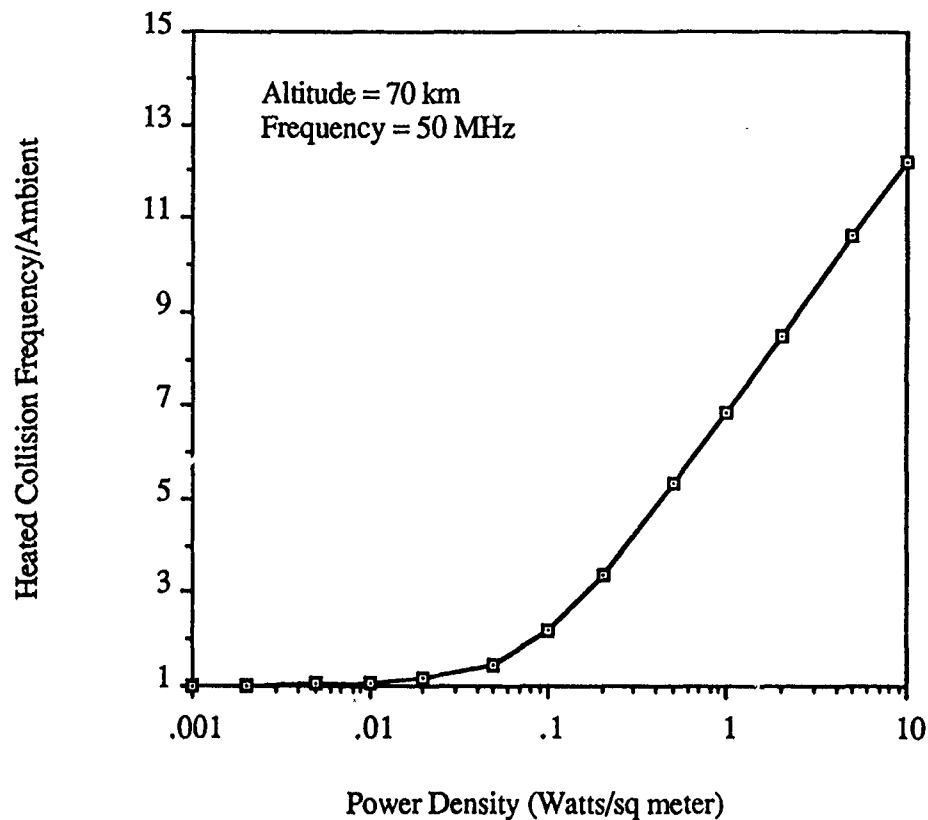
Figure 5.4. Ratio of Heated $v_m$ to Ambient

Patch heating imposes an upper limit on the signal power density at the patch. As the signal power density exceeds the threshold level for heating (about 0.1 W/m² in the example above), the relationship between incident and reflected power becomes nonlinear. At some point, a maximum is reached, where additional power input causes additional absorption sufficient to cancel the power increase. Above this, additional incident power actually causes the reflected power to decrease. This limiting effect is shown in Figure 5.5.
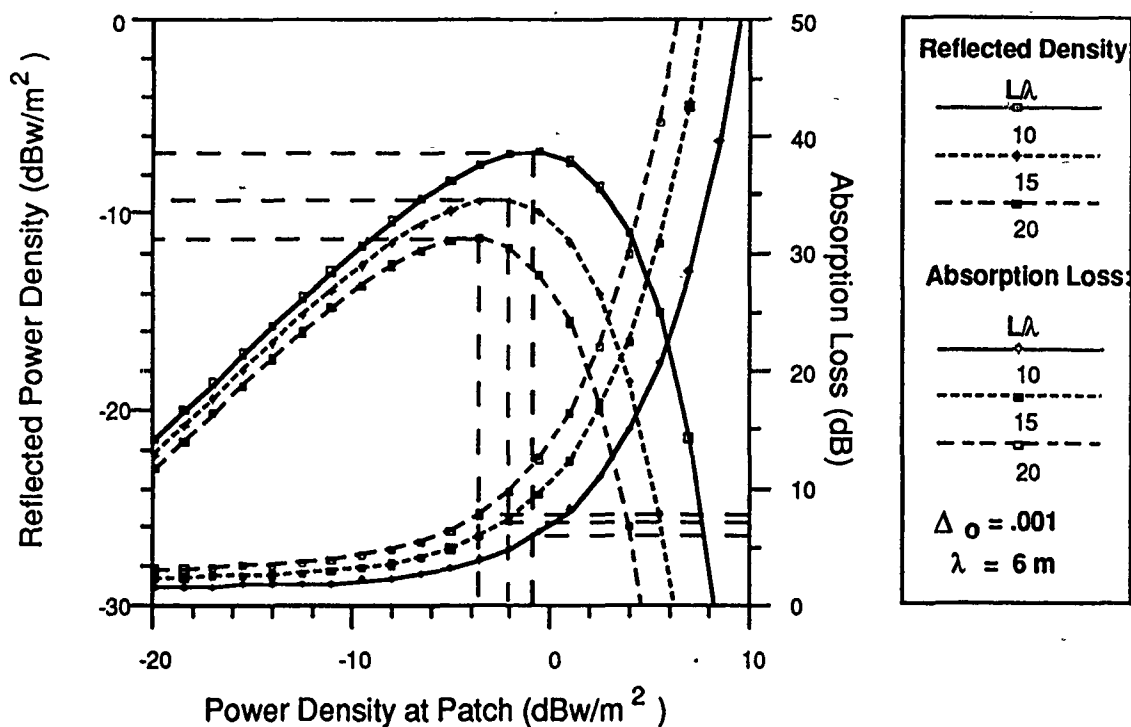
Figure 5.5. Self-Limiting of Reflected Power by Patch Heating

## 5.4.3 Summary of Absorption Effects

The necessity to minimize signal absorption imposes constraints on both the heater and the signal power. The heater system must be capable of producing regions of ionization whose "depth", that is, the distance over which the plasma frequency changes from ambient to a sufficient level to reflect the incident wave, is short. Typically, the patch depth is restricted to less than 20-30 signal wavelengths, and patches must be created at altitudes such that $v_m/\omega < 0.1$. Creation of these patches requires a focusing heater. Patch absorption places an upper limit on incident power density. The increase in absorption with patch depth also restricts the use of deeper patches to reduce sensitivity to irregularities, as will be discussed in section 5.6.

## 5.5 Doppler Effects

Three major causes of frequency-domain signal modifications have been identified: patch motion, wind shear, and turbulence. It is important to note that all three of these effects are driven by motions of the neutral atmosphere; because of the very low fractional ionization, $10^{-3}$ or less, and the relatively high neutral density, plasma oscillations are expected to be very heavily damped and have negligible effect on the reflected signal.

### 5.5.1 Patch Motion

As soon as it is created, the ionized region will move with the neutral atmosphere in which it is embedded. This motion will cause a doppler shift in the signal reflected from the patch. It is not anticipated that uniform motion of the patch as a whole, regardless of the wind speed, will degrade the performance of an AIM system.

### 5.5.2 Wind Shear

If a wind shear exists at the point where the patch is created, the patch will not only move, but be altered in orientation and shape. Because vertical shear is generally much more severe than horizontal shear, it is expected to be the dominant source of shear-induced doppler effects. The vertical extent of the patch is typically 300-600 meters; at altitudes of 70 kilometers, vertical shears of as much as 0.05-0.07 $sec^{-1}$ are known to exist. (This figure represents the 1% probability maximum shear at Cape Canaveral, from [Jursa, 1985].)

This worst-case situation represents a wind velocity change of 15-40 m/s over the vertical extent of the patch, which corresponds to a rotation of 0.7-3.6 degrees per second. This will cause a change in the direction of the reflected beam of 1.4-7.2 degrees per second. Although this has an insignificant effect on the pointing of the beam, since patch lifetimes are of the order of 0.1 second, it does impose a scanning modulation on the signal given by

$$\sigma_f = 0.265 \frac{\varphi_{scan}}{\phi} \qquad (5.15)$$

where $\sigma_f$ is the frequency deviation of the power spectrum in Hertz, $\varphi_{scan}$ is the scanning rate in degrees per second, and $\phi$ is the beamwidth in degrees. The maximum frequency spread for the example system discussed above, for which $\phi_v = 12°$, is 0.16 Hz. This frequency deviation corresponds to a velocity deviation of

$$\sigma_v = \frac{c \, \sigma_f}{2 f} \qquad (5.16)$$

which for our example equals 0.48 meters per second. In general, the impact of shear induced scanning modulation is expected to be slight.

## 5.5.3 Turbulence

Little information is available on the existence or characteristics of turbulence at altitudes of 50-100 kilometers. If turbulence occurs, it may be possible to avoid it by adjusting the altitude of the AIM patch.

## 5.6 Faraday Rotation

Depending on the geographical location and orientation of the patch, the geomagnetic field will cause some amount of Faraday rotation of the polarization of the reflected signal.

In modeling Faraday rotation, it is necessary to employ a vector wave equation to determine the change in the polarization of the incident wave. The approach selected follows that of [Budden, 1985], i.e. the calculation of the reflection coefficient rather than the electric field vector to avoid singularities at the reflection point.

In this approach, a vacuum reflection coefficient matrix $\mathbf{R}$ is defined to be:

$$\begin{bmatrix} E_{HI} \\ E_{VI} \end{bmatrix} = \mathbf{R} \begin{bmatrix} E_{HR} \\ E_{VR} \end{bmatrix} \tag{5.17}$$

Where $E_H$ and $E_V$ are the equivalent vacuum fields at the point where $\mathbf{R}$ is evaluated, and the I and R subscripts indicate incident and reflected waves. The $\mathbf{R}$ matrix indicates the degree to which horizontally polarized incident waves are transformed into vertically polarized reflected waves, and vertically polarized incident are transformed into horizontally polarized reflected, by Faraday rotation. A complex matrix differential equation for $\mathbf{R}$ in terms of altitude may be derived [Budden, 1985]:

$$2j \frac{\partial \mathbf{R}}{\partial z} = w_{21} + w_{22} \mathbf{R} - \mathbf{R} w_{11} - \mathbf{R} w_{12} \mathbf{R} \tag{5.18}$$

where the w's are matrix functions of the plasma properties at that altitude and the intensity and orientation of the magnetic field. This set of equations may be solved using any of the various approaches for ordinary differential equations; in this case, an adaptive altitude step Runge-Kutta method was used.

Results of this calculation show the expected geographical variation in the amount of rotation, due to the geographical changes in the direction and strength of the geomagnetic

field. Rotation is minimized regardless of location if the transition from ambient to maximum plasma density is made in as small a distance as possible, which also reduces the absorption of the signal due to reflection from the plasma.

Computations using typical profiles produced by simulations of the plasma formation process show rotations of as much as 2-3 radians for the worst-case location and patch orientation. In these cases, it may be necessary to precompensate for Faraday rotation by adjusting the polarization of the transmitted signal. Because the amount of rotation depends only on the depth, location, and orientation of the patch, the amount of compensation required can be computed or determined by experiment and applied each time a patch is created.

## 5.7 Irregularities

Random errors during the patch formation process may result in patches which have small-scale departures from the desired shape. The causes of these errors and their expected magnitude are discussed in section 4. In this section, we examine the impact of random positional errors on a radar system.

In order to assess the impact of errors on the ultimate performance of the AIM radar, we first derive the relationship between rms patch irregularity and the resulting reduction in effective patch gain. Figure 5.6 illustrates the relevant two dimensional geometry and associated parameters for the AIM cloud.
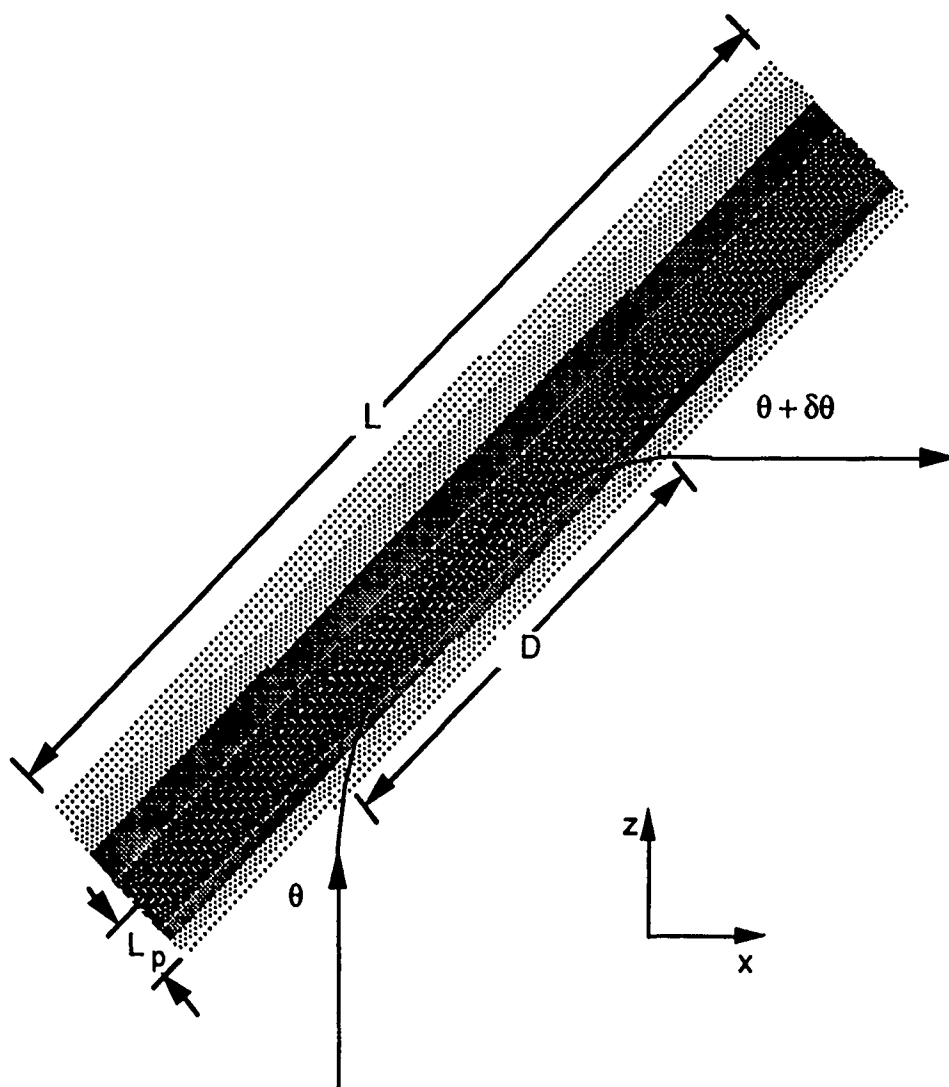
Figure 5.6. AIM Cloud Geometry

Using the ray path model indicated in Figure 5.6, the direction of the exiting ray, $\eta(x,z)$ is related to the spatial phase gradient, $-\nabla\phi(x,z)$, of the propagating wave by

$$\eta(x,z) = \frac{-\nabla\phi(x,z)}{k} \qquad (5.19)$$

where $k = 2\pi/\lambda$ is the wave number. The unit vector in (5.19), which is locally orthogonal to the surface of constant phase, is given by the direction of the ray leaving the plasma,

$$\eta(x,z) = \begin{bmatrix} sin(2\theta + \delta\theta(x,z)) \\ cos(2\theta + \delta\theta(x,z)) \end{bmatrix} \tag{5.20}$$

At any given point in time, the relative phase of the exiting wave at the plasma surface can be found by integrating the phase gradient projected along the direction parallel to the plasma surface. In terms of the parameters indicated in Figure 5.6, the relative phase along the AIM surface is

$$\begin{aligned} \phi(l) &= \phi(l\,sin\,\theta,\,l\,cos\,\theta) \\ &= \phi_0 - k\int_D^l cos\big(\theta + \delta\theta(u\,sin\,\theta,\,u\,cos\,\theta)\big)\,du \\ &\approx \phi_0 - k(l-D)cos\,\theta + k\,sin\,\theta\left(\int_D^l \delta\theta(u\,sin\,\theta,\,u\,cos\,\theta)\,du\right) \end{aligned} \tag{5.21}$$

where

$l$ = the distance along the AIM surface (in the plane of inclination) and

$D$ = the distance from the point of entry to the point of exit, for the unperturbed plasma. For a linear plasma profile, D. Mosher [Mosher, 1988] has shown that

$$D = 4L_p\,cot\,\theta \tag{5.22}$$

where $L_p$ is the patch depth (distance from the ambient electron density to a plasma frequency equal to the signal frequency). In the case of the linear electron density profile, Mosher also shows that the direction of the exiting wave front is related to the positional perturbations of the AIM profile by

$$\delta\theta(l\,sin\,\theta,\,l\,cos\,\theta) = \frac{1}{2\,L_p\,cot\,\theta}[\varepsilon(l) - \varepsilon(l-D)] \tag{5.23}$$

where $\varepsilon(l)$ is the position perturbation relative to the ideal AIM profile, orthogonal to the AIM surface. For the purposes of our analysis, we assume that $\varepsilon$ position errors are on the same order as $\Delta z$, thus using the approximation $\varepsilon(l) = \Delta z(l)$.

The reduction in effective gain off of the AIM surface due to the wave front perturbations is given by the integration of the electric field at the plasma surface, which can be reduced to

$$L(\theta) = \frac{1}{(L-D)^2} \left| \int_D^L e^{j(\phi(l) - k(L-l)\cos\theta)} \, dl \right|^2 \qquad (5.24)$$

where $L$ is the length of the AIM surface, the phase term is compensated relative to the far-field path length in the direction of the maximum gain, and integration is performed over the extent of the AIM surface associated with an exiting wave front. Substituting equation (5.21) into (5.24) and simplifying gives

$$L(\theta) = \frac{1}{(L-D)^2} \left| \int_D^L e^{j\delta\phi(l)} \, dl \right|^2 \qquad (5.25)$$

where

$$\delta\phi(l) = k \sin\theta \cdot \int_D^l \delta\theta(u \sin\theta, u \cos\theta) \cdot du \qquad (5.26)$$

Since $L(\theta)$ is a function of $\Delta z(l)$ and $\Delta z$ has been modelled as a random perturbation, the $L(\theta)$ is best characterized through its statistical moments. The first order moment is found by taking the expected value as follows:

$$E\{L(\theta)\} = \frac{1}{(L-D)^2} \int_D^L\!\!\int E\left\{e^{j(\delta\phi(u) - \delta\phi(v))}\right\} du \, dv$$

$$(5.27)$$

$$= \frac{1}{(L-D)^2} \int_D^L\!\!\int e^{-\frac{1}{2}R_\phi(u,v)} du \, dv$$

where

119

$$\frac{1}{2} R_\phi(u,v) \quad = E\left\{\left|\delta\phi(u) - \delta\phi(v)\right|^2\right\}$$

(5.28)

$$= \frac{k^2 \sin^2\theta \, D}{2 \, L_p^2 \cot^2\theta} \int_{-D}^{D} (1 - \frac{\tau}{D}) \{R_e(\tau) - R_e((u-v) + \tau)\} \, dt$$

In (5.28), $R_e(t)$ is the autocorrelation function of $\varepsilon(l)$, or in our case of $\Delta z(l)$.

Therefore, given a statistical model for the AIM positional errors, the impact of these errors can be related to a corresponding reduction in the unperturbed patch gain. This gain 'loss' can subsequently be expressed in terms of its impact on the overall radar detection performance.

A second loss factor related to propagation of the incident wave through the AIM cloud is the the absorption of signal energy in the cloud due to electron-neutral collisions, as described in section 5.3 above. For a linear density profile, this loss mechanism can be expressed analytically [Case and Sprangle, 1988]

$$L_A = e^{-\frac{8\pi}{3}\left(\frac{L_P}{\lambda}\right)\left(\frac{V_m}{\omega}\right)\cos^3\theta}$$

(5.29)

where $v_m$ is the electron-neutral collision frequency, $\omega$ is the radar radian frequency, and $\lambda$ is the radar wavelength.

In order to assess the overall impact of AIM related losses on the system performance, the dispersion factor, (5.27), and absorption factor, (5.29), are multiplied to obtain a combined one-way AIM loss factor. In considering the two components of this combined loss, we see that as the patch depth, $L_p$, is increased the dispersion loss decreases (due to increased averaging), while the absorption loss increases. This phenomenon introduces a trade-off between the two competing loss mechanisms, resulting in an optimal AIM density gradient for a given set of heater/radar design parameters.

In order to assess the impact that density fluctuations will have on radar performance, the equivalent distortions in the refracted wave's phase front must be determined. Because the AIM represents a continuously increasing electron density (decreasing index of refraction), the wave is not scattered, as from an irregular hard surface, but refracts through many

signal wavelengths of fluctuating medium, resulting in phase deviations that have been significantly reduced by averaging.

Two numerical models have been developed to help quantify this effect, using the techniques described in section 5.4.1. The first model uses a geometric optics approach, by integrating through the AIM medium along refracting rays of propagation. The second model implements a two-dimensional full-wave propagation through a plane perpendicular to the patch and and the far-field wave front. Figure 5.7 shows the results of applying these models to a 50 Mhz signal refracting through a 100 m deep plasma, for a number of rms surface errors and fluctuation lengths. While the bulk of the results are due to a ray tracing model, a number of full-wave results are shown for verification. As these curves indicate, for projected plasma density gradients, smoothing due to refraction reduces the perturbation effects relative to a hard surface by a factor of 10. The .1 m fluctuation shown in Figure 5.7 translates to a 1 degree wave front variation in the refracted wave, resulting in negligible impact on patch gain and subsequent radar performance.
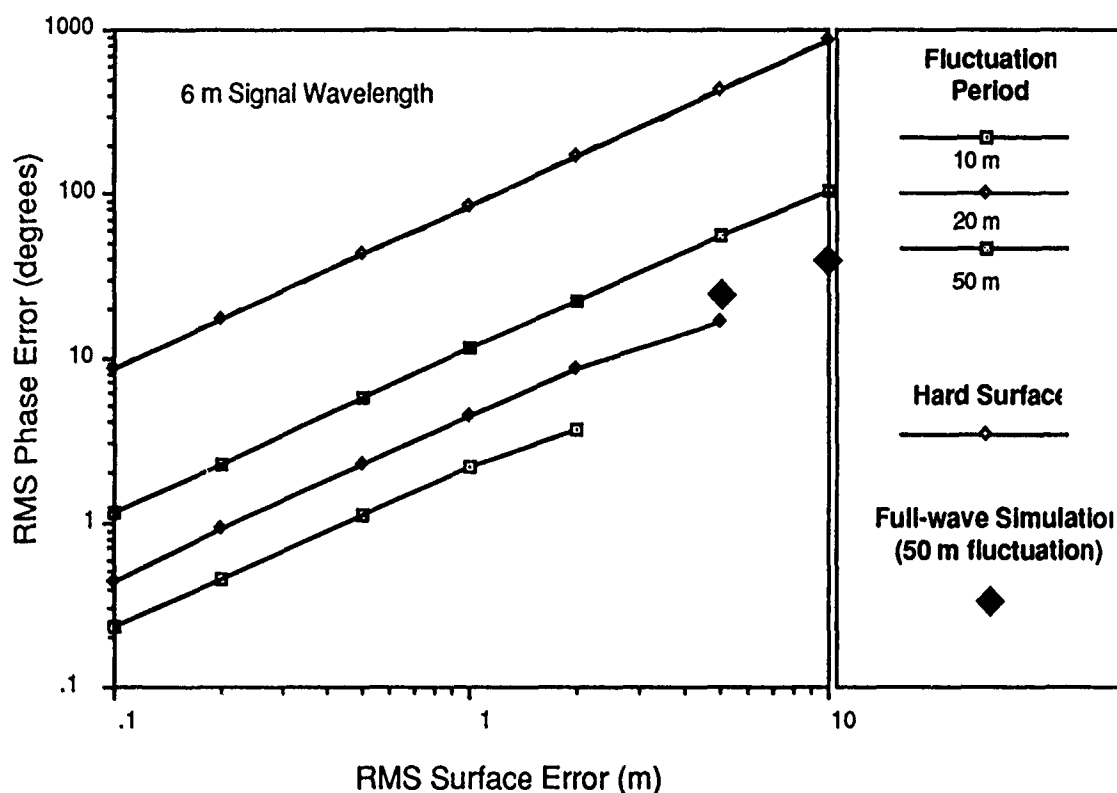


Figure 5.7. Phase Perturbations with AIM Refraction Versus a Hard Surface.

## 5.8 Conclusion

Several perturbations which propagation through a plasma mirror imposes on the signal have been identified and analyzed in detail. A few effects, notably absorption, impose constraints on the heater design.

## 6.0 OVERALL SIMULATION MODEL

As an aid to the analysis of the relationships between components of an AIM system, a model of the complete plasma formation and signal reflection process has been constructed. The model is composed of a plasma formation simulation and a propagation simulation, which together calculate the propagation effects of a patch created by a given heater design. A wide variety of candidate heater designs has been examined using the simulation, and an understanding of the range of designs which yield useful patches has been developed. Each of the components of the simulation is described in the sections below.

### 6.1 Plasma Formation Simulation

The purpose of this part of the overall AIM simulation model is to simulate the microwave breakdown of air through avalanche ionization. The simulation, known as FAIM (Formation of an Artificial Ionospheric Mirror) is used to demonstrate techniques used to control the altitude, inclination, size and gradient of the created AIM. It is an essential tool in evaluating the utility of potential heater designs for the AIM system.

### 6.1.1 Basic Algorithm

The FAIM code is a vertical one-dimensional discretized model of the atmosphere and a high-energy microwave pulse. The code begins with a discrete altitude grid, with ambient values for electron density and neutral density. A microwave pulse grid propagates upwards with time. The pulse propagates according to the formula

$$E = E_0 \exp\left( jk\sqrt{\varepsilon'}z \right) \tag{6.1}$$

where $\sqrt{\varepsilon'}$ is the complex valued dielectric constant of the atmosphere. The real part of $\sqrt{\varepsilon'}$ describes the pulse's velocity and the imaginary part describes the attenuation or absorption of the pulse by existing electrons. At each time step and at each location on the altitude grid, the physical location of the pulse is determined and the electric field is computed using the antenna array factor (which is focusing at a particular altitude) and any self-absorption that has previously occurred. The ionization and collision frequencies are computed using this electric field in the formulas mentioned above. The electron density and dielectric constant are then recomputed, and finally the self-absorption for the time step is calculated. The basic mechanics of the code are exhibited in Figure 6.1.

**On a discrete altitude grid,**

**With a high energy microwave pulse train grid
propagating upwards with time**

$\frac{1}{2}\frac{\Delta h}{c}$ = **fundamental time step**

**Compute** $v_{net}$ **using** $E$
**from pulse train**

**Adjust electron density**
$N_e = N_e \exp(\ v_{net}\ \tau)$

next time step

**Compute energy attenuation**
$E = E \exp(\ \mathrm{Im}(\sqrt{\varepsilon'})\ \tau)$

**Recompute dielectric constant**
$\varepsilon' = 1 - \dfrac{\omega_p^2 / \omega^2}{1 - j(\ v_m / \omega)}$
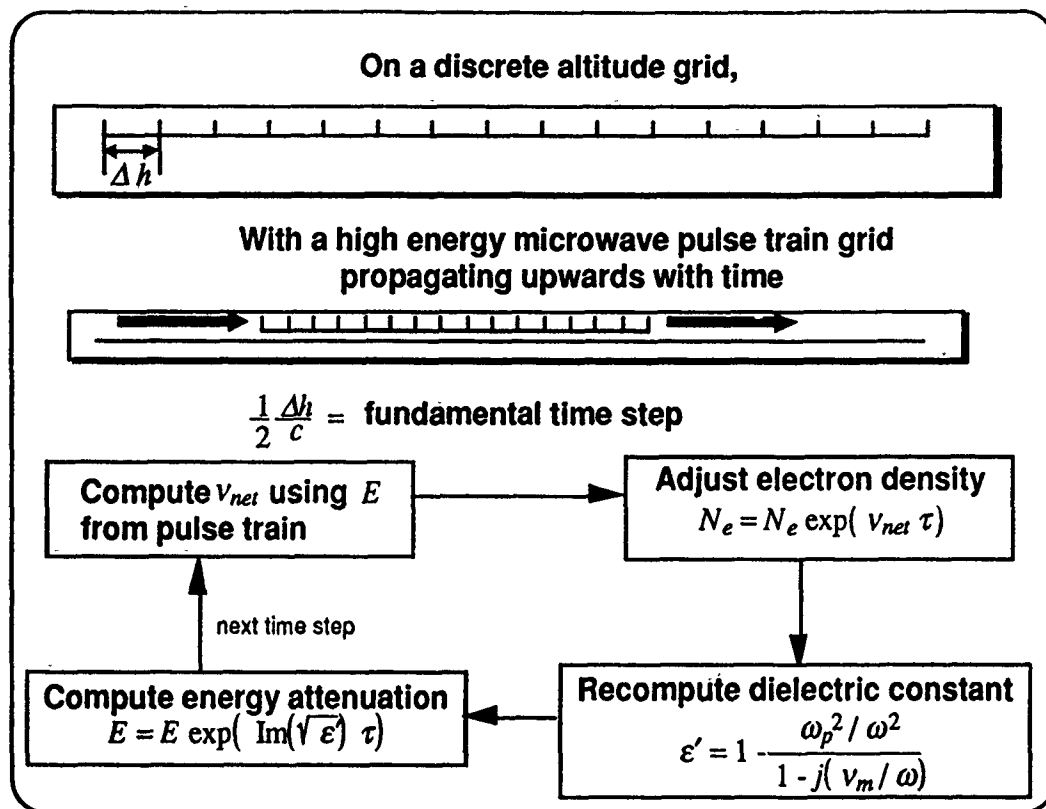
Figure 6.1. Mechanics of one-dimensional FAIM code

## 6.1.2 Heater Simulation

The heater antenna model for the overall AIM simulation must be as flexible as possible in
its range of input parameters. It must be able to model a wide array of different candidate
heater designs. The model works on the basic equation

$$S = P\ G\ \left(\frac{|A|^2}{4\pi}\right) \tag{6.2}$$

where      $S$ = power density

$P$ = transmitted power

$G$ = gain

$A$ = heater array antenna and space loss factor

The heater array antenna and space loss factor describes the antenna pattern and includes the $1/r^2$ space loss. When $|A|^2 = 1/r^2$, we are at the point of maximum electric field. The antenna and space loss factor for an unfocused array of isotropic sources is

$$A = \sum_{n=1}^{N} \frac{\exp(-jkr_n)}{r_n} \qquad (6.3)$$

where    $k = 2\pi f/c$ = frequency wave number

   $N$ = number of elements in the array.

   $r_n$ = distance from element to point of measurement

This equation represents the basic building block in the heater array simulation. A small array of isotropic sources is used to approximate the antenna pattern from a horn or a dish. In the case of a large array of horns or dishes, the sources are grouped into "sub-arrays" of smaller arrays (40 - 100 isotropic sources) and treated as one unit. The antenna factors from each sub-arrays are then added to form an antenna factor for the entire heater. Each of the sub-arrays can also be focused by adding a correction to the phase term so that the complex exponential in the numerator of (6.3) equals 1:

$$A_t = \sum_{n=1}^{N} \left[ \frac{\exp(-jk(r_n - r_{0n}))}{r_n} \right] A_n \qquad (6.4)$$

where    $A_t$ = array and space loss factor for entire heater

   $r_{0n}$ = distance from center of sub-array to point of focus.

   $r_n$ = distance from center of sub-array to point of measurement.

   $A_n$ = array and space loss factor for nth sub-array.

The routine lets the user input the size of the sub-arrays, the number of sub-arrays, and their placement in the aperture.

### 6.1.3 Ambient Atmospheric and Ionospheric Model

The accuracy of the ambient values for electron density and neutral density are important to the accuracy of the model. The atmospheric data in the simulation are taken from the U.S. Standard Atmosphere [COESA, 1976], and ambient electron density data are typical of midlatitude daytime conditions. A cubic spline is fit through the data, enabling the extraction of values at any altitude.

### 6.1.4 Ionization Frequency and Collision Frequency Formulas

The foundations of the FAIM code are the formulas it uses for net ionization frequency and collision frequency for momentum transfer. Two versions are included in the code, "empirical" formulas based on chamber experiments, and analytic approximations based on test particle analysis. Either version is selectable as an option, and both are described below.

The set of parametric formulas is empirically based on experimental data compiled by Ali [Ali, 1988]. These formulas are based on a scaling of $E/P$ ($E$ = electric field, $P$ = atmospheric pressure). The formula for net ionization frequency, $v_{net}$, uses empirical formulas for the Townsend ionization coefficient, $\alpha$, and the electron drift velocity, $V_d$, and combines them to form a formula for $v_{net}$:

$$\frac{v_{net}}{P} = \frac{\alpha}{P} V_d \qquad (6.5)$$

The formulas for $V_d$ and $\alpha$ are based on DC field data. As described in section 2, these data may be used for microwave air breakdown if $E$ is replace by $E_e$, an effective electric field, within the limits of the effective field approximation.

$$E_e = E \frac{v_m^2}{v_m^2 + \omega^2} \qquad (6.6)$$

where     $v_m$ = collision frequency for momentum transfer.
$\omega$ = angular heater frequency.

The collision frequency is required for determining the effective electric field and also for determining the complex dielectric constant of the medium, which in turn fixes the amount

of attenuation or self-absorption of the microwave pulse (see Figure 6.1). $V_m$ is expressed as a function of $E/P$ by using its relationship with the drift velocity $V_d$:

$$V_m = \frac{e}{m} \cdot \frac{E_e}{V_d} \tag{6.7}$$

The reader will note that $E_e$ is dependent on $V_m$. The code creates a recursive loop that computes each value alternately until they converge.

The analytic approximation was developed in section 3. Computational constraints prohibit performing kinetic calculations at a number of different altitude grids simultaneously. Moreover, such a simulation would be very inefficient in the sense that the calculations are extremely repetitive. Therefore, expressions have been developed for ionization frequency and collision frequency that are based on a test particle approach, and agree well with results from the zero-dimensional kinetic simulation. The formulas are repeated here for completeness. We begin with the quiver energy of an electron:

$$\tilde{\varepsilon} = \frac{1}{2} m \frac{e^2 E_0^2}{m \, \omega^2} \cong 1.68 \times 10^{-4} \frac{S}{f^2} \left( \frac{W/m^2}{100 \, MHz} \right) \tag{6.8}$$

This is the fundamental quantity in the ionization frequency formula. The reader will note it is proportional to $1/f^2$, as is $E_e$ in the formulas above.

$$V_m = 1.3 \times 10^{-7} N \tag{6.9}$$

$$V_{net} = 9 \times 10^{-9} N \left( \frac{\tilde{\varepsilon}}{1 + \frac{V_{max}^2}{\omega^2}} \right) \exp \left[ - \sqrt{\frac{2}{\tilde{\varepsilon}/\left(1 + \frac{V_{max}^2}{\omega^2}\right)}} \right] (1 - G(\tilde{\varepsilon})) \tag{6.10}$$

where    $N$ = neutral density

   $G(\tilde{\varepsilon}) = 3.7 \times 10^{-4} \exp\left[.6\sqrt{20/\tilde{\varepsilon}}\right]$ = reattachment term

   $V_{max}$ = maximum collision frequency = $3 \times 10^{-7} N$

The final term has minimal effect on the overall formula. It represents the effects of reattachment, which are minor in virtually all cases where substantial electron production

127

occurs. It serves primarily to extend the range of validity of the equation downward toward low power levels.

All results of the plasma formation code presented in section 4 were computed using the analytic approximation. A comparison of the ionization frequencies and the resulting plasma frequency profiles for Ali's empirical formulas and the analytic approximation is presented in Figures 6.2 and 6.3.
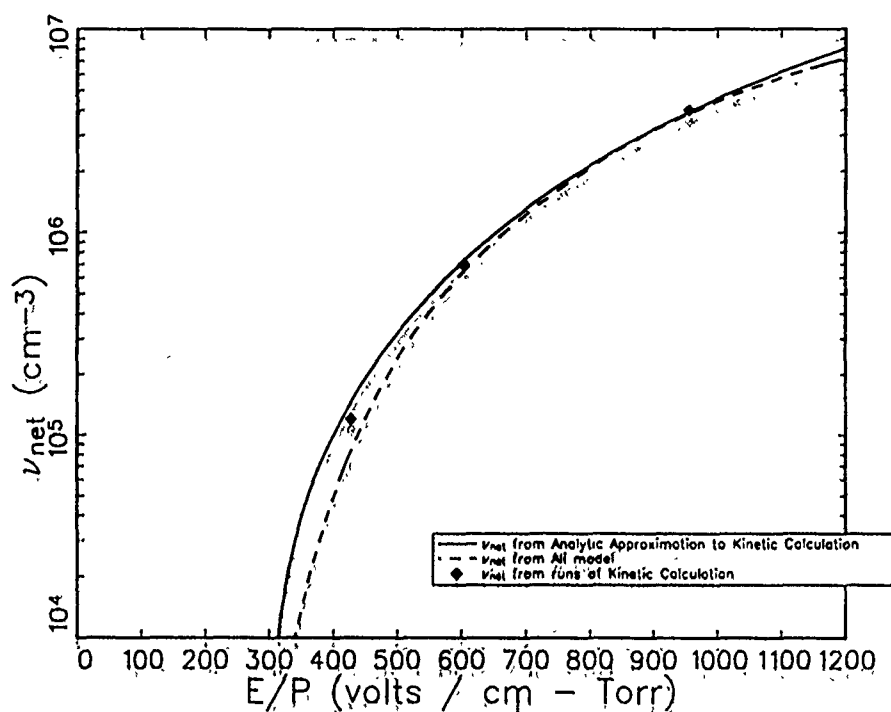


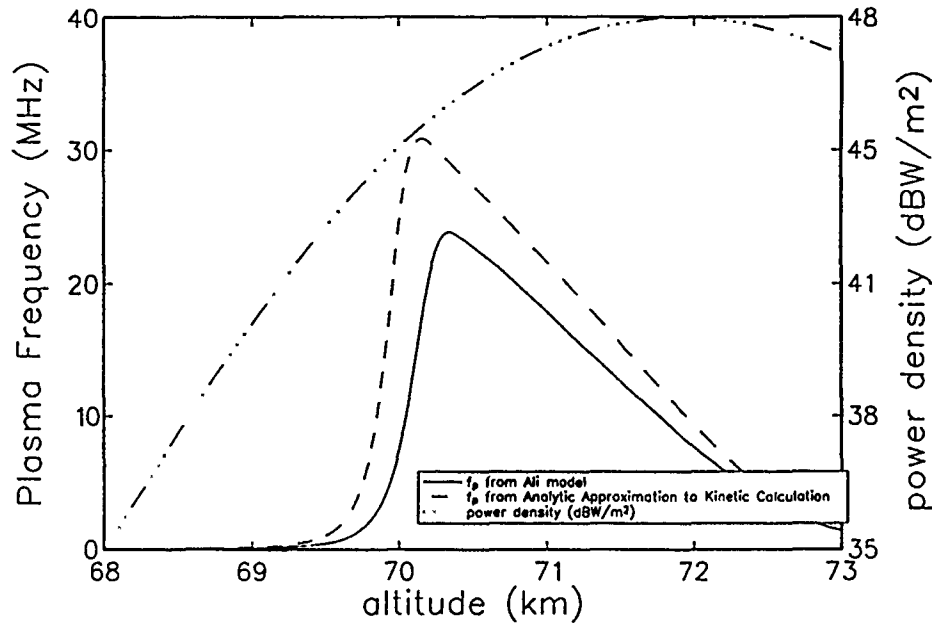Figure 6.2 Ionization Frequencies for $f = 300$ MHz, $h = 70$ km

Figure 6.3. Plasma Frequency Profiles for $f = 300$ MHz, $h = 70$ km

## 6.2 Propagation Simulation

The propagation simulation is based on the ray tracing approach described in section 5.3.1.1. The simulation uses the complex refractive index $\tilde{n}$ to calculate the ray path and absorption for a signal propagating through the patch created in the heater simulation above.

$$\tilde{n} = \sqrt{1 - \left(\frac{\omega_p^2}{\omega^2 + v_m^2}\right)\left(1 + j\frac{v_m}{\omega}\right)} \qquad (6.11)$$

The simulation performs integration with respect to time of one scalar and two vector differential equations simultaneously:

$$\frac{d\mathbf{n}}{dt} = \frac{c}{n}\frac{\partial n}{\partial \mathbf{r}} \tag{6.12}$$

$$\frac{d\mathbf{r}}{dt} = \frac{c\mathbf{n}}{n^2} \tag{6.13}$$

$$\frac{d}{dt}(\ln E) = -\omega \frac{\text{Im}(\tilde{n})}{\text{Re}(\tilde{n})} \tag{6.14}$$

where

> $\mathbf{n}$ = the refractive index vector, whose magnitude is equal to the real part
> of the complex refractive index $\tilde{n}$,
>
> $\mathbf{r}$ = the location of the tip of the ray, and
>
> $E$ = electric field intensity.

The one-dimensional plasma density profiles generated by the plasma formation simulation are used to synthesize a two-dimensional plasma profile representing a uniform patch at an angle of 45°. Equations (6.12-14) are then integrated over the transit time of the ray through the patch to determine the ratio of initial to final electric field intensities, and therefore the power loss. The electron neutral collision frequency $v_m$ is assumed to have cooled to its ambient value. Reheating of the plasma by the incident wave is not currently taken into account in the absorption calculation, but is accounted for by separate calculations which produce an additional loss factor. (A more complete discussion of absorption and reheating effects is given in section 5.4.2 above.)

In addition to direct calculation of absorption, additional information on the effects of the reflection process on the signal may also be developed from the electron density profile produced by the plasma formation simulation. By calculating the refractive index separately for the ordinary and extraordinary rays, the effects of Faraday rotation may be included; in addition, the simulation is capable of directly accepting input from a two-dimensional patch simulation to calculate the effects of irregularities.

The integrated nature of the simulation allows examination of the effect of heater design changes on the losses experienced by the signal. For example, Figure 6.4 below shows the effect of changes in the heater antenna size (assuming a randomly thinned square array) on the single-pass absorption of the reflected signal. Here the heater power is held constant

while the aperture is increased, resulting in a sharper focus of the heater E-field. This, in turn, generates a steeper plasma density gradient, which absorbs less of the signal power.
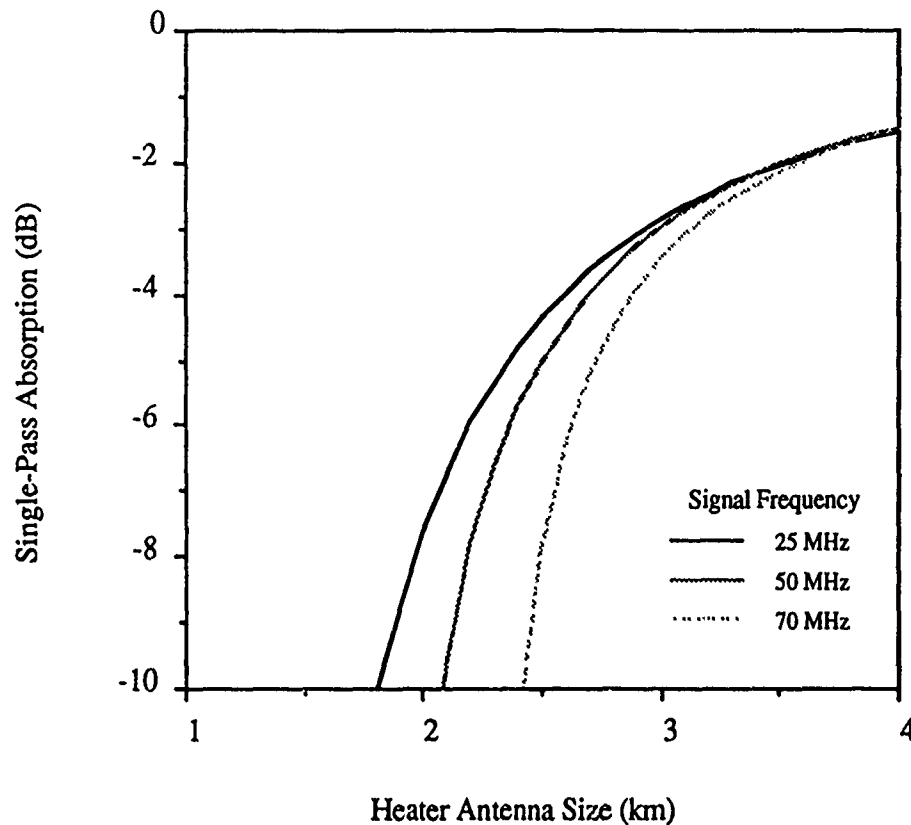


Figure 6.4. Change in Absorption with Heater Antenna Size

This figure shows that, for this example, increasing the size of the heater antenna brings diminishing returns when the size exceeds 2.5-3 km, and illustrates the use of the integrated simulation in to develop a consistent, cost-effective design by considering the interaction between all elements of the AIM system.

## 6.3   Conclusion

An integrated plasma formation and electromagnetic signal reflection has been developed. The simulation has been based on detailed analysis of the plasma formation and signal reflection process, as described in sections 3, 4, and 5 above, and has been used to determine the interactions between the major components of the AIM system.

# 7.0 RECOMMENDATIONS FOR THE NEXT PHASE

## 7.1 Near-Term Atmospheric Experiment

The most critical next step in the development of the AIM system is the performance of an atmospheric Proof of Principle experiment. Several candidate experiments that vary widely in cost and in utility could be performed:

- A rocket-borne electron beam experiment.
- A chemical (eg barium) release experiment in conjunction with an existing high ERP facility.
- A modification of some existing facility (likely Arecibo) to increase the ERP sufficiently to produce breakdown (existing high ERP facilities are surveyed in Figure 7.1).
- The development of a dedicated facility (perhaps in Alaska) that could be used freely for ionospheric experiments.
- Proceeding directly to the FSED AIM heater concept for experimentation.

Table 7.1 presents the preliminary tradeoffs among the various candidates.

A particularly appealing candidate for a near term atmospheric test is the Alaskan dedicated facility. Such a facility has several distinctive advantages:

- It could be developed sequentially with some experiments at each stage.
- The Proof of Principle system could be integrated from non-developmental components.
- The system would be available for experimentation as required (ie not subject to NSF or other approval).
- Since the system would have residual military/commercial value for communications, its development could conceivably be cost-shared.

Such a system could be installed in about a three-year time frame in a selected site in Alaska. The Fairbanks area is probably optimum in that a military/NASA infrastructure is in place in the area, and it enjoys a central location in the state. The latter is a factor in the residual value of the AIM Proof of Principle facility, ie as a commercial/military communications relay system. Figure 7.2 illustrates the concept.
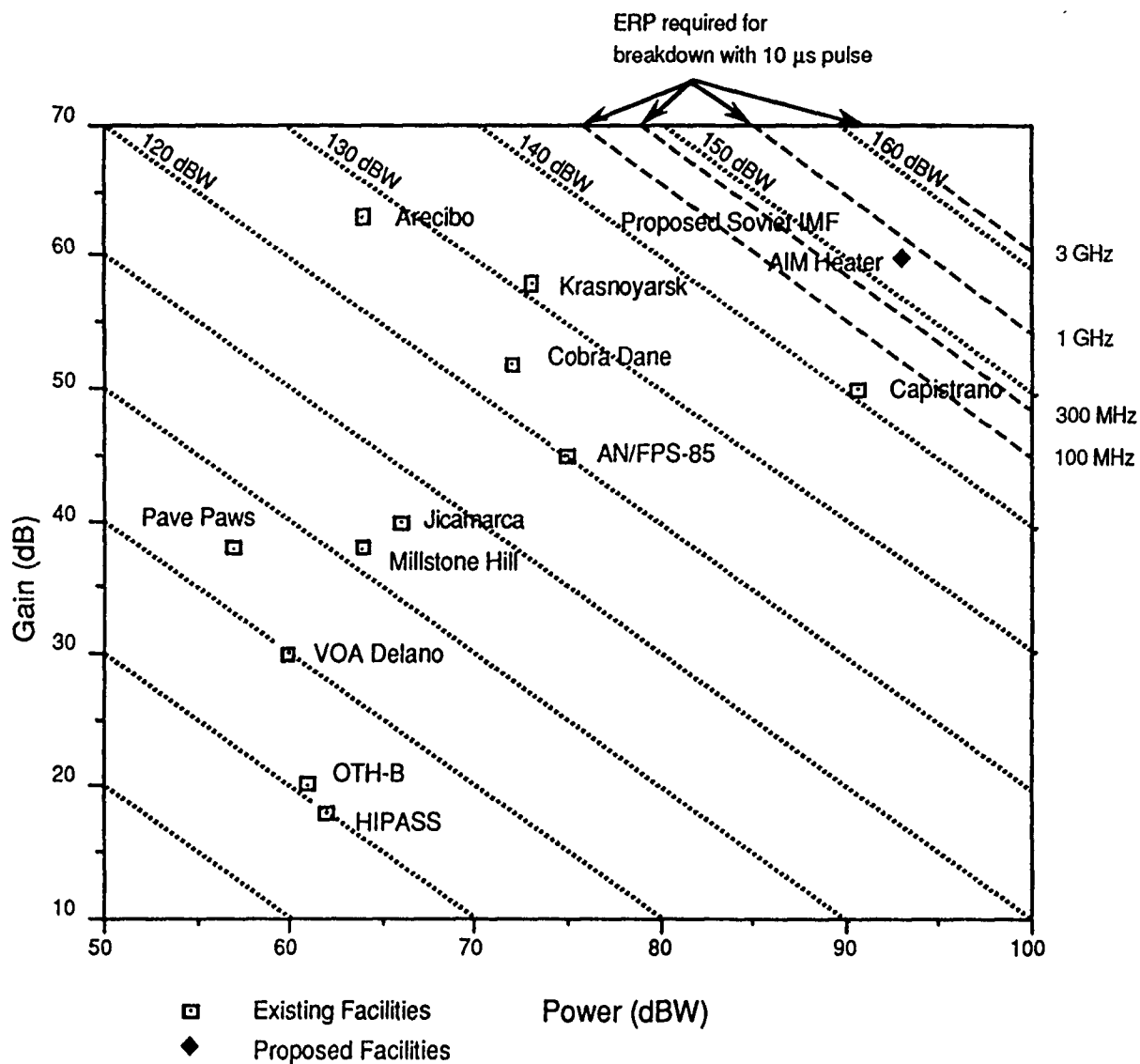
ERP required for breakdown with 10 µs pulse

Figure 7.1. No Existing High Power Facility Is Suitable for an AIM Atmospheric Breakdown Experiment without Modification

133

Table 7.1.  Comparison of Alternative Atmospheric Demonstration Experiments

| Evidence of AIM Feasibility | | E-Beam | Arecibo | W/Release | Alaska | W/Release | AIM Heater |
|---|---|---|---|---|---|---|---|
| Mirror Creation | Controlled Breakdown from Ground | - | ✓- | ✓- | ✓+ | ✓- | ✓+ |
| | Peak Density | - | ✓- | - | ✓ | - | ✓+ |
| | Density Profile Control | - | - | - | ✓- | - | ✓+ |
| | Mirror Painting | - | - | - | ✓- | - | ✓+ |
| Mirror Evolution | Lifetime | ✓- | ✓ | ✓- | ✓ | ✓- | ✓+ |
| | Ambient Winds | ✓- | ✓ | ✓ | ✓ | ✓ | ✓+ |
| Mirror Utility | Communications Demonstration | - | - | ✓- | ✓ | ✓- | ✓+ |
| | Radar Demonstration | - | - | - | ✓- | ✓- | ✓+ |
| Advantages/Disadvantages | | E-Beam | Arecibo | W/Release | Alaska | W/Release | AIM Heater |
| Cost | | | Moderate | Low | Moderate | Low | High |
| Risk | | High | Moderate | Low | Low-Mod | Low | Low-Mod. |
| Availability | | One-time | Limited | Limited-Shots | Unlimited | N-Shots | Unlimited |
| Location | | | Arecibo | | Fairbanks/Poker Flats | | Open |
| Residual Value | | None | Low | None | High | Low | High |
| Physical Correspondence to End System | | - | ✓- | ✓- | ✓ | ✓- | ✓+ |

Code:
-    Not Available
✓-   Marginal
✓    Good
✓+   Excellent

134

Such a heater system could be built from existing components. The two major types of hardware required are the antennas and the RF sources. Based upon our preliminary survey, 20 meter satellite dishes appear to be the most cost-effective antennas. These could be fed with Stanford Linear Accelerator klystrons that are currently producing around 100 MW at S band.
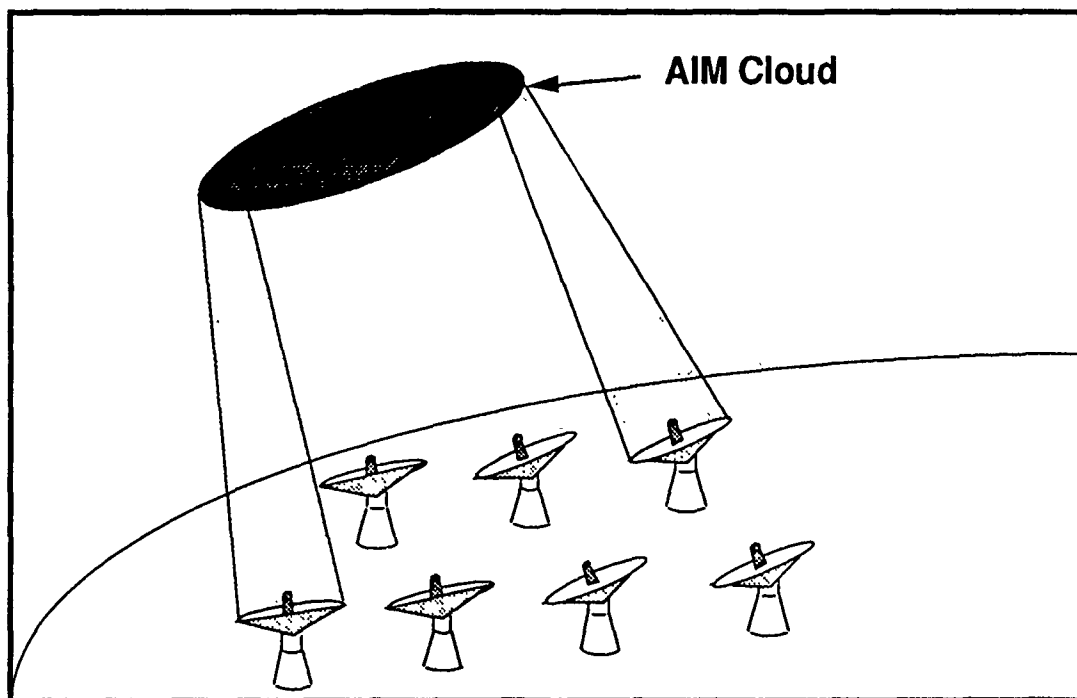


Figure 7.2. The Alaskan AIM Proof of Principle Facility

## 7.2 Chamber Experiment Design

Another important recommendation is a series of chamber experiments that will represent as closely as possible the physics parameters associated with a full-scale AIM system. Previous experiments in air breakdown physics have utilized relatively high heater RFs at atmospheric pressures significantly greater than 60 Km atmosphere. As a result, the plasma decay time and recombination characteristics are far from the region of interest for AIM. Also, these experiments have not addressed the more intricate issues of density

135

control, through antenna focussing and frequency agility. Careful diagnosis of the patch creation and decay could be performed to assess the lifetime and distribution of the electron density. Knowing these characteristics of the electron density profiles would allow the physics models to accurately predict propagation characteristics. Figure 7.3 illustrates the likely configuration for an AIM chamber experiment that will be scientifically meaningful.
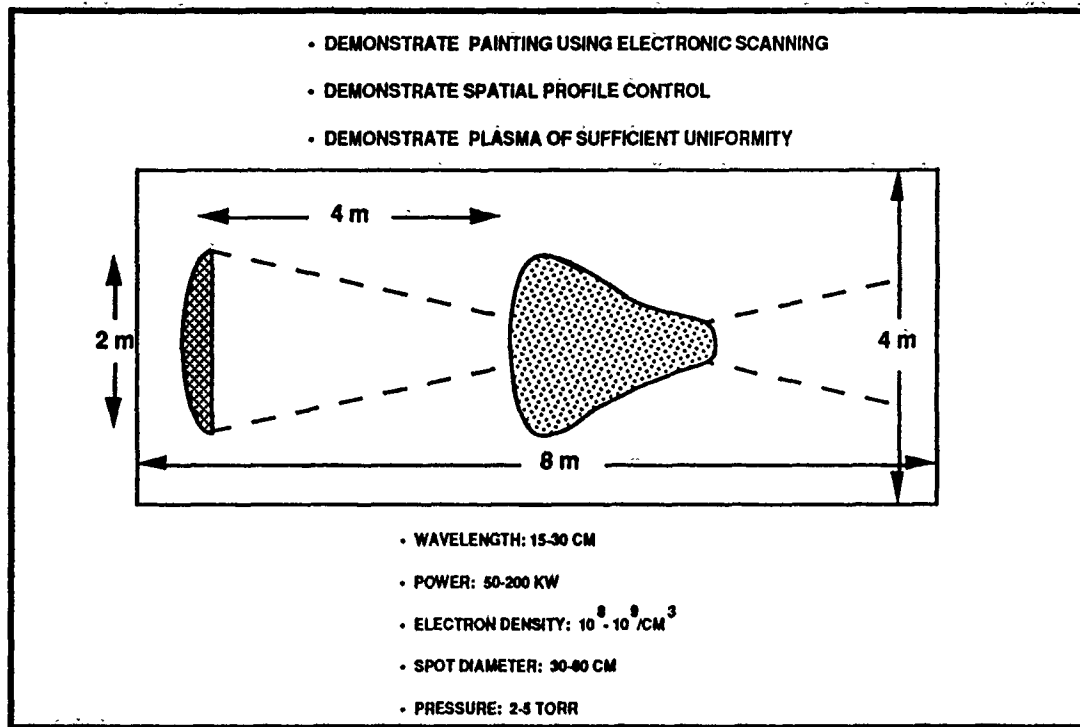


Figure 7.3. A Meaningful AIM Experiment Can Be Performed in a Small Chamber

## 7.3 Heater Design

The following key issues associated with fabricating a large aperture RF heater using tubes or solid-state should be addressed:

- Determining the number and placement of dishes/subarrays to form a coherent beam at the proper altitude for AIM formation,
- Verifying the accuracy and uncertainty with which signal parameters from each dish/subarray can be measured by a reference scheme,
- Verifying that the unit-by-unit calibration scheme can cause each dish/subarray to produce a desired transmitted waveform,

136

- Validating that an arbitrary waveform for transmission can be achieved by GaAs digital IC technology at the 1 GHz clock rates and that klystrons can be synchronized with sufficient precision.

Analytical modelling and numerical simulation could be performed to determine the trade-offs involved in selecting placement and number of heater array panels for a range of power density and frequency space-time profiles. Breadboard experiments could be designed to determine the capabilities of silicon digital circuit and power amplifier technology to produce arbitrary waveform transmissions and the output transmit level. In addition, the limits of accuracy and stability to measure signal parameters using state-of-the-art equipment could be experimentally determined.

## 7.4 Preliminary Environmental Assessment

A preliminary environmental assessment of the AIM concept should be performed in order to determine if there are any effects that could be of any significance. Effects to be considered are hazards to living tissues, electromagnetic interference, and ionospheric effects.

# BIBLIOGRAPHY

Ali, A. W. *Laser and Particle Beams* 6, 105 (1988) and Naval Research Laboratory
Memorandum Report, 5815, August (1986).

Ali, A. W., "Excitation and Ionization Cross Sections for Electron Beam and
Microwave   Energy Deposition in Air," Naval Research Laboratory Memo
Report 4598 (1981); (revised version in press).

Allis, W. P., "Motions of Ions and Electrons," in *Encyclopedia of Physics*, ed. S.
Flugge, v. 11, Berlin: Springer-Verlag (1956).

August, G. *"Advanced Microwave Effects"* Vol. 1, *"Experiments on Air Breakdown
Using Short, Intensive Microwave Pulses"* DNA-TR-88-80-V1 (1988).

Babal'yants, V.F., Vurzel', F.B. and Polak, L.S. Zh. Tekh. Fiz. 43, 1895 (1973) (Sov.
Phys. Tech. Phys. 18, 1197 (1976).

Bailey, V. A., "Generation of Auroras by Means of Radio Waves," Nature, v. 142
(1938), p. 613.

Bailey, V. A., "On Some Effects Caused in the Ionosphere by Electric Waves," Phil.
Mag., v. 23 (1937), p. 929.

Bandel, H. W. and MacDonald, A. D. *J. Appl. Phys,* 41, 2903 (1970).

Bisbing, P. E., McMenamin,  D. L., Jordan,  A. K. and Schere, P. M. *"Study to Obtain
Design Data for Reentry ECM Antenna Systems"* AFCRL-68-0226, GE Report
68SD591, General Electric, Philadelphia, PA (1968), AD835245

Bollen, W. M., Yee, C. L., Ali, A. W., Nagurney, M. J. and Read, M. E. *J. Appl. Phys.*
54, 101 (1983).

Brassem, P. and Maeseu, F.J. *Spectochim ACTA* 29, B, 203 (1974).

Budden, K. G., The Propagation of Radio Waves. Cambridge: Cambridge University
Press (1985).

Byrne, D. P., Alvarez, R. A. and Johnson, R. M. *"Air Breakdown Limits for Microwave Pulse Propagation. Part I Experiments"* Lawrence Livermore National Laboratory Report UCID - 19877 Pt. 1 (1983).

Case, W., and Sprangle, P., "Reflection of Microwave Signals off a Plasma Layer with Density Fluctuations and Collisional Effects," APTI Technical Report 1002 (1988).

Clavier, P. A., "Man-Made Heating and Ionization of the Upper Atmosphere," *J. Appl. Phys.*, v. 32, n. 4 (1961), p. 510.

COESA, *U.S. Standard Atmosphere*, 1976, U.S. Government Printing Office, Washington, D.C. 1976

Didenko, A. N., Novikov, S. A., Razin, S. V., Chumerin, P. Y. and Yushkov, Y. G. *Sov J. Communication Tech. and Electronics*, No. 4 731, (1985).

Felsenthal, P. and Proud, J. M. *Phys. Rev.* 139, A 1796 (1965).

Felsenthal, P. *J. Appl. Phys.* 37, 4557 (1966).

Franklin, J.L., Studnairs, S.A. and Ghosh, P.K. *J. Appl. Phys.* 39, 2052 (1968).

Geballe, R. and Harrison, M. A. *Phys. Rev.* 91, 1 (1953).

Gould, L., and Roberts, L. W. *J. Appl. Phys.* 27, 1162 (1956).

Gurevich, A. B., Karfidov, D. M., Lukina, N. A. and Sergeychev, K. F. *Soviet Geomagnetism and Aeronomy* 20, 668 (1980).

Gurevich, A. V., "Contribution to the Theory of Nonlinear Effects during Radio Wave Propagation in the Ionosphere," Geomagn. Aeron., v. 5 (1965), p. 49.

Gurevich, A. V., *Nonlinear Phenomena in the Ionosphere*, New York: Springer-Verlag (1978).

Hays, G. N, Pitchford, L. C., Gerardo, J. B., Verdeyen , J. T. and Li, Y. M. *Phys. Rev. A* 36, 2031 (1987).

Hays, G. N. Sandia Laboratories *"Private Communication"* (1989).

139

Hays, G. N., L. C. Pitchford, J. B. Gerardo, J. T. Verdeyen and Y. M. Li, "Ionization Rate Coefficients and Induction Times in Nitrogen at High Values of E/N," *Phys. Rev.* A, v. 36, n. 5 (1987), p. 2031.

Herlin, M. A., and Brown, S. C. *Phys. Rev.* 74, 291 (1948), 74, 1650 (1948). *J. Appl. Phys.* 42, 5871 (1971).

Jursa, A. S., ed., *Handbook of Geophysics and the Space Environment.* Hanscom AFB, Massachusetts: Air Force Geophysics Laboratory, 1985, AFGL-TR-85-0315, ADA167000.

Kal'vina, I.N., Leot'eva, S.M., and Shuvalova, L.G. *Opt. Spektrosk.* 2, 173 (1968).

Karfidov, D. M., Lukina, N. A. and Sergeychev, K. F. *Sov. Plasma Phys.* 2, 605 (1983).

Karfidov, D. M., Lykima, N.A., and Sergeychev, K.F. *Soviet Plasma Physics.* 7., 312 (1981).

Lombardini, P. P., "Alteration of the Electron Density of the Lower Ionosphere with Ground-Based Transmitters," *Radio Science*, v. 1 (1965), p. 83.

Lupan, Y. A. *Sov. Phys. Tech. Phys.* 21, 1367 (1976).

MacDonald, A. D. "*Microwave Breakdown in Gases*", Wiley, New York (1966).

MacDonald, A. D., Gaskell, D. V., and Giterman, H. N. *Phys. Rev.* 130, 1841 (1963).

Maksimov, A.I. *Soviet Phys. Tech. Phys.* 11, 1316 (1967).

Mayan, J. T. and Fante, R. L. *J. Appl. Phys.* 40, 5207 (1969).

Mosher, D., "Monthly Technical Report," ARCO Power Technologies Inc., November 1988.

Rose, D. J. and Brown, S. C. *J. Appl. Phys.* 28, 561 (1957).

Scharfman, W. and Morita, T. *J. Appl. Phys.* 35, 2016, (1964).

Scharfman, W. E., Taylor, W. C. and Morita, T. *IEEE*, AP-12, 709 (1964).

Schlumbohm, H. Z. *Z. Physik* 182, 317 (1965).

Sullivan, C. A., Destler, W. W., Rodgers, J. and Segalov, Z. *J. Appl. Phys.* 63, 5228 (1988).

Taylor, W. C., Chown, J. B. and Morita, T. *J. Appl. Phys.* 39, 191 (1968).

Tetenbaum, S. J., MacDonald, A. D., and Bandel, H. W. *J. Appl. Phys.* 42, 5871 (1971).

Woo, W and DeGroot, J. S. *Phys. Fluids* 27, 475 (1984).

Yee, C. L., Ali, A. W., and Bollen, W. M. *J. Appl. Phys.* 54, 1278 (1983).

Yee, J. H., Alvarez, R. A., Mayhall, D. J., Byrne, D. P. and DeGroot, *J. Phys. Fluids* 29 1238 (1986).